Response of the wind-turbine wake to a turbulent atmospheric boundary-layer flow

Antonia Englberger

München 2017

Response of the wind-turbine wake to a turbulent atmospheric boundary-layer flow

Antonia Englberger

Dissertation
an der Fakultät für Physik
der Ludwig–Maximilians–Universität
München

vorgelegt von
Antonia Englberger
geb. Kempf

München, den 14. 07. 2017

Erstgutachter: Prof. Dr. George Craig
Zweitgutachter: Prof. Dr. Markus Rapp
Tag der mündlichen Prüfung: 20. 10. 2017

Für meine Familie.

Zusammenfassung

Die Eigenschaften des Nachlaufs einer Windturbine werden für verschiedene im Laufe eines Tages in einer turbulenten Grenzschicht auftretende atmosphärische Schichtungen mit Grobstruktursimulationen mit dem Strömungslöser EULAG untersucht. Dafür wurde eine Methode zur Erhaltung der Hintergrundturbulenz für Windturbinensimulationen mit offenen Randbedingungen in Strömungsrichtung entwickelt. Dies wird durch das Aufprägen der turbulenten Fluktuationen in der spektralen Energieverteilung einer neutralen Grenzschicht ermöglicht. Weiter lässt sich damit das permanente Einlesen von turbulenten Einströmprofilen in die Windturbinensimulationen vermeiden. Zusätzlich wurden idealisierte Tagesgangsimulationen über homogenen und heterogenen Oberflächen durchgeführt. Der Tagesgang zeigt einen signifikanten Einfluss auf den Wind und die Turbulenz in der atmosphärischen Grenzschicht. Unter homogenen Bedingungen treten in der stabilen und der morgendlichen Grenzschicht eine starke vertikale Windscherung und eine Änderung der Windrichtung mit der Höhe auf, wohingegen in der konvektiven und der abendlichen Grenzschicht die Turbulenz in der Atmosphäre stark ausgeprägt ist. Unter heterogenen Bedingungen hat die nächtliche Zunahme der Scherung einen großen Einfluss auf Wind und Turbulenz, und führt zu einer Kompensation der Ekmanspirale. Windturbinensimulationen werden mit synchronisierten Daten aus den Tagesgangsimulationen betrieben. Die sich ergebenden Nachläufe sind von der Stabilität der Atmosphäre beeinflusst und haben ihrerseits einen Einfluss auf die Energieeffizienz der Windturbine. Das Strömungsfeld wird durch eine schnellere Einmischung unter konvektiven Bedingungen am Tag, im Gegensatz zur Nacht, geprägt. Die Nachläufe, die sich in der abendlichen und morgendlichen Grenzschicht entwickeln, sind entscheidend von der vorhergehenden atmosphärischen Situation beeinflusst. Um diese äußerst rechenintensiven Tagesgangsimulationen zu vermeiden, wurde die Methode zur Aufrechterhaltung der Hintergrundturbulenz zu einer Parametrisierung ausgeweitet. Diese beinhaltet eine schichtungsspezifische Gewichtung sowie entsprechende Hintergrundwindprofile, beides aus der idealisierten Tagesgangsimulation über homogener Oberfläche abgeleitet. Die Windturbinensimulationen mit Parametrisierung zeigen eine gute Übereinstimmung mit den synchronisierten Windturbinensimulationen aus der Tagesgangsimulation über homogener Oberfläche und reduzieren die erforderliche Rechenzeit um den Faktor $\mathcal{O}(10^2)$. Dies spricht für eine einfache und äußerst effiziente Parametrisierung des turbulenten einströmenden Windfeldes für Grobstruktursimulationen unterschiedlicher thermischer Schichtungen.

Abstract

The wake characteristics of a wind turbine for different regimes occurring throughout the diurnal cycle are investigated systematically by means of large-eddy simulation with the geophysical flow solver EULAG. A methodology to maintain the turbulence of the background flow in wind-turbine simulations with open streamwise boundaries, without the necessity of the permanent import of turbulence data, was developed. These requirements are fulfilled by applying the turbulent fluctuations of the spectral energy distribution of a neutral boundary layer in the wind-turbine simulations. Further, idealized diurnal cycle simulations over homogeneous and heterogeneous surface were performed. Under homogeneous conditions, the diurnal cycle significantly impacts the low-level wind shear and the atmospheric turbulence. A strong vertical wind shear and veering with height occur in the nocturnal stable boundary layer and in the morning boundary layer, whereas the atmospheric turbulence is much larger in the convective boundary layer and in the evening boundary layer. The increased shear under heterogeneous conditions change these characteristics, counteracting the formation of the night-time Ekman spiral. Synchronized turbulent inflow data from the diurnal cycle simulations drive the wind-turbine simulations. The resulting wake is strongly influenced by the stability of the atmosphere and has an impact on the efficiency of the wind turbine. The flow in the wake recovers more rapidly under convective conditions during the day, than under stable conditions at night. The wake characteristics of the transitional periods are influenced by the flow regime prior to the transition. To alleviate the computational extremely expensive diurnal cycle simulations, the turbulence preserving method was extended to a parameterization, which includes a stratification related weighting and suitable background wind profiles, both resulting from the idealized diurnal cycle precursor simulation over homogeneous surface. The following parameterization wind-turbine simulations are in good agreement with the synchronized diurnal cycle wind-turbine simulations over homogeneous surface and reduce the computational costs by a factor of $\mathcal{O}(10^2)$. Therefore, they result in a simple, numerically efficient, and computationally fast parameterization of turbulent wind-turbine flows for large-eddy simulations of different thermal stratifications.

Contents

1 Introduction

Energy supply and demand - current status and future challenges

The importance of renewable energies is increasing worldwide because accessible non-renewable resources become depleted and because of the climate change. Both make the optimal use of the renewable energy resources a crucial problem.

World population has reached 7.3 billion in 2015 with a primary energy demand amounted to 1.3×10^{14} kWh a^{-1}. This was covered to 32.9 % by oil, to 29.2 % by coal, to 23.8 % by gas, to 4.4 % by nuclear, to 6.8 % by hydro, and to 2.8 % by other renewables (wind, solar, geothermal, biomass and waste) (BP, 2016).

Germany demanded 2.4 % of the total primary energy in 2015. It was covered to 34.4 % by oil, to 21.0 % by coal, to 24.4 % by gas, to 6.5 % by nuclear, to 1.4 % by hydro, and to 12.5 % by other renewables. Compared to the total world statistic, the contribution of other renewables is almost three times larger in Germany, with wind representing a main supplier. The installed wind capacity in Germany represents 10.9 % of the total installed capacity worldwide (BP, 2016).

In 2050 the world population is expected to reach its maximum of 10 billion with a primary energy demand of 2.0×10^{14} kWh a^{-1}. The non-renewables oil, coal, gas, and nuclear, however, can only produce 40% of this demand, because accessible reserves become depleted. 60% has to be produced by renewable energies. Considering the climate change, an environmentally sensitive energy supply without coal and nuclear even requires a contribution of 93% of the renewable energies to the primary energy supply in 2050. Either way, the renewable energy contribution has to increase from 9.6 % in 2015 to at least 60 % in 2050 (Pelte, 2014).

The two main renewables, besides the geographically limited hydro (see Germany), are wind and solar. In 2015, wind contributes globally with 1,4 % and solar with 0.5 % to the primary energy (BP, 2016).
The contribution of solar is smaller because it is limited to the day with a decrease of efficiency towards higher latitudes. (The rate of utilization in Germany is only 7 % of the power efficiency factor of a photovoltaic panel (Pelte, 2014).) Further, it requires a large amount of space. (If every roof in Germany will be covered with photovoltaic panels, only 2 % of Germany's primary energy demand will be covered (Pelte, 2014).)
Wind, on the contrary, is available almost everywhere and at every time in the midlatitudes. The rate of utilization does not depend on the geographical latitude. (For Germany, this results in a rate of utilization of 22 % of the power efficiency factor (Pelte, 2014).) Further, the required space is much less and over land it can still be used by agriculture, while it is available offshore anyway. Therefore, wind has a high potential to provide the major contribution of the primary energy demand in the world in 2050.

Wind energy

A wind turbine transforms the kinetic energy in the wind $^1/_2 mv^2$ into mechanical energy and finally into electrical energy. The maximum available power is $^1/_2 \rho A v^3$, where ρ is the density of the air, A the area of the rotor, and v the wind speed. As the rotor cannot decelerate the wind speed to zero, the maximum available power in the wind is reduced to the actual power $^1/_2 \rho A v^3 c_p$, where $c_p = {}^{16}/_{27}$ is a constant, denoted as the Betz limit. Modern wind turbines operate close to this limit with $c_p = 0.5$. The actual power is further reduced by the mechanical power efficiency factor $\eta_{mech} = 0.64$, resulting in the useful power $^1/_2 \rho A v^3 c_p \eta_{mech}$ (Manwell et al., 2002; Emeis, 2013, 2014; Pelte, 2014).

According to this equation, there are three ways to optimize the useful power of a wind turbine: An increase of η_{mech}, A or v. This results in a strict limitation of what can actually be done to make wind energy more efficient, as an increase of η_{mech} is an engineering issue and an increase of A is restricted. The largest onshore wind turbine (Enercon E-126) already has a rotor diameter of 127 m and the largest offshore wind turbine (Vestas V164-8.0) reaches even 171.2 m (wind-turbine models, 2016). The wind has the largest impact on the useful power, due to the third power of v. The wind, however, depends on many factors, like the wind-turbine site, the surface condition, and the prevailing atmospheric situation. Therefore, considering the diurnal variation of the near surface wind instead of an average climatology of the wind is fundamental to get the actual wind condition. The near surface wind, however, is influenced by different turbulence structures of the atmospheric boundary layer (ABL), which vary during the diurnal cycle. Therefore, the basic scientific knowledge of how a wind turbine reacts under different atmospheric conditions constitutes the main challenge to optimize the useful power of a wind turbine, leading to a better utilization of wind energy. Finally, this knowledge should also lead to better wind-farm optimization techniques.

Atmospheric boundary layer

The ABL in Fig. 1.1 reaches from the surface up to a height of 100 m to 3000 m. Based on thermal stratification, it can be classified as convective, stable, or neutral (Stull, 1988): Convective atmospheric stratification is caused by a warmer surface than the atmosphere due to solar irradiation during the day. The corresponding potential temperature decreases with height in the surface layer (bottom 10 % of ABL) and is constant above. Stable atmospheric stratification results from a surface colder than the atmosphere due to outgoing infrared radiation at night. The corresponding potential temperature increases with height in the surface layer and is also constant above. Neutral atmospheric stratification occurs under very high wind speeds or during the transition between the stable boundary layer (SBL) at night and the convective boundary layer (CBL) at day with only little cooling or heating at the surface and an adiabatic potential temperature profile. The transition periods of the morning and the evening are defined following Grimsdell and Angevine (2002) as the time period in which the sensible heat flux at the surface changes sign (Fig. 1.1). The morning boundary layer (MBL) and the evening boundary layer (EBL) include the atmospheric situation before and after the corresponding transition.

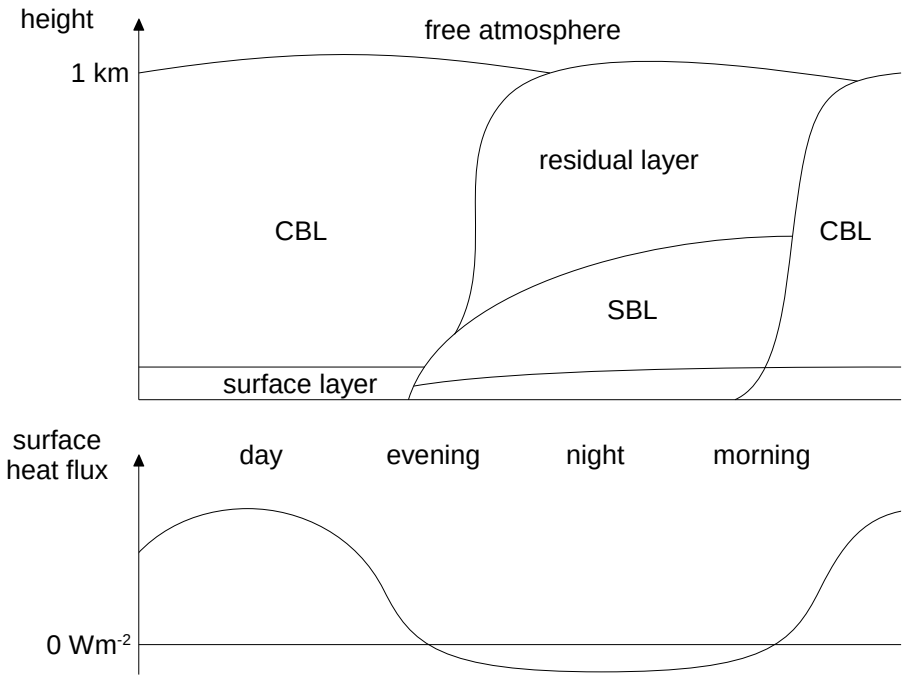

Figure 1.1: The diurnal evolution of the vertical boundary-layer structure, consisting of three major parts: a very turbulent and well-mixed convective boundary layer during the day, a less-turbulent residual layer and a nocturnal stable boundary layer with a small amount of turbulence at night. The transitional phases correspond to the evening and the morning boundary layers. The surface heat flux evolution during the diurnal cycle is shown below.

This diurnal cycle of the ABL has been studied since the 1970s. There are many observational and numerical studies regarding the SBL (Nieuwstadt, 1984; Carlson and Stull, 1986; Mahrt, 1998) or especially the residual layer (Balsley et al., 2008; Wehner et al., 2010). The CBL has also been investigated intensively with different focuses, e.g. on coherent structures (Schmidt and Schumann, 1989), on entrainment (Sorbjan, 1996; Sullivan et al., 1998; Conzemius and Fedorovich, 2007), and on shear (Moeng and Sullivan, 1994; Fedorovich et al., 2001; Pino et al., 2003). The first LES of a transition process in the ABL was performed by Deardorff (1974a,b). Since then, many simulations considering the transitional phases have been performed on the morning transition (Sorbjan, 2007; Beare, 2008) as well as on the evening transition (Sorbjan, 1996, 1997; Beare et al., 2006; Pino et al., 2006). More recently, diurnal cycle studies were conducted by Kumar et al. (2006) and Basu et al. (2008).

According to these studies, which do not consider larger scale external forcings as fronts or local wind systems, the diurnal cycle is prevalent in the wind: During day, a logarithmic wind profile exists in the surface layer whereas a nearly constant wind speed and direction are prevalent above. During the night, the wind is lighter or calm at the ground level. Aloft it can become supergeostrophic with wind speeds between 10 m s^{-1} to 30 m s^{-1} at roughly

200 m altitude. This phenomenon is known as low-level jet (LLJ) and is often accompanied by a rapid change in wind direction. Above the LLJ, the wind speed decreases to the geostrophic value. This decoupling of the wind at night at the cross-over height results from the strong stabilisation of the ABL due to radiative cooling of the ground and is not prevalent during the day due to intense vertical mixing processes (Stull, 1988; Emeis, 2013, 2014).

The diurnal cycle is also prevalent in the turbulent intensity: The CBL is very turbulent, with positive buoyancy representing the main source, whereas weaker sporadic turbulence exists in the SBL, with negative buoyancy as main sink. In supergeostrophic situations, however, turbulence is generated at night by wind shear below the LLJ (Stull, 1988; Emeis, 2013, 2014).

A wind turbine operating in the ABL is therefore exposed to low-level vertical wind shear and wind veer as well as to atmospheric turbulence. All of these characteristics influence v and therefore the useful power. Atmospheric turbulence also has an impact on fatigue loading and life expectancy of a wind turbine (Wharton and Lundquist, 2012; Sathe et al., 2013; Vanderwende and Lundquist, 2012; Dörenkämper et al., 2015). This makes the response of the wind-turbine wake to the turbulent ABL flow crucial to increase the wind energy contribution to the primary energy demand. To explore the response, the impact of turbulence in the flow and especially the impact of the diurnal cycle has to be investigated. Therefore, the focus of this work is on a high-resolution large-eddy simulation (LES), being an approved tool to study the turbulence in the ABL (Bellon and Stevens, 2012a).

Impact of the wind-turbine parameterization

In addition to the modelling of the wind behaviour, a parameterization of the wind-turbine forces is an essential first step for wind-turbine LES. The wind-turbine forces can be parameterized as a disc that can either rotate or not. Alternatively, individual rotating lines represent the blades of the wind turbine. The respective approaches are termed the actuator disc model (ADM) and the actuator line model (ALM). In addition, the wind-turbine forces can be represented by the classical Rankine-Froude theory (Rankine, 1865; Froude, 1889) or the blade-element momentum (BEM) method (Glauert, 1963). The Rankine-Froude approach represents the wind-turbine forces as 1 D thrust force, which is constant over the disc, and no torque is considered. The BEM approach accounts for local blade characteristics in both the axial and the tangential force.

The impact of wind-turbine parameterizations on the wake has been studied in numerical simulations focusing on various aspects:
Mikkelsen (2003) investigated the parameterization of a wind turbine with the ADM and the ALM, extended for a multiplicity of rotor configurations, e.g. a coned or a yawed rotor. Numerous investigations comparing the Rankine-Froude approach to the BEM approach were performed by e.g. Ivanell et al. (2008), Porté-Agel et al. (2010), Wu and Porté-Agel (2011), and Tossas and Leonardi (2013). All of these studies resulted in a near-wake wind field, sensitive to the wind-turbine parameterization, whereas the far-wake structure depends mainly on the background turbulence.

Several studies explored the impact of the distribution of the forces: Ivanell et al. (2008) and Tossas and Leonardi (2013) studied the impact of different smearing parameters of the forces acting on the atmosphere, resulting in numerical instabilities for a tight volume-force distribution at the rotor position. Ivanell et al. (2008), Wu and Porté-Agel (2011), and Gomes et al. (2014) investigated the influence of the number of grid points representing the disc on the wake structure with the result that the wake characteristics are independent of the resolution, if a minimum of ten grid points cover the rotor diameter in the spanwise and the vertical directions. Gomes et al. (2014) also analyzed the effect of the radial dependencies of the applied forces. A strong sensitivity of the near-wake wind field was found in contrast to the far-wake behaviour.

In this work, a modified version of the classical Rankine-Froude ADM, which also accounts for the tangential force, and the BEM method for two different airfoils are applied as wind-turbine parameterizations in the numerical simulations. In addition, systematic investigations of the wake characteristics depending on the two parameterizations, the local blade characteristics, and the rotation of the disc are performed.

Impact of turbulence in the flow

A first important step to increase the wind-energy contribution to the primary energy demand is the investigation of the impact of neutral boundary layer (NBL) turbulence in the flow on the wind-turbine wake. This step requires the development and verification of a turbulence preserving method.

The impact of turbulence in the incoming flow on the structure of the wake has been investigated in experimental studies (Medici and Alfredsson, 2006; Chamorro and Porté-Agel, 2009; Zhang et al., 2012) as well as in numerical simulations (Troldborg et al., 2007; Naughton et al., 2011; Wu and Porté-Agel, 2012; Witha et al., 2014). According to them, the wake structure is strongly influenced by the presence of turbulence in the inflow. In general, a more rapid wake recovery exists for higher turbulence intensity levels of the incoming flow.

Different methods have been applied to generate a turbulent flow field upstream of the wind turbine:
In wind-tunnel experiments, additional roughness elements in front of the wind turbine evoke a turbulent flow, which can be generated by turbulence grids (Medici and Alfredsson, 2006) or obstacles on the floor (Chamorro and Porté-Agel, 2009). Implementing this method in a numerical simulation requires a rather large upstream section, which is computationally expensive, leading to other approaches:
A simple method, avoiding the simulation of atmospheric turbulence, was proposed by Mann (1994), e.g. used in Troldborg et al. (2007). The resulting three-dimensional turbulence field is compact and provides turbulence spectra as theoretically expected and observed in an ABL. The method, however, is not based on a physical model and only offers a synthetic turbulence field (Naughton et al., 2011).

Another approach is to couple meteorological data (e.g. wind speed, wind direction, temperature) from a mesoscale simulation on the microscale LES of the wind turbine. However, the two-way coupling as well as the one-way coupling between mesoscale and microscale models are an active area of research, inducing different problems at the moment (Mirocha et al., 2013; Muñoz-Esparza et al., 2014).

An alternative is the use of a precursor simulation. The wind-turbine simulation is initialized with data from the precursor simulation. There are different requirements to maintain the turbulence during the simulation depending on the boundary conditions.
Applying periodic streamwise boundary conditions requires a buffer zone, which prevents the turbulence in the wake from re-entering the domain and interacting with the wind turbine. Periodic streamwise boundary conditions were used amongst others by Wu and Porté-Agel (2012). They created a neutral ABL flow forced by a streamwise pressure gradient.
Applying open streamwise boundary conditions, the wind-turbine simulation has to be fed continuously with turbulence data from a precursor simulation or a region upstream of the wind turbine to generate a fully developed turbulent flow field. This makes the buffer zone obsolete. Open streamwise boundary conditions were used amongst others by Naughton et al. (2011), Witha et al. (2014), and Dörenkämper et al. (2015). Naughton et al. (2011) ensured a turbulent inflow by prescribing instantaneous velocity components from the precursor simulation at the inflow plane at regular time intervals. This method is accompanied by a large memory requirement. Witha et al. (2014) and Dörenkämper et al. (2015) realized a turbulent inflow for an array of wind turbines in a wind park based on a recycling method after Kataoka and Mizuno (2002). The wind-turbine simulation used the data from the precursor simulation for initialization and persistently extracted turbulence from a region upstream of the wind turbine adding it to the mean inflow profiles. This method requires an extended upstream region.

The difficulties of supplying a turbulent flow field upstream of a wind-turbine represent the starting point for the present thesis. The first important step of this study is to develop and investigate a simple and numerically efficient tool which does not require a buffer zone, a large memory, or an extended domain. The turbulence preserving method is described and applied as new methodology in the first part of this study. It maintains the spectral properties of a realistic background turbulence field in a wind-turbine LES with open streamwise boundary conditions. To ensure this, at each time step of the wind-turbine LES, the flow field is perturbed by velocity fluctuations extracted from only one selected equilibrium state of the precursor simulation of an NBL, which also serves for initialization.

The turbulence preserving method is implemented in the multiscale geophysical flow solver EULAG (Prusa et al., 2008). This LES model resolves all energy containing modes of the turbulent transport and scales larger than the spatial resolution of the computational grid. Only the turbulence of the smallest unresolved scales is parameterized using a subgrid-scale (SGS) closure model. The sensitivity of the numerical results towards different SGS closure models (turbulent kinetic energy (TKE) closure, Smagorinsky closure) as well as an implicit LES (Grinstein et al., 2007) is also explored in the first part of this study as possible application of the turbulence preserving method.

The investigation of the impact of NBL turbulence on wind-turbine wakes, with the development and verification of the turbulence preserving method, constitutes the first goal of this study, with special emphasis on different wind-turbine parameterizations and SGS closure models.

Impact of atmospheric turbulence in the flow

A second important step to increase the wind-energy contribution to the primary energy demand is the investigation of the impact of atmospheric turbulence in the flow on the wind-turbine wake. Atmospheric turbulence depends on the mechanical and thermal production due to shear and buoyancy and the dissipation and is strongly influenced by diurnal cycle variations and surface conditions. To investigate the diurnal cycle impact, the wake response is analyzed in particular for the CBL, the EBL, the SBL, and the MBL during two diurnal cycles over homogeneous surface. To investigate the impact of the surface condition, the wake response is analyzed for the CBL and the SBL over heterogeneous surface and compared to the corresponding situation over homogeneous surface.

Impact of the diurnal cycle

The mechanical and thermal production of atmospheric turbulence due to shear and buoyancy and the dissipation are varying over the course of the day. The impact of the diurnal cycle of the ABL on the wind-turbine wakes has been investigated in experimental studies considering different atmospheric stratifications. In general, the level of atmospheric turbulence is weaker (higher) in the stable (convective) case, resulting in a less rapid (more rapid) wake recovery and a larger (smaller) velocity deficit (Baker and Walker, 1984; Magnusson and Smedman, 1994; Medici and Alfredsson, 2006; Chamorro and Porté-Agel, 2010; Zhang et al., 2012, 2013; Tian et al., 2013; Iungo and Porté-Agel, 2014; Hancock and Pascheke, 2014; Hancock and Zhang, 2015).

Atmospheric stability has often been neglected in wind-energy studies, e.g. Porté-Agel et al. (2010); Calaf et al. (2010a); Naughton et al. (2011); Wu and Porté-Agel (2011, 2012); Gomes et al. (2014). The entrainment of energy and momentum into the wake region and the resulting wake structure, however, strongly depend on the level of atmospheric turbulence in the upstream region of a wind turbine. Therefore, an accurate representation of the diurnal cycle driven ABL flow is required to simulate realistic wake structures and to estimate the efficiency.

Some recent LES studies investigate the impact of different atmospheric stratifications on the wake flow. Among others, an SBL has been considered in Aitken et al. (2014) and a CBL in Mirocha et al. (2014), both studies are performed with the Weather Research and Forecasting (WRF)-LES model. Bhaganagar and Debnath (2014, 2015) studied the effect of an SBL on the wake structure for a single wind-turbine. Dörenkämper et al. (2015) investigated the SBL effect in a wind farm. Mirocha et al. (2015) contrasted stable and convective wind-turbine simulations. Abkar and Porté-Agel (2014) and Vollmer et al. (2016) investigated the effect of convective, neutral and stable stratifications on wake characteristics

and Abkar et al. (2016) performed SBL and CBL simulations of a wind farm during a diurnal cycle. These studies reinforce the results of the experimental studies, resulting in a more rapid recovery of the ambient flow for a higher level of the atmospheric turbulence. Specifically, the ambient flow recovers more rapidly under convective conditions and less rapidly under stable conditions.

Therefore, a CBL and an SBL precursor simulation are necessary to investigate the impact of the convective and the stable stratification on the wake. To include the investigation of the impact of the EBL and the MBL, a diurnal cycle LES of the ABL is essential as precursor simulation for realistic wind-turbine simulations.

A simulation of an idealized ABL over homogeneous surface, characterized by high wind speeds, throughout two full diurnal cycles with periodic streamwise boundary conditions is performed in the second part of this study. This is for two reasons: First, to investigate the diurnal variation of different atmospheric variables relevant to wind-energy research. Second, as precursor simulation for synchronized wind-turbine simulations. Therefore, 2 D slices of the three wind components and the potential temperature are extracted at each time step from this precursor simulation.

The wake response is analyzed for a representative CBL, an EBL, an SBL, and an MBL state of the diurnal cycle. This is the first study which also investigates the wake characteristics of a single wind turbine for the EBL and the MBL. Wind-turbine simulations are also conducted for a further day to exclude any influence of the initial conditions on the first diurnal cycle.

Impact of the surface condition

The heterogeneity of the surface increases the depth of the shear layer near the surface and enhances the atmospheric turbulence due to mechanical turbulence production. Surface heterogeneity can be represented by temperature gradients via surface flux variations as in Kang et al. (2012) and Kang and Lenschow (2014), as well as by surface impacts like a modification of the effective roughness length due to terrain undulations as in Dörnbrack and Schumann (1993), Bou-Zeid et al. (2004), Calaf et al. (2014) or individual resolved roughness elements as in Belcher et al. (2003) and Millward-Hopkins et al. (2012). These studies reveal a considerable impact of surface heterogeneity on wind and turbulence within the blending height, which is defined as the height at which the flow becomes horizontally homogeneous (Wieringa, 1976). Specifically, heterogeneity may result in a transition from convective to shear-dominated regimes in day-time boundary layers.

The impact of an increased surface roughness on the wind-turbine wake structure for the CBL and the SBL regimes is also investigated in the second part of this thesis. For this purpose, a 24-h idealized ABL simulation with a heterogeneous surface is performed, represented by spatially distributed obstacles as roughness elements. The 2 D slices of the three wind components and the potential temperature are extracted from the precursor simulation over heterogeneous surface and are applied in the wind-turbine simulations.

The idealized diurnal cycle simulations over homogeneous and heterogeneous surface lay the groundwork for the investigation of the impact of the diurnal cycle of the ABL and of the surface conditions on wind-turbine wakes, which is the second goal of this study.

Final approach

A third important step to increase the wind-energy contribution to the primary energy demand is the development and successful validation of a simple, numerically efficient, and computationally fast parameterization to analyze the response of the wind-turbine wake to the turbulent ABL flow under different atmospheric conditions.

The first part of this study presents the derivation and implementation of a turbulence preserving method, which maintains the spectral properties of a realistic background turbulence field in wind-turbine simulations with open horizontal boundary conditions. The numerical results of the wind-turbine simulations are tested and validated. The second part offers wake results obtained by typical stages during the diurnal cycle as the CBL, the EBL, the SBL, and the MBL. A combination of both parts, resulting in the consideration of characteristics of the different atmospheric regimes in a modified version of the turbulence preserving method, makes the modified turbulence preserving method appropriate for different thermal stratifications.

The idealized diurnal cycle precursor simulation further offers synchronized wind-turbine simulations of the CBL, the EBL, the SBL, and the MBL. They can serve as benchmark wind-turbine simulations for validation of the modified turbulence preserving method.

The combination of both methods, developed in this thesis, is an important and necessary step: Firstly, wind-turbine simulations considering various atmospheric regimes are essential for current and future applications. Secondly, complete diurnal cycle simulations including the corresponding wind-turbine simulations are computationally extremely expensive.

Therefore, this study presents as final approach and third goal a parameterization as combination of the turbulence preserving method and the ambient atmospheric wind profiles and characteristic turbulence intensity profiles occurring during the diurnal cycle. To achieve this, the turbulence preserving method is extended to a stratification dependent turbulent inflow, and combined with different background wind profiles towards a parameterization of turbulent wind-turbine flows for LES of different thermal stratifications. The spectral energy distribution of the turbulent wind fluctuations of the NBL precursor simulation is still applied. In addition, the turbulent inflow includes a stratification dependent weighting. Both, the stratification related weighting, as well as the background wind profiles result from the idealized diurnal cycle simulation over homogeneous surface. The designed parameterization is successfully validated by comparing the wind-turbine simulations applying the developed parameterization to the synchronized wind-turbine simulations over homogeneous surface.

The developed parameterization does not require a large memory, and extended domain, or a computationally very expensive diurnal cycle precursor simulation to consider all relevant regimes during the diurnal cycle in a wind-turbine LES with open streamwise boundary conditions. Therefore, it offers a simple, numerically efficient, and computationally very

fast tool to analyse the response of the wind-turbine wake to the turbulent ABL flow under different atmospheric conditions.

Thesis approach

To increase the utilization of wind energy and therefore the wind-energy contribution to the primary energy demand, it is crucial to understand how a wind turbine operates under different atmospheric conditions. Therefore, the following three key issues have to be solved and are addressed in this thesis:

- The investigation of the impact of NBL turbulence on wind-turbine wakes with the development and verification of the turbulence preserving method and the implementation and validation of appropriate wind-turbine parameterizations.
- The investigation of the impact of the diurnal cycle of the ABL on wind-turbine wakes, including the evening and morning phases, and, in addition, the impact of the surface condition during the day and the night. Idealized diurnal cycle simulations over homogeneous and heterogeneous surface lay the groundwork for the second part.
- The development and successful validation of a numerically efficient parameterization of turbulent wind-turbine flows for LES of different thermal stratifications to analyze the response of the wind-turbine wake to the turbulent ABL flow. The parameterization uses a stratification dependent turbulent inflow, as extended version of the turbulence preserving method, and combines it with appropriate background wind profiles. The parameterization in this third part combines the turbulence preserving method from the first part with the diurnal cycle simulation data from the second part.

Overview of the thesis

These questions are investigated performing LES simulations with the geophysical flow solver EULAG. The numerical model, the wind-turbine parameterization, the turbulence preserving method, and a description of the ABL simulations are given in Chapter 2. The investigation of the impact of NBL turbulence on wind-turbine wakes follows in Chapter 3. The results of Chapter 3 as well as the corresponding theory from Chapter 2 are published in Englberger and Dörnbrack (2017a). The investigation of the impact of the diurnal cycle of the ABL on wind-turbine wakes is given in Chapter 4. All results of Chapter 4, besides the second diurnal cycle, as well as the corresponding theory from Chapter 2 are published in Englberger and Dörnbrack (2017b). A combination of both, the turbulence preserving method and the idealized diurnal cycle simulation, leads to a numerically efficient parameterization of wind-turbine flows for LES of different thermal stratifications, which is presented in Chapter 5. The results of Chapter 5 are submitted to Englberger and Dörnbrack (2017c). Conclusions are given in Chapter 6.

2 Applied Methods

2.1 Numerical model EULAG

An incompressible, turbulent, and dry ABL flow as well as the flow through a wind turbine are simulated with the multiscale geophysical flow solver EULAG (EUlarian / semi-LAGrangian) (Prusa et al., 2008). A comprehensive description and discussion of EULAG can be found in Smolarkiewicz and Margolin (1998) and Prusa et al. (2008).

The model integrates the following set of non-hydrostatic Boussinesq equations, respectively, the momentum equation 2.1 of the three components in 2.2 - 2.4, the thermodynamic equation in 2.5, and the mass continuity equation in 2.6.

$$\frac{d\mathbf{v}}{dt} = -\boldsymbol{\nabla}\left(\frac{p^{'}}{\rho_0}\right) + \mathbf{g}\frac{\Theta^{'}}{\Theta_0} - \underbrace{2\,\Omega\,(\mathbf{v} - \mathbf{v}_e)}_{\mathbf{F}_{COR}} + \underbrace{\frac{\mathbf{F}}{\rho_0}}_{\mathbf{F}_{WT}} + \underbrace{\mathbf{F}_{\mathbf{v}}}_{\mathbf{F}_{sub}} - \underbrace{\alpha_m \mathbf{v}}_{\mathbf{F}_{het}} + \boldsymbol{\mathcal{V}} \equiv \boldsymbol{\mathcal{R}}^{\boldsymbol{v}}, \quad (2.1)$$

$$\frac{du}{dt} = -\frac{1}{\rho_0}\frac{\partial p^{'}}{\partial x} + f\,(v - ve) + \frac{F_x}{\rho_0} + F_u - \alpha_m\, u + \mathcal{V}_x, \quad (2.2)$$

$$\frac{dv}{dt} = -\frac{1}{\rho_0}\frac{\partial p^{'}}{\partial y} - f\,(u - ue) + \frac{F_{\Theta_y}}{\rho_0} + F_v - \alpha_m\, v + \mathcal{V}_y, \quad (2.3)$$

$$\frac{dw}{dt} = -\frac{1}{\rho_0}\frac{\partial p^{'}}{\partial z} + g\,\frac{\Theta^{'}}{\Theta_0} - \frac{F_{\Theta_z}}{\rho_0} - \alpha_m\, w + \mathcal{V}_z, \quad (2.4)$$

$$\frac{d\Theta^{'}}{dt} = -\mathbf{v}\nabla\Theta_e + F_{\Theta'} - \alpha_h\,\Theta^{'} + \mathcal{H} \equiv \mathcal{R}^{\Theta}, \quad (2.5)$$

$$\boldsymbol{\nabla}\cdot(\rho_0\mathbf{v}) = 0, \quad (2.6)$$

These Boussinesq equations are solved for the Cartesian velocity components $\mathbf{v} = (u, v, w)$ and for the potential temperature perturbations $\Theta^{'} = \Theta - \Theta_e$ (Smolarkiewicz et al., 2007), for a flow with constant density $\rho_0 = 1.1\,\mathrm{kg\ m^{-3}}$ and a constant reference value of the potential temperature $\Theta_0 = 301\,\mathrm{K}$. Height-dependent states $\psi_e(\mathrm{z}) = (u_e(\mathrm{z}), v_e(\mathrm{z}), w_e(\mathrm{z}), \Theta_e(\mathrm{z}))$

enter Eqs. 2.1 - 2.6 in the pressure gradient term, the buoyancy term, the Coriolis term, and as boundary conditions. These background states correspond to the ambient and environmental states. Initial conditions are provided for u, v, w, and the potential temperature perturbation $\Theta^{'}$ in $\psi = (u, v, w, \Theta^{'})$. In the set of equations, d/dt, $\boldsymbol{\nabla}$, and $\boldsymbol{\nabla} \cdot$ represent the total derivative, the gradient, and the divergence, respectively. The factor $p^{'}$ represents the pressure perturbation with respect to the background density, and $\mathbf{g}$ is the vector of acceleration due to gravity. $\mathbf{F}_{COR}$ corresponds to the Coriolis force, with the angular velocity vector of the earth's rotation Ω. The Coriolis force depends on the background winds u_e and v_e and a Coriolis parameter of $f = 1.0 \times 10^{-4}$ s^{-1}. $\mathbf{F}_{sub}$ and $\mathrm{F}_{\Theta'}$ are the large-scale forcings of subsidence and radiative cooling, applied in the ABL simulations. $\mathbf{F}_{sub}$ has a zonal F_u and a meridional F_v component. $\mathbf{F}$ is the turbine-induced force in the wind-turbine simulations with the axial F_x and the tangential F_Θ component. $\mathbf{F}_{het}$ corresponds to the forces related to the flow over heterogeneous surface, with the relaxation terms α_m and α_h. The obstacles in the ABL simulation with heterogeneous surface are included via the immersed boundary method (Smolarkiewicz et al., 2007). A detailed description of F_{WT} is given in Chapter 2.2.1, of F_{sub} in Chapter 2.4.1, and of F_{het} in Chapter 2.4.2. The SGS terms $\mathcal{V}$ and $\mathcal{H}$ symbolise viscous dissipation of momentum and diffusion of heat. The terms $\boldsymbol{\mathcal{R}}^{\boldsymbol{v}}$ and $\mathcal{R}^{\Theta}$ summarize symbolically all forces in the corresponding equations.

The acronym EULAG refers to the ability of solving the equations of motions either in an EUlerian (flux form) (Smolarkiewicz and Margolin, 1993) or in a semi-LAGrangian (advective form) (Smolarkiewicz and Pudykiewicz, 1992) mode, via

$$\psi^{\xi+1} = \mathrm{LE}\left(\psi^{\xi} + \frac{1}{2}\Delta t \mathcal{R}^{\psi}\big|^{\xi}\right) + \frac{1}{2}\Delta t \mathcal{R}^{\psi}\big|^{\xi+1}, \tag{2.7}$$

where $\psi = (u, v, w, \Theta)$, ξ denotes the time step and LE is the corresponding finite-difference operator (semi-Lagrangian/Eulerian). EULAG is at least second-order accurate in time and space (Smolarkiewicz and Margolin, 1998) and is well suited for massively-parallel computations (Prusa et al., 2008). It can be run in parallel up to a domain decomposition in three dimensions.

In general, the geophysical flow solver EULAG owes its versatility to a unique design that combines a rigorous theoretical formulation in generalized curvilinear coordinates (Smolarkiewicz and Prusa, 2005) with non-oscillatory forward-in-time differencing for fluids built on the multi-dimensional positive definite advection transport algorithm (MPDATA), which is based on the convexity of upwind advection (Smolarkiewicz and Margolin, 1998; Prusa et al., 2008) and a robust, exact-projection type, elliptic Krylov solver (Prusa et al., 2008). The flow solver has been applied to a wide range of scales simulating various problems including turbulence (Smolarkiewicz and Prusa, 2002), flow past complex or moving boundaries (Wedi and Smolarkiewicz, 2006; Kühnlein et al., 2012), gravity waves

(Smolarkiewicz and Dörnbrack, 2008; Doyle et al., 2011), or even solar convection (Smolarkiewicz and Charbonneau, 2013). The turbulence closure in the geophysical flow solver EULAG can be described by a TKE model, a Smagorinsky model or an implicit LES, with no turbulence closure model due to not considering the diffusion process. The implicit LES properties of numerical solvers based on MPDATA are documented in e.g. Margolin and Rider (2002), Margolin et al. (2002), and Margolin et al. (2006) for structured grids. A detailed description of an implicit LES is given in Grinstein et al. (2007).

2.2 Wind-turbine parameterization

As mentioned in the Introduction, the parameterization of the wind-turbine forces is an essential first step for wind-turbine LES. In this section, two different wind-turbine parameterizations, a modified version of the Rankine-Froude approach and the BEM method are deduced, applied, and successfully validated as wind-turbine parameterizations A, B, and C. The modified Rankine-Froude approach is termed as wind-turbine parameterization A and can be considered as a simplification of the wind-turbine parameterization B, which corresponds to the BEM method. Wind-turbine parameterization C corresponds also to the BEM method, only the airfoil data refer to a different wind turbine as in wind-turbine parameterization B. Further, a smearing of the wind-turbine forces represented by parameterizations A, B, and C is performed before the application of the forces, to avoid numerical instabilities. Finally, a successful validation of the wind-turbine parameterizations is performed against theoretical wind predictions from 1 D theory for laminar and uniform inflow conditions.

2.2.1 Parameterization of the forces

There are two theories for the force calculation of a wind turbine, the momentum theory and the blade element theory (Manwell et al., 2002; Hansen, 2008).

Momentum theory

The momentum theory calculates the forces at the blades based on the conservation of linear and angular momentum. In the following, V_∞ is the upstream velocity, V_R the velocity at the rotor, and V_W the velocity in the wake, as shown in Fig. 2.1. The same nomenclature is valid for the area A. Further, Δp represents the pressure gradient directly before and behind the rotor, P_R corresponds to the power of the rotor, and P_{wind} to the available power in the wind, whereas F_x corresponds to the axial force and F_Θ to the tangential force.

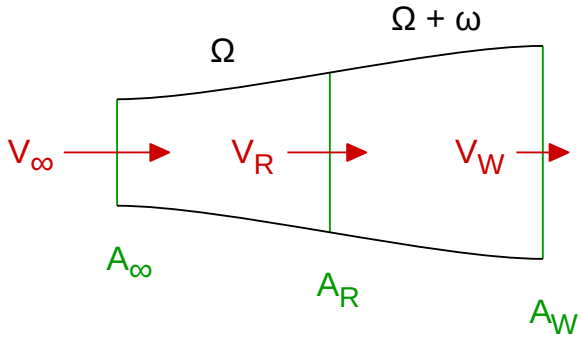

Figure 2.1: Actuator disc model of a wind turbine with the upstream velocity V_∞, the velocity at the rotor V_R, and the velocity in the wake V_W, and likewise the area of the stream tube boundary in the upstream region A_∞, at the rotor A_R, and in the wake A_W. Further, Ω represents the angular velocity of the wind turbine and ω the angular velocity of the flow.

$$
\begin{aligned}
\boldsymbol{F_x} &= A_R\,\Delta p \\
&= \frac{1}{2}\,\rho\,A_R\,(V_\infty^2 - V_W^2) && \text{Bernoulli function: } \Delta p = \frac{1}{2}\,\rho\,(V_\infty^2 - V_W^2) \\
&= \frac{1}{2}\,\rho\,A_R\,V_\infty^2 4a(1-a) && \text{axial induction factor } a := \frac{V_\infty - V_R}{V_\infty} \\
&= \frac{1}{2}\,\rho\,c_T\,A_R\,V_\infty^2 && \text{thrust coefficient: } c_T = \frac{T}{F_{Dyn}} = 4\,a\,(1-a) \\
&= \boldsymbol{\frac{1}{2}\,\rho\,c_T'\,A_R\,V_R^2} && c_T' = \frac{c_T}{(1-a)^2}
\end{aligned}
$$

$$
\begin{aligned}
P_R &= F_x\,V_R \\
&= \frac{1}{2}\,\rho\,A_R\,V_R\,(V_\infty^2 - V_W^2) \\
&= \frac{1}{2}\,\rho\,A_R\,V_\infty^3\,4\,a\,(1-a)^2 \\
&= \frac{1}{2}\,\rho\,c_P\,A_R\,V_\infty^3 && \text{power coefficient: } c_P = \frac{P_R}{P_{wind}} = 4\,a\,(1-a)^2 \\
&= \frac{1}{2}\,\rho\,c_P'\,A_R\,V_R^3 && c_P' = \frac{c_P}{(1-a)^3}
\end{aligned}
$$

$$
\begin{aligned}
\boldsymbol{F_\Theta} &= \frac{P_R}{\Omega r} \\
&= \boldsymbol{\frac{1}{2}\,\rho\,c_P'\,A_R\,\frac{V_R^3}{\Omega r}}
\end{aligned}
$$

If the rotation of the wind-turbine rotor is considered, the flow in the wake rotates in the opposite direction of the rotor, as a consequence of the torque exerted by the flow on the rotor. This results in the following modifications of F_x and F_Θ, where ω represents the angular velocity of the flow, Q the torque, L the angular momentum, I the momentum of inertia, and m the mass.

$$
\begin{aligned}
F_x &= A_R\,\Delta p \\
&= \rho\,A_R\,(\Omega + \frac{\omega}{2})\,\omega\,r^2 && \text{Bernoulli function: } \Delta p = \rho\,(\Omega + \frac{\omega}{2})\,\omega\,r^2 \\
&= \frac{1}{2}\,\rho\,A_R\,\Omega^2\,r^2\,4\,a^{'}\,(1 + a^{'}) && \text{tangential induction factor } a^{'} := \frac{\omega}{2\,\Omega}
\end{aligned}
$$

$$
\begin{aligned}
Q &= \frac{dL}{dt} \\
&= \frac{dm}{dt}\,\omega\,r^2 && L = I\,\omega \text{ and } I = m\,r^2 \\
&= \rho\,A_R\,V_R\,\omega\,r^2 && \frac{dm}{dt} = \rho\,A_\infty\,V_\infty = \rho\,A_R\,V_R = \rho\,A_W\,V_W \\
&= \frac{1}{2}\,\rho\,A_R\,V_\infty\,\Omega\,r^2\;4\,a^{'}\,(1-a)
\end{aligned}
$$

$$
\begin{aligned}
F_\Theta &= \frac{Q}{r} \\
&= \frac{1}{2}\,\rho\,A_R\,V_\infty\,\Omega\,r\;4\,a^{'}\,(1-a)
\end{aligned}
$$

According to this derivation, the momentum theory offers the thrust and the tangential force of the rotor as a function of the flow conditions, included in the axial and tangential induction factors a and $a^{'}$. The 1 D momentum theory or classical Rankine-Froude theory is a simplification of the momentum theory. It was introduced by Froude (1889), who continued the work of Rankine (1865) on the momentum theory of propellers. The theory can be applied to determine the power from an ideal rotor, the thrust of the wind on the ideal rotor, and the effect of the rotor on the wind field. The forces induced by a wind turbine are basically parameterized as a 1 D thrust force. The most important underlying assumptions of the 1 D momentum theory are an infinite number of blades, a uniform thrust over the rotor area, and a non-rotating wake. Despite its simplicity, this non-rotating ADM has been widely used in LES, as it provides reliable results on coarse grids (Calaf et al., 2010b; Porté-Agel et al., 2010; Wu and Porté-Agel, 2011; Tossas and Leonardi, 2013; Meyers and Meneveau, 2013).

A wind turbine rotates and the incoming profiles of the horizontal wind speed are often vertically sheared ($\partial\mathbf{u}/\partial z \neq 0$). Both processes limit the applicability of the simple ADM parameterization by the 1 D momentum theory. To circumvent these limitations and to enable an investigation of the impact of the local blade characteristics by comparing

it to the results of the BEM parameterization, a modified version of the Rankine-Froude ADM is applied, which considers the axial force $F_x(y,z)$ in the streamwise (x) direction and the tangential force $F_\Theta(y,z)$ perpendicular to F_x in the y-z plane, as deduced above, with $u_{i_0,j,k}$ corresponding to V_R and $A_{i_0,j,k}$ to A,

$$|F_x|\big|_{i_0,j,k} = \frac{1}{2}\rho_0 c_T^{'} A_{i_0,j,k}\overline{u_{i_0,j,k}^2}, \tag{2.8}$$

$$|F_\Theta|\big|_{i_0,j,k} = \frac{1}{2}\rho_0 c_P^{'} A_{i_0,j,k}\overline{u_{i_0,j,k}^2}\frac{u_{i_0,j,k}}{\Omega r_{i_0,j,k}}. \tag{2.9}$$

Here, both forces F_x and F_Θ result in the total force $\mathbf{F}\big|_{i_0,j,k}$ in Eq. 2.1 (Hansen, 2008), with

$$\mathbf{F}\big|_{i_0,j,k} = \mathbf{F}_x\big|_{i_0,j,k} + \mathbf{F}_\Theta\big|_{i_0,j,k}, \tag{2.10}$$

with

$$F_{\Theta_y} = F_\Theta \frac{L_y}{r},$$
$$F_{\Theta_z} = F_\Theta \frac{L_z}{r},$$

in Eqs. 2.3 and 2.4, where the centre of the rotor is defined by the grid-point coordinates i_0, j_0, and k_h with j_0 corresponding to the centre of the domain in y-direction and k_{hub} to the grid point at hub height z_{hub} of the rotor. L_y (L_z) corresponds to the lateral (vertical) distance from a certain grid point towards the lateral (vertical) rotor axis. In Eqs. 2.8 and 2.9, $r_{i_0,j,k}$ is the radial position inside the rotor ($0 \leq r_{i_0,j,k} \leq R$), with $R = D/2$ and D representing the diameter of the wind-turbine rotor. The time-averaged value of the squared streamwise velocity component at the rotor position i_0, j, k is denoted by $\overline{u_{i_0,j,k}^2}$.

Blade element theory

The blade element theory calculates the forces at the blades as a function of blade geometry, based on the lift and drag coefficients c_L and c_D and the angle of attack α. The geometrical relations of the following derivation follow from Fig. 2.2*b*, which represents the cross section of an airfoil, as shown in Fig. 2.2*a*. Here, B represents the number of blades of the rotor, c the chord length, F_n the normal and F_t the tangential force, Φ the angle of relative wind, which is composed of the pitch angle Θ and α to $\Phi = \Theta + \alpha$, V_x the axial velocity, and V_Θ the tangential velocity.

$$\begin{aligned}
\boldsymbol{dF_x} &= B\ dF_n \\
&= B\ (dF_L\, cos\Phi\ +\ dF_D\, sin\Phi) \\
&= \boldsymbol{\frac{1}{2}\,\rho\,\frac{B\,c}{2\pi\,r}\,dA\,(c_L\,cos\Phi\ +\ c_D\,sin\Phi)\,\frac{V_\infty^2\,(1\ -\ a)^2}{sin^2\Phi}}
\end{aligned}$$

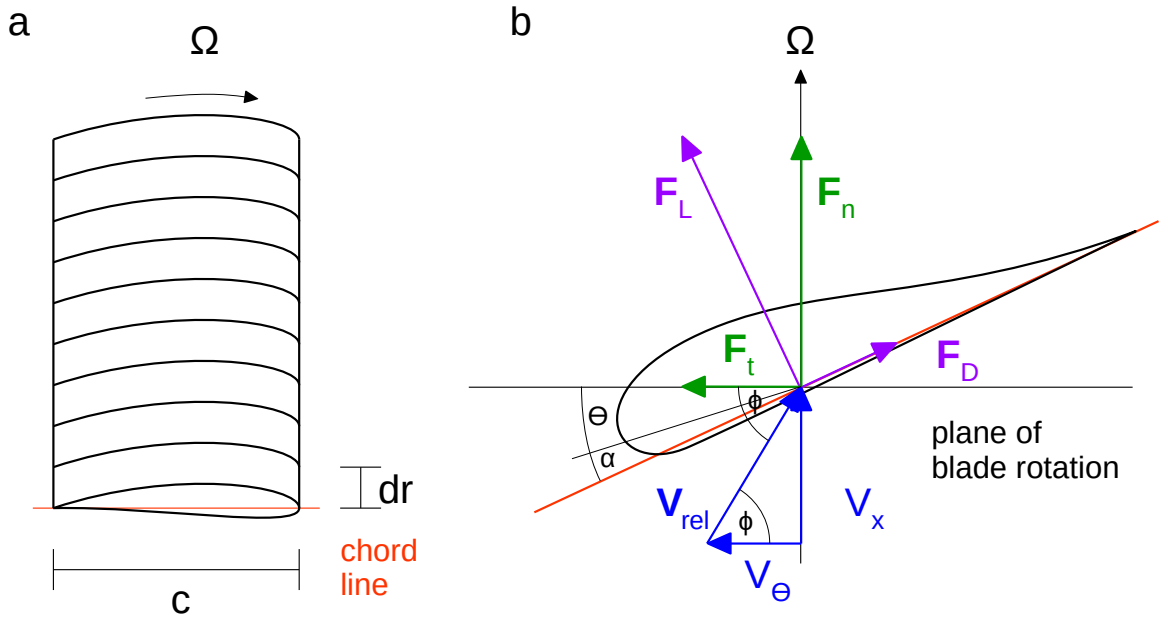

Figure 2.2: Schematic of the blade elements of an airfoil with the chord length c, the radial length of an element dr , and the angular velocity of the wind-turbine rotor Ω in a. Blade geometry of a wind turbine with the relative velocity $\mathbf{V}_{rel}$, the axial and tangential velocities V_x and V_Θ, the drag and the lift force $\mathbf{F}_D$ and $\mathbf{F}_L$ and the normal and tangential force $\mathbf{F}_n$ and $\mathbf{F}_t$. Further, Φ corresponds to the angle of relative wind, Θ to the pitch angle, and α to the angle of attack, with $\Phi = \Theta + \alpha$ and $\Theta(r)$ in b.

$$
\begin{aligned}
\boldsymbol{dF_\Theta} &= B\, dF_t \\
&= B\, (dF_L\, sin\Phi \,+\, dF_D\, cos\Phi) \\
&= \frac{\mathbf{1}}{\mathbf{2}}\, \boldsymbol{\rho}\, \frac{\boldsymbol{B\, c}}{\boldsymbol{2\pi\, r}}\, \boldsymbol{dA}\, (\boldsymbol{c_L\, sin\Phi} \,+\, \boldsymbol{c_D\, cos\Phi})\, \frac{\boldsymbol{V_\infty\, (1 \,-\, a)\, \Omega\, r\, (a \,+\, a')}}{\boldsymbol{sin\Phi\, cos\Phi}}
\end{aligned}
$$

with:

$$
\begin{aligned}
dF_L &= \frac{1}{2}\, \rho\, c_L\, V_{rel}^2\, c\, dr \\
dF_D &= \frac{1}{2}\, \rho\, c_D\, V_{rel}^2\, c\, dr \\
dA &= 2\pi\, r\, dr \\
tan\Phi &= \frac{V_x}{V_\Theta} \\
V_x &= V_\infty\, (1 \,-\, a) \\
V_\Theta &= \Omega\, r \,+\, \frac{\omega}{2}\, r \,=\, \Omega\, r\, (1 \,+\, a')
\end{aligned}
$$

This represents a great improvement of the momentum theory, as it enables calculation of the steady loads as well as the thrust and the power for different wind speeds, rotational speeds, and pitch angles of the blades. The most important assumption of the blade element theory is the division of the blade into individual sections with no aerodynamic interaction between. The axial and tangential forces of the blade element theory are represented in Eqs. 2.11 and 2.12, as deduced above, with $u_{i_1,j,k}$ representing V_∞ and $A_{i_0,j,k}$ to A,

$$\begin{aligned} |F_x|\big|_{i_0,j,k} &= \frac{1}{2}\rho_0 \frac{Bc}{2\pi r_{i_0,j,k}}(c_L \cos\Phi + c_D \sin\Phi) \\ &\quad \times A_{i_0,j,k} \frac{u_{i_1,j,k}^2 (1-a)^2}{\sin^2\Phi} \end{aligned} \tag{2.11}$$

$$\begin{aligned} |F_\Theta|\big|_{i_0,j,k} &= \frac{1}{2}\rho_0 \frac{Bc}{2\pi r_{i_0,j,k}}(c_L \sin\Phi - c_D \cos\Phi) \\ &\quad \times A_{i_0,j,k} \frac{u_{i_1,j,k}(1-a)\Omega r_{i_0,j,k}(1+a')}{\sin\Phi\cos\Phi}. \end{aligned} \tag{2.12}$$

Here, the upstream velocity $u_{i_1,j,k}$ is taken at the first upstream grid point in the x-direction and the corresponding y and z coordinates. With the exception of ρ_0 and B, all other parameters appearing in Eqs. 2.11 and 2.12 depend on the radius $r_{i_0,j,k}$ and vary spatially.

Blade element momentum theory

The blade element momentum theory by (Glauert, 1963) is the combination of the momentum theory (flow conditions in a, a') and the blade element theory (blade conditions in c, Θ, c_L, c_D). The axial and tangential forces can be solved via an iteration procedure, following (Hansen, 2008).

Input: $c(r)$, $\Theta(r)$, V_∞, Ω

Step 1: $a = 0$; $a' = 0$

Step 2: $tan\Phi = \dfrac{V_\infty (1 - a)}{\Omega r (1 + a')}$

Step 3: $\alpha = \phi - \Theta$

Step 4: c_L and c_D for α from table

Step 5: $c_n = c_L cos\Phi + c_D sin\Phi$
$c_t = c_L sin\Phi - c_D cos\Phi$

Step 6: $$a = \frac{1}{F\,\frac{4\,sin^2\Phi}{\frac{B\,c}{2\pi\,r}\,c_n} + 1}$$

$$a' = \frac{1}{F\,\frac{4\,sin\Phi\,cos\Phi}{\frac{B\,c}{2\pi\,r}\,c_t} - 1}$$

Prandtl's tip loss factor F to correct the assumption of an infinite number of blades

$$F = \frac{2}{\pi} cos^{-1}\left(exp\left(-\frac{\frac{B}{2}\,(R - r)}{r\,sin\Phi}\right)\right)$$

Step 7: If a and a' has changed more than a certain tolerance, go to Step 2, or else finish with Step 8.

Step 8: Compute F_x and F_Θ of the blade element theory.

Applied parameterizations

In this work, the modified version of the Rankine-Froude ADM as well as the BEM parameterization are implemented via Eq. 2.10 in the geophysical flow solver EULAG. The forces are treated implicitly in the numerical scheme according to Eq. 2.7. In EULAG, the rotor of a wind turbine is not implemented as a real circular obstacle (e.g. grid-point blocking as in Heimann et al. (2011)) or a permeable rotor (Witha et al., 2014; Tossas and Leonardi, 2013; Gomes et al., 2014). Instead, at every grid point covered by the rotor, the velocity field experiences the turbine-induced force $\mathbf{F}_{WT}$ according to Eq. 2.1. This implementation is inspired by the immersed boundary method, successfully applied in EULAG by Smolarkiewicz and Winter (2010). The immersed boundary method is described in detail later in this chapter for the heterogeneous surface simulation. The implicit treatment of the forces in Eq. 2.7 has a positive effect on the time step, because there are no large velocity gradients between the rotor area and its surroundings.

Altogether, three different parameterizations of wind-turbine induced forces are implemented in EULAG. The respective wind-turbine parameterizations A, B, and C are listed together with their main characteristics in Table 2.1:
Wind-turbine parameterization A represents the modified version of the Rankine-Froude ADM, hereafter referred to as modified momentum theory (MMT). It can be applied for a rotating actuator with $F_\Theta \neq 0$ or for a non-rotating actuator with $F_\Theta = 0$. Wind-turbine parameterization A can be regarded as a simplified version of wind-turbine parameterization B, as the values of $c'_{T_{blade}} = 1.27$ and $c'_{P_{blade}} = 0.87$ in Eqs. 2.8 and 2.9 are deduced from wind-turbine parameterization B. These prescribed values are comparable to Meyers and Meneveau (2013).

Table 2.1: The crucial characteristics of the three different wind-turbine parameterizations A, B, and C applied in this study, using the MMT or the BEM theory as wind-turbine parameterization.

wind-turbine parameterization	A	$B + C$
name	MMT	BEM
characteristics	Eq. 2.8	Eq. 2.11
	Eq. 2.9	Eq. 2.12

Table 2.2: List of the BEM method parameters used in wind-turbine parameterization of type B (10 MW reference wind turbine from DTU) (Mark Zagar (Vestas), personal communication, 2015) and type C (three-blade GWS/EP-6030x3 rotor) (Wu and Porté-Agel, 2011). The radius r and the chord length c of the two rotors are scaled to a rotor diameter of 100 m.

parameterization B			parameterization C		
r / m	$c(r)$ / m	$\Theta(r)$ / °	r / m	$c(r)$ / m	$\Theta(r)$ / °
5.0	5.3	13.3	6.7	9.3	20.5
10.0	6.0	13.2	13.3	9.8	20.9
15.0	6.2	10.5	20.0	9.8	19.8
20.0	5.8	9.0	26.6	9.4	16.9
25.0	5.0	7.3	33.3	8.7	13.2
30.0	4.5	5.5	40.0	7.9	10.7
35.0	3.5	3.8	46.7	6.8	9.1
40.0	3.0	2.5	50.0	4.0	6.7
45.0	2.3	1.3			
50.0	1.0	0.2			

The BEM method, applied in wind-turbine parameterizations B and C, is used to investigate the influence of the blade structure. The wind-turbine parameterizations B and C are essentially the same, only the airfoil data applied in B and C differ. The airfoil data are taken from two different wind turbines: The 10 MW reference wind turbine from DTU (Technical University of Denmark) referred to as wind-turbine parameterization B (Mark Zagar (Vestas), personal communication, 2015) and the three-blade GWS/EP-6030x3 rotor (Wu and Porté-Agel, 2011) referred to as wind-turbine parameterization C. For both wind turbines, the rotor radius as well as the chord length of the blades are scaled to a rotor diameter of 100 m, to make the results comparable to each other. The most relevant wind-turbine parameters used for wind-turbine parameterizations B and C are listed in Table 2.2.

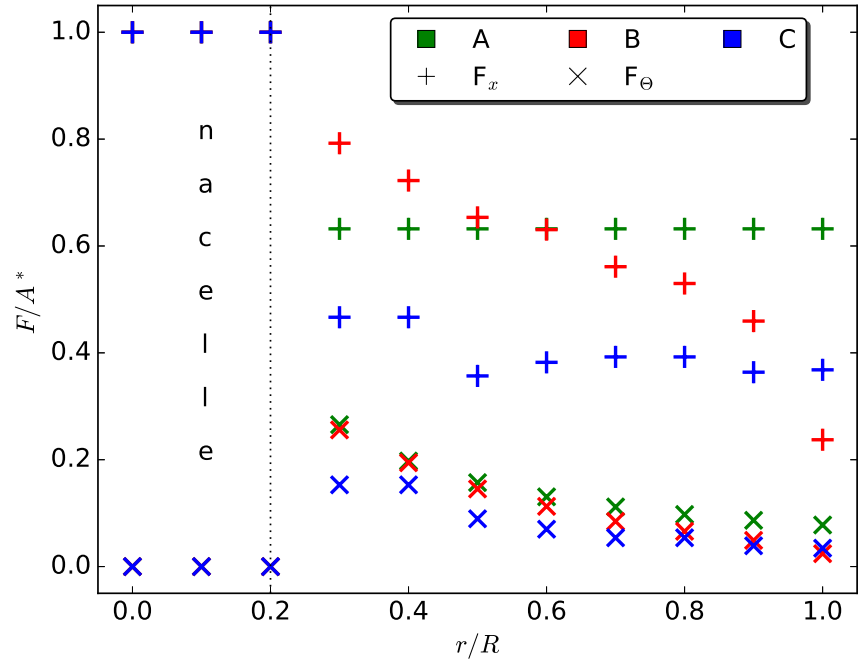

Figure 2.3: Radial distributions of the axial and tangential forces F_x and F_Θ normalized by the area A^* for the different wind-turbine parameterizations A, B, and C of Table 2.1. The values of F_x and F_Θ are normalized by the maximum of the axial force at the nacelle, which is the same in all three wind-turbine parameterizations. The axial forces are represented by (+) and the tangential forces by (×). They are plotted for each discrete position of the rotor, assuming 21 grid points are covering the rotor with radius R. The nacelle covers 20 % of the blades, denoted by the dotted vertical line. For the calculation of the forces in these schematic illustration, a rotor diameter of 100 m is assumed, together with a rotation frequency $\Omega = 7$ r.p.m. and a constant upstream velocity $u_{i_1,j,k} = 8$ m s^{-1}.

The radial distributions of the respective axial and tangential forces of wind-turbine parameterizations A, B, and C are depicted in Fig. 2.3. In each wind-turbine parameterization, a nacelle is represented within $r/R \leq 0.2$ by a stronger drag force in comparison to the blade values and no lift force. The size of the parameterized nacelle is large compared to a real wind turbine, because the numerical resolution demands enough grid points representing the nacelle to avoid instabilities. For the nacelle, $c'_{T_{nacelle}} = 1.48$ and $c'_{P_{nacelle}} = 0$ are chosen in all three parameterizations. A value of the drag coefficient of the nacelle of 1.0 agrees with the drag coefficient interval of cylindrically shaped bluff bodies between 0.8 and 1.2 (Schetz and Fuhs, 1996), and has also been used e.g. in El Kasmi and Masson (2008). A tower is not considered in the wind-turbine parameterizations as it is not the major source of turbulence.

2.2.2 Application of the forces

The numerical simulations conducted in this study are performed on an equidistant Cartesian mesh with grid spacings Δx, Δy, and Δz, in the streamwise, lateral, and vertical directions, respectively. It must be noted, that all wind-turbine parameterizations A, B, and C are coded to perform properly in terrain-following coordinates with variable vertical grid spacings over hilly terrain, as applied in Heimann et al. (2017).

To calculate the forces of the actuator, polar coordinates serve as a local mesh. The centre coordinate of the polar mesh is the centre of the rotor. From this position, the polar mesh is described by a very fine grid with $\Delta r = R/1000$ as radial step size and $\Delta\varphi = 1\,^\circ$ as azimuthal step size. The step sizes in the radial and azimuthal directions are fine enough to minimize the errors that would result from calculating the forces on a Cartesian mesh (Ivanell et al., 2008). The computational costs arising from such a fine polar mesh are insignificant, as the disc is always at the same position, making this calculation of the actuator force in polar coordinates $F_{r,\Theta,z}$ only necessary once.

The force acting on each polar grid point $F_{r,\Theta,z}$ is transformed to the corresponding force in Cartesian coordinates $F^*_{i,j,k} = F^*_{x,y,z} = \mathcal{M}_{x,y,z} \cdot F_{r,\Theta,z}$ through the transformation matrix $\mathcal{M}_{x,y,z}$. The force $F^*_{i,j,k}$ contributes to a certain fraction $\mu \in [0,1]$ to the actuator force $F_{i,j,k} = \mu \cdot F^*_{i,j,k}$. The fraction μ is determined by the ratio of the grid-cell volume of the polar coordinate and the corresponding Cartesian coordinate, i.e. $\mu = 1$ if the Cartesian grid point is completely covered by the rotor and $\mu = 0$ in case of a rotor-free grid point. At the edge of the rotor, the fraction $\mu < 1$, because the Cartesian grid cell is not completely covered by the local polar mesh representing the rotor.

A smearing of the turbine-induced forces in the axial as well as in the radial direction is necessary to avoid numerical instabilities. As a first step, the forces from Eq. 2.10 are additionally distributed in the streamwise direction. This approach is performed for all parameterizations. The forces in Eq. 2.10 are smeared with a 1 D Gaussian function in the x-direction,

$$F_{s_x} = \frac{1}{\sqrt{\pi}\sigma} \exp\left(-\frac{(x(i) - x(i_0))^2}{\sigma^2}\right). \tag{2.13}$$

Similar to Meyers and Meneveau (2013), the value of σ is set to 1.5 and is given in absolute values of the radius.

In wind-turbine parameterization A, the axial force F_x in the y-z plane only varies with the incoming velocity across the rotor. A moderate velocity gradient results in very similar F_x values, generating large gradients at the edges of the rotor. Therefore, an additional two-dimensional smearing $F_{s_{y-z}}$ in the y-z plane is introduced to avoid too sharp radial gradients in the turbine-induced forces between the rotor area and the immediate surroundings. The forces of the schematic illustration in Fig. 2.3 decrease with a step function over the last three grid points $\in [0.8\,r/R, 1.0\,r/R]$. The force at each of these outer region grid

points is half of the force of the corresponding nearest inner neighbour grid point. $F_{s_{y-z}}$ is not applied for the forces in the BEM method, as the parameters in Eqs. 2.11 and 2.12 already decrease with increasing r.

The values of the smearing parameters and of the step function applied on the forces in the y-z plane in wind-turbine parameterization A are chosen in such a way that the integrated force distributed in three dimensions is the same as in the two-dimensional case without smearing. By combining the smearing in the x-direction F_{s_x} and the smearing in the y-z plane $F_{s_{y-z}}$, the difference of the forcings between a 2 D and a 3 D disc is less than 1 % for 21 grid points per disc and decreases for a finer resolution.

The parameterization $\mathbf{F}\big|_{i_0,j,k}$ (Eq. 2.10) together with the coordinate transformation $F_{i,j,k}$ and the applied smearing in the axial F_{s_x} and radial $F_{s_{y-z}}$ directions result in a total parameterized force,

$$\mathbf{F}\big|_{i,j,k} = \mathbf{F}\big|_{i_0,j,k} \cdot F_{i,j,k} \cdot F_{s_x} \cdot F_{s_{y-z}}, \tag{2.14}$$

where the wind-turbine induced force $\mathbf{F}\big|_{i,j,k}$ corresponds to the force $\mathbf{F}$ in Eq. 2.1.

2.2.3 Validation of the wind-turbine parameterization

A validation of the numerical results for the wind-turbine parameterizations A, B, and C at the rotor position (i_0, j, k) and in the wake (i_w, j, k), whereby $i_w \geq i_0$, are possible with theoretical wind predictions from the 1 D momentum theory,

$$u_{i_0,j,k} = u_{i_1,j,k}(1-a), \tag{2.15}$$

$$u_{i_w,j,k} = u_{i_1,j,k}(1-2a), \tag{2.16}$$

where a is the axial induction factor defined as

$$a := \frac{u_{i_1,j,k} - u_{i_0,j,k}}{u_{i_1,j,k}}. \tag{2.17}$$

Equation 2.15 follows directly from Eq. 2.17, and Eq. 2.16 can be derived from the Bernoulli equation and Newton's second law of motion (Hansen, 2008). This comparison is strictly applicable only for laminar and uniform inflow conditions $u_{i_1,j,k}$ $(du/dz = 0)$.

Numerical simulations are performed on 512 × 128 × 128 grid points with a horizontal and a vertical resolution of 0.1 m. The rotor of the wind turbine is located at 12 m in x-direction and centred in y-direction with a diameter D and a hub height z_h of 4 m. The following simulations are performed with different axial induction factors $a = 1/3$, 1/4, 1/5 for all wind-turbine parameterizations. Exemplary, the results for wind-turbine parameterization A, a non-rotating disc and $u_{i_1,j,k} = 0.08$ m s^{-1} are listed in Table 2.3. The results for wind-turbine parameterizations B and C and for a different upstream velocity of $u_{i_1,j,k} = 0.10$ m s^{-1} are quantitatively similar and therefore not shown here.

Table 2.3: Theoretically predicted velocities for different axial induction factors a at the rotor position $u_{i_0,j,k}$ and in the wake $u_{i_w,j,k}$ scaled with the upstream velocity $u_{i_1,j,k}$ according to Eqs. 2.15 and 2.16 and the deviations obtained from the numerical simulations. The deviations are calculated as an average over the disc area.

a	$\frac{u_{i_0,j,k}}{u_{i_1,j,k}}$ expected	$\frac{u_{i_0,j,k}}{u_{i_1,j,k}}$ deviation	$\frac{u_{i_w,j,k}}{u_{i_1,j,k}}$ expected	$\frac{u_{i_w,j,k}}{u_{i_1,j,k}}$ deviation
1/3	0.67	2 %	0.33	5 %
1/4	0.75	0 %	0.50	0 %
1/5	0.80	2 %	0.60	4 %

The simulated ratios of $u_{i_0,j,k}/u_{i_1,j,k}$ and $u_{i_w,j,k}/u_{i_1,j,k}$ for a realistic value of the axial induction factor of 1/4 are in complete agreement with the 1 D momentum theory. For larger ($a = 1/3$) and smaller ($a = 1/5$) a values, the simulation results deviate by 5 % or less from the theoretical predictions.

Summarizing, a successful validation of the LES model EULAG follows for the non-rotating disc of wind-turbine parameterization A and realistic values of the axial induction factor against the 1 D momentum theory and of wind-turbine parameterizations B and C against the BEM method.

2.3 Turbulence Preserving Method

As stated in the Introduction, one of the difficulties of an LES of a single wind turbine is the supply of a turbulent flow field upstream of the wind turbine. In this section, the turbulence preserving method is introduced as new methodology to preserve the background turbulence in an LES of a flow through a wind turbine. The basic idea is to extract velocity perturbations from a precursor simulation of the NBL. The velocity fields are used to disturb the wind-turbine simulation in a special manner as described below. For this purpose, a precursor simulation of the turbulent NBL has to be conducted.

2.3.1 Precursor simulation

To drive the NBL flow, an additional forcing $-u_*^2/H$ is applied in Eq. 2.2, where H is the height of the computational domain. Sensitivity tests revealed that a value of the friction velocity $u_* = 0.4$ m s^{-1} results in a realistic pressure gradient of the ABL. This forcing is comparable to the streamwise mean pressure gradient force applied in Wu and Porté-Agel (2012). The precursor simulation is performed with the same number of grid points as the

wind-turbine simulations, in which the turbulence preserving method is applied, but with periodic horizontal boundary conditions. The initial wind speed is set to zero, and the drag coefficient in the surface parameterization is set to 0.1.

Applying only the above forcing, it is a long lasting process until the precursor simulation is in an equilibrium state. Additional velocity gradients in the neutral flow can serve as a trigger, breaking the symmetry, and acting as a seed for turbulence to develop. Therefore, the precursor simulation is disturbed by inserting an obstacle in the domain for a few time steps. The flow around this obstacle enhances the velocity gradients in the NBL flow, and the equilibrium state of the precursor simulation is attained more rapidly.

2.3.2 Turbulence preserving method

The perturbation velocities $\mathbf{u}_p^*\big|_{i,j,k}^{\xi}$ are extracted from the precursor simulation according to,

$$\mathbf{u}_p^*\big|_{i,j,k}^{\xi} = \alpha \cdot \beta \cdot \underbrace{\left(\mathbf{u}_p\big|_{i^*,j,k} - \underbrace{\frac{1}{n \cdot m} \sum_{i=1}^{n} \sum_{j=1}^{m} \mathbf{u}_p\big|_{i,j,k}}_{I} \right)}_{II}, \tag{2.18}$$

where $\mathbf{u}_p\big|_{i^*,j,k}$ is the velocity vector of the precursor simulation in an equilibrium state and the term I in Eq. 2.18 denotes the height-averaged mean value of the corresponding wind component at each grid point i, j, and k. The index of the grid points are denoted by $i = 1 \ldots n$, $j = 1 \ldots m$, and $k = 1 \ldots l$ in the x, y, and z directions, respectively.
The perturbation velocity from Eq. 2.18 contributes to the velocity field of the wind-turbine simulation $\mathbf{u}\big|_{i,j,k}^{\xi}$ at the initial time step $\xi = 0$ and at each following time step ξ. The values of the precursor simulation $\mathbf{u}_p\big|_{i^*,j,k}$ are shifted in the streamwise direction by one grid point every time step ξ, symbolized by $i^* = i + \xi^*$, with $i^* \in [1, n]$ and ξ^* representing the number of time steps since the start of the simulation. Furthermore, the difference as denoted by II in Eq. 2.18 is multiplied with a random number β ranging from -0.5 to 0.5. Both, the grid point shift and the random number multiplication, are necessary to only apply the spectral energy distribution of the precursor simulation instead of impressing individual flow patterns onto the wind-turbine simulation. To account for different magnitudes of the background turbulence, the term II in Eq. 2.18 is additionally multiplied by a factor α, representing the amplitude of the turbulence perturbations (hereafter referred to as perturbation amplitude).

Applying this method maintains the spectral properties of the turbulent fluctuations in the wind-turbine simulation. It offers several possibilities for the numerical scheme:

1. Periodic boundary conditions and a buffer zone can be avoided, enabling open inflow and outflow Neumann boundary conditions. Further, an extended upstream region can also be avoided. Both effects are minimising the domain size of the simulation.
2. The perturbation data from the precursor simulation are imported only once and are stored in three 3 D fields (u, v, w) during the wind-turbine simulation. This makes a permanent import of turbulence data from a precursor simulation obsolete, reducing the memory requirement.
3. The method is computationally very efficient, as it allows to reapply the background turbulence of one precursor simulation to a variety of wind-turbine simulations.
4. The response of a wind turbine to different intensities of the background turbulence can be easily investigated by changing the parameter α in Eq. 2.18.

2.3.3 Validation of the turbulence preserving method

A simulation applying term I from Eq. 2.18 as wind field is performed. In addition, the spectral energy distribution of the precursor simulation is applied with the prescribed methodology. After integrating for the same amount of time as in the following wind-turbine simulations, this simulation resulted in the same values of $\overline{u}$, $\overline{v}$ and $\overline{w}$, as well as σ_u, σ_v and σ_w with $\sigma_i = \sqrt{i'^2}$ as the precursor simulation, validating the mechanism of the turbulence preserving method.

2.4 Atmospheric boundary-layer simulations of the diurnal cycle

In this section, the setup of the ABL diurnal cycle simulations is described in detail. The diurnal cycle data are essential to perform the wind-turbine simulations, answering the problem of how a wind turbine reacts under different atmospheric conditions, as mentioned in the Introduction. Therefore, a detailed description of the interface between ABL and wind-turbine simulations is given in the following. Finally, the successful validation of one ABL diurnal cycle simulation of the BLLAST (Boundary Layer Late Afternoon and Sunset Turbulence) field experiment gives confidence in the ABL diurnal cycle simulations performed with EULAG.

2.4.1 External forcing

Infrared radiation at night and solar radiation at day trigger the diurnal cycle. The resulting cooling at night and warming during the day time can be prescribed by the sensible heat

flux. It arises from the solar radiation or infrared irradiation value divided by ρ_0 and the specific heat capacity at constant pressure and contributes to $\mathcal{H}$ in Eq. (2.5) via the SGS closure model.

For a realistic simulation of the diurnal cycle (ABL height, temperature, turbulence evolution), it is important to model and integrate additional external forcings, representing mesoscale and synoptic scale processes, into the LES. Subsidence and radiative cooling of the atmosphere are selected as dominant large-scale external forcing processes. They impact on the geophysical flow solver EULAG via Eqs. (2.1) and (2.5).

Subsidence damps vertical motions at scales larger than the mixed layer height, especially during convective conditions, limiting the growth of the ABL and influencing temperature and turbulence in simulations of the ABL (Mirocha and Kosović, 2010; Blay-Carreras et al., 2014; Mazzitelli et al., 2014). It acts on the zonal and meridional wind components u and v, and on the potential temperature perturbation $\Theta^{'}$, and consists of the product of a subsidence velocity w_{sub} and the vertical derivative of $\Phi = (u, v, \Theta^{'})$, representing the wind components or the potential temperature perturbation according to

$$S^{\gamma}_{i,j,k} = w_{sub}\frac{d\Phi}{dz} = w_{sub}\frac{\Phi_{i,j,k+1} - \Phi_{i,j,k}}{z_{i,j,k+1} - z_{i,j,k}}. \tag{2.19}$$

The vertical gradient in Eq. (2.19) controls the height of the ABL, whereas the magnitude of the subsidence velocity influences the strength of this change. The subsidence process is included as $S^u{=}F_u$ and $S^v{=}F_v$ in Eq. (2.1), whereas $S^{\Theta^{'}}$ contributes to $F_{\Theta'}$ in Eq. (2.5).

The subsidence applied on the potential temperature perturbation in Eq. (2.5) leads to a warming of the ABL air. This effect is compensated by radiative cooling of the atmosphere (Bellon and Stevens, 2012b). A constant radiative cooling with height is applied on $\mathrm{F}_{\Theta'}$ in Eq. (2.5), which acts in all levels and grid points besides at the ground and the top.

2.4.2 Setup of the diurnal cycle simulations

There are different numerical requirements for ABL simulations representing a stable or a convective atmospheric state. An SBL simulation requires a fine spatial resolution to represent the small eddies, and a small computational domain is sufficient. A CBL simulation requires a large domain to capture the energy-containing thermals, and a coarse computational grid is sufficient.

A combination towards ABL simulations with a large domain with a rather fine resolution is computationally very expensive, but it is useful if the ABL simulation is performed as precursor simulation of a wind-turbine simulation.

Idealized ABL simulation over homogeneous surface

The idealized ABL simulation over homogeneous surface is performed with periodic horizontal boundary conditions on 512 × 512 grid points in the horizontal with a resolution of 5 m for 54 h, representing two full diurnal cycles. The vertical resolution is 5 m in the lowest 200 m, 10 m up to 800 m, and 20 m approaching the domain top at 2 km. The simulation is initialised with a wind of 10 m s^{-1} in the zonal (east - west, streamwise) direction and zero for the meridional (north - south, spanwise, lateral) direction, and no vertical wind component. The ambient potential temperature $\Theta_e(z)$ of 300 K is constant up to 1 km and changes with height above according to a lapse rate of 10 K km^{-1}. The profile sensible heat flux used in the idealized ABL simulation at the surface is shown in Fig. 4.1*a* with a minimum of -10 W m^{-2} during the night and a maximum of 140 W m^{-2} at noon. Further, no additional external forcings were included, because this simulation is not aiming to agree exactly with measurements and most of the presented analysis focuses on the operating height of a wind turbine ($z \leq 200$ m), which is mostly unaffected by subsidence and radiative cooling. This idealized ABL simulation is performed over homogeneous surface with a drag coefficient of 0.1, which enters the SGS momentum flux in Eq. 2.1. The computational costs of the idealized ABL simulation representing 54 h add up to 23 days, performed on 256 Intel Xeon E5-2697 v3 threads at 2.6 GHz.

Idealized ABL simulation over heterogeneous surface

In an additional simulation, the first 24 h of the diurnal cycle are simulated using a heterogeneous surface, covered by obstacles representing for example individual patches of different land use or buildings. The individual obstacles have a size of 20 m x 20 m x 5 m and are separated from one another in the zonal and meridional direction by 20 m, an arrangement similar to Belcher et al. (2003, Fig. 1). This results in a density of the surface of 25%, which is considered to be appropriate for this investigation, as wind turbines are placed outside central city areas with a surface density of approximately 50% (Millward-Hopkins et al., 2012). The obstacles are implemented via the immersed boundary method (Smolarkiewicz et al., 2007) in Eqs. 2.1 - 2.5. This method mimics the presence of solid structures and internal boundaries by applying the fictitious body forces $-\alpha_m \mathbf{v}$ in Eq. 2.1 and $-\alpha_h \Theta'$ in Eq. 2.5. In the fluid away from the solid boundaries, α_m and α_h are both zero, whereas $\alpha_{(m/h)} = 1/2 \Delta t$ within the solid, assuring the velocity approaching zero, with the time step Δt. The immersed boundary method in EULAG has been successfully applied in Schröttle and Dörnbrack (2013), von Larcher and Dörnbrack (2014), and Gisinger et al. (2015).

BLLAST ABL simulation

A different setup can be applied to reduce the computational costs for a pure diurnal cycle ABL simulation, which is not used as precursor simulation for wind-turbine simulations. The SBL is initialized with a horizontal resolution of 6.25 m on 128 × 128 grid points

with periodic horizontal boundaries. For the transition from an SBL towards a CBL the domain expansion method of Beare (2008) is applied, resulting in a horizontal resolution of 25 m on 128 x 128 grid points in the CBL. For the transition back from the coarse to the fine resolution the domain size is kept constant and the horizontal resolution is decreased to 6.25 m by performing an interpolation procedure, resulting in 512 $\times$ 512 horizontal grid points. Both transition methods are conducted in two steps, each separated by one hour of physical time to limit numerical instabilities. This 24-h simulation is initialized with observations from the BLLAST field campaign.

The BLLAST field campaign took place from 14 June to 8 July 2011 in southern France at Lannemezan, an area of complex terrain a few kilometres from the Pyrenean foothills. Measurements from towers, radiosondes, airplanes, and ground-based remote sensing are taken during the whole campaign, with twelve intensive observing periods, characterised by various meteorological conditions. A detailed description can be found in Lothon et al. (2014). The 1st of July 2011 was chosen for the simulation of the complete diurnal cycle, because this day was characterised by anticyclonic conditions minimising large-scale forcings except subsidence and radiative cooling. The lower troposphere was governed by a mountain-plain circulation along the valley with almost no clouds prevalent.

The BLLAST ABL simulation is initialized with the potential temperature and the zonal and meridional wind data from the 0000 UTC radiosonde launch of the 1st of July. The domain height extends up to 3 km with a vertical resolution of 5 m in the first 200 m, increased to 10 m up to 800 m and 20 m to the domain top. The flux measurements are taken from a 60 m tower with values at 30 m, 45 m, and 60 m altitude. The sensible heat flux (SHF) at the surface is calculated via an e-folding scale of 300 m and the measurements at the heights z according to $\mathrm{SHF}_{z=0} = \mathrm{SHF}_z \exp(-z\,/\,300\ \mathrm{m})$. The temporal evolution of the measurements is set symmetric around 12 h with a maximum of roughly 140 W m^{-2} at noon and a minimum of -10 W m^{-2} at night (Fig. 2.4*a*). The simulation is dry and does not consider any moisture effects or latent heat fluxes. Subsidence and radiative cooling were applied as large-scale forcings. The subsidence velocity is calculated from the ABL height of the potential temperature profiles from the four radiosonde ascents at 0000 UTC, 1100 UTC, 1658 UTC, and 2254 UTC (Fig. 2.6) to a value of $w_{sub} = -10$ mm s^{-1}. A radiative cooling of the atmosphere of -2 K d^{-1} arises from the difference of the simulated potential temperature profile in a different simulation with exactly the same setup as the BLLAST ABL simulation, however, without radiative cooling. The values of the subsidence velocity and the radiative cooling are comparable to values of Bellon and Stevens (2012b).

2.4.3 Interface between atmospheric boundary-layer and wind-turbine simulations

Wind-turbine simulations performed to investigate the impact of neutral boundary-layer turbulence on wind-turbine wakes in Chapter 3 and for the numerically efficient param-

eterization of turbulent wind-turbine flows for LES of different thermal stratifications in Chapter 5 are performed on 512 × 64 × 64 grid points with open streamwise and spanwise boundary conditions. Wind-turbine simulation performed to investigate the impact of the diurnal cycle of the atmospheric boundary layer on wind-turbine wakes in Chapter 4 are performed on 512 × 512 × 64 grid points with open streamwise and periodic spanwise boundary conditions.

All wind-turbine simulations are performed with a horizontal resolution of 5 m and a vertical resolution of 5 m in the lowest 200 m and 10 m above. The rotor of the wind turbine is located at 300 m in the x-direction and centred in the y-direction with a diameter D and a hub height z_h of 100 m. In the heterogeneous wind-turbine simulations, it corresponds to a wind turbine located 300 m away from the obstacles in the precursor simulation. Further, all wind-turbine simulations in Chapters 7 and 8 are implemented with parameterization of type B.

For the wind-turbine simulations performed in Chapter 3, a logarithmic wind profile $u_{i_1,j,k} = \frac{u_*}{\kappa} \ln(\frac{z}{z_0})$ is prescribed with a friction velocity $u_* = 0.45$ m s^{-1}, a roughness length $z_0 = 0.1$ m, and the von Karman constant $\kappa = 0.4$. It is applied in combination with the wind-turbine parameterizations and the turbulence preserving method described in Chapter 2.

For the synchronized coupling between ABL and wind-turbine simulations in Chapter 4, the initial fields $\psi = (u, v, w, \Theta')$ at 12 h, 18 h, 24 h, 29 h, 36 h, 42 h, 48 h, and 53 h for the homogeneous wind-turbine simulations and at $t = 12$ h and 24 h for the heterogeneous wind-turbine simulations, as well as the 2 D inflow fields of ψ at each time step of the following one hour of the wind-turbine simulations ($\psi_{j,k}(t)$) are provided by the corresponding idealized ABL simulation. Further, the horizontal averages of the respective initial conditions of ψ are taken as background fields $\psi_e(\mathrm{z}) = (u_e(\mathrm{z}), v_e(\mathrm{z}), w_e(\mathrm{z}), \Theta_e(\mathrm{z}))$. At each time step of the wind-turbine simulation, the two dimensional y-z slice $\psi_{j,k}(t)$ contributes to the upstream values of ψ at $i = 1$, the left-most edge of the numerical domain at $x = 0$ m. This approach to handling the interface between the ABL and wind-turbine simulations is similar to techniques used by Kataoka and Mizuno (2002), Naughton et al. (2011), Witha et al. (2014), and Dörenkämper et al. (2015).

Wind-turbine simulations, using the idealized ABL simulation over homogeneous surface as precursor simulation, are performed in Chapter 4 for four regimes at two days, hereafter referred to as CBL (12 h - 13 h), EBL (18 h - 19 h), SBL (24 h - 25 h), and MBL (29 h - 30 h) representing day 1 and CBL_2 (36 h - 37 h), EBL_2 (42 h - 43 h), SBL_2 (48 h - 49 h), and MBL_2 (53 h - 54 h) representing day 2. Wind-turbine simulations, using the idealized ABL simulation over heterogeneous surface as precursor simulation, are performed for two regimes, hereafter referred to as CBL_{het} (12 h - 13 h) and SBL_{het} (24 h - 25 h).

For the wind-turbine simulations performed in Chapter 5, the detailed simulation setup, resulting from the parameterization, is deduced in detail in Chapter 5.

2.4.4 Atmospheric boundary-layer and wind-turbine characteristics

This work investigates the following characteristics of the ABL and the wind-turbine wakes:

- The budget of the resolved mean TKE of the ABL

$$\overline{e} = \frac{1}{2}\left(\overline{u''^2} + \overline{v''^2} + \overline{w''^2}\right) \tag{2.20}$$

is calculated at each height level according to Stull (1988)

$$\underbrace{\frac{\partial \overline{e}}{\partial t}}_{Storage\ St} = \underbrace{-\left(\overline{u''w''}\frac{\partial \overline{u}}{\partial z} + \overline{v''w''}\frac{\partial \overline{v}}{\partial z}\right)}_{Shear\ S} + \underbrace{\frac{g}{\Theta_0}\overline{w''\Theta''}}_{Buoyancy\ Production\ B} - \underbrace{\frac{\partial \overline{w''e''}}{\partial z}}_{Turbulent\ Transport\ T} - \underbrace{\epsilon}_{Dissipation\ D}. \tag{2.21}$$

In this representation, u'', v'', w'', Θ'', p'', and e'' are the turbulent fluctuations of the velocity components u, v, w, the potential temperature Θ, the pressure p and the resolved turbulent kinetic energy e. Θ_0 is the reference potential temperature at the ground. ϵ represents the dissipation rate and is calculated as the residual from all other contributions. The overlines in Eq. (2.20) indicate a temporal (1 h) and an area (horizontal domain size) average. Here, $\xi'' = \xi - <\xi(z)>_{x,y}$, whereas $\xi' = \xi - \xi_e$. For all variables except for $\xi = \Theta$, $\xi'' = \xi'$.

- The spatial distribution of the temporal average of the streamwise velocity $\overline{u_{i,j,k}}$, the streamwise velocity ratio

$$VR_{i,j,k} = \frac{\overline{u_{i,j,k}}}{\overline{u_{i_1,j,k}}}, \tag{2.22}$$

and the streamwise velocity deficit

$$VD_{i,j,k} = \frac{\overline{u_{i_1,j,k}} - \overline{u_{i,j,k}}}{\overline{u_{i_1,j,k}}}, \tag{2.23}$$

as they are related to the power loss of a wind turbine.

- The streamwise turbulent intensity

$$I_{x_{i,j,k}} = \frac{\sigma_{u_{i,j,k}}}{\overline{u_{i,j,k_h}}} \tag{2.24}$$

  and the total turbulent intensity

$$I_{i,j,k} = \frac{\frac{1}{3}\sqrt{\sigma^2_{u_{i,j,k}} + \sigma^2_{v_{i,j,k}} + \sigma^2_{w_{i,j,k}}}}{\overline{u_{i,j,k_h}}}, \tag{2.25}$$

  with $\sigma_{u_{i,j,k}} = \sqrt{\overline{u'^2_{i,j,k}}}$, $\sigma_{v_{i,j,k}} = \sqrt{\overline{v'^2_{i,j,k}}}$, and $\sigma_{w_{i,j,k}} = \sqrt{\overline{w'^2_{i,j,k}}}$, as well as $u'_{i,j,k} = u_{i,j,k} - \overline{u_{i,j,k}}$, $v'_{i,j,k} = v_{i,j,k} - \overline{v_{i,j,k}}$, and $w'_{i,j,k} = w_{i,j,k} - \overline{w_{i,j,k}}$, as it affects the flow-induced dynamic loads on downwind turbines.

In the x-z plane, the index j_0 corresponds to the centre of the domain in y-direction y_0, whereas in the x-y plane, the index k_h corresponds to the hub height z_h.

The wind-turbine simulations are performed for 20 min in Chapter 3 and for 60 min in Chapters 4 and 5. In each simulation, the time period is long enough for the wake to reach an equilibrium state with statistical convergence of the results. All mean values are averaged over the last 10 min in Chapter 3 and 50 min in Chapters 4 and 5. The temporal average $\overline{\Psi_{i,j,k}}$ of a quantity Ψ for a time period t is calculated online in the numerical model and updated at every time step according to the method of Fröhlich (2006, Eq. 9.1).

Generally, the numerical simulation results are plotted in dimensionless coordinates as a function of the rotor diameter D. The contour of the actuator in the cross-sections represents the transition to a wind-turbine force of zero. Furthermore, only a sector of the complete computational domain is shown in most of the following plots.

2.4.5 Validation of the atmospheric boundary-layer simulations of the diurnal cycle

A complete diurnal cycle of one day is simulated with the LES model EULAG by using observations from the BLLAST field campaign for initialization and validation. The BLLAST diurnal cycle simulation is performed to give confidence in the ability of the geophysical flow solver EULAG to simulate the diurnal cycle of an idealized ABL simulation. For the evaluation of the BLLAST ABL simulation, the sensible heat flux, the potential temperature, and the TKE budget are shown in Fig. 2.4. The structure of the potential temperature and the TKE budget are strongly influenced by the diurnal cycle enforced by the prescribed sensible heat flux. For rather low surface flux values in $t \in [0\ h, 5\ h]$, the ABL in Fig. 2.4*b* consists of an SBL capped by a neutrally-stratified layer, the residual

layer. An increase of the surface fluxes at t = 5 h from their minimum level initiates the onset of the MBL, which is related to a warming of the surface in Fig. 2.4*b*. This generates thermals and the turbulent eddies increase in size and strength and start to form a fully convective layer, which continues to grow throughout the morning eroding the stable layer from below and incorporating the residual layer in a process called free encroachment (Sorbjan, 2004) (Fig. 2.4*b*). This results in a fully developed CBL, characterised by the domination of buoyancy over shear in Figs. 2.4*c* and 2.5*a* (Stull, 1988; Beare, 2008). The decrease of the surface fluxes approaching their minimum level represents the EBL. In the EBL, the decaying CBL merges into the SBL, which is shear driven, because the eddies have less energy in comparison to the CBL due to much smaller surface flux values (Stull, 1988; Beare, 2008). The domination of shear over buoyancy is not visible in Fig. 2.4*c* because the individual TKE budget terms are approximately an order of magnitude smaller at night in comparison to the daytime situation. A comparison of the vertical evolution of the horizontal average of the TKE budget in Fig. 2.5*b*, however, confirms this statement. Further, the height of the ABL during the diurnal cycle simulation corresponds to the stronger stratification in Fig. 2.4*b*, which is limited by the imposed large-scale subsidence.

This diurnal cycle dependency, existing in the potential temperature as well as in the TKE budget, is in qualitative agreement with other studies like Stull (1988), Kumar et al. (2006), and Basu et al. (2008). The amount and temporal evolution of the TKE budget during the day are in agreement with the results from Blay-Carreras et al. (2014), who performed an LES with the DALES model for the 1st of July of the BLLAST campaign. Their simulation lasted 12.5 h starting at 0730 UTC, which does not allow a comparison of this SBL state.

A quantitative comparison of the horizontally-averaged Θ profiles with the radiosonde measurements from the BLLAST campaign is shown in Fig. 2.6. The simulation is initialized with a fit to the observed 0000 UTC potential temperature profile. The potential temperature structure evolves towards a convective profile in the first eleven hours (Stull, 1988; Kumar et al., 2006; Basu et al., 2008; Beare, 2008; Walter et al., 2009; Rhodes and Lundquist, 2013). The decrease of the ABL height is induced by the imposed large-scale subsidence. After 17 h, the simulated Θ profile fits well with the observation for $z < 1300$ m. Above the inversion, modelled and observed profiles differ, as other mesoscale influences are not taken into account in the LES. After 23 h, a stable stratification has established again (Stull, 1988; Kumar et al., 2006; Basu et al., 2008; Beare, 2008; Walter et al., 2009; Rhodes and Lundquist, 2013). Considering 23 h of simulation with the limited prescribed external forcings, the colder temperature in the lowest levels can be caused by additional large-scale effects, which are not included in this simulation, e.g. colder air close to the surface advecting from the mountains as part of the mountain-plain circulation.
A quantitative comparison of the evolution of the wind is not reasonable for this simulation. This is for two reasons: Firstly, only the initialization contains an information of the wind conditions, no additional information of measured profiles during the diurnal cycle is given during the simulation. Secondly, no mesoscale processes are included in the simulation.

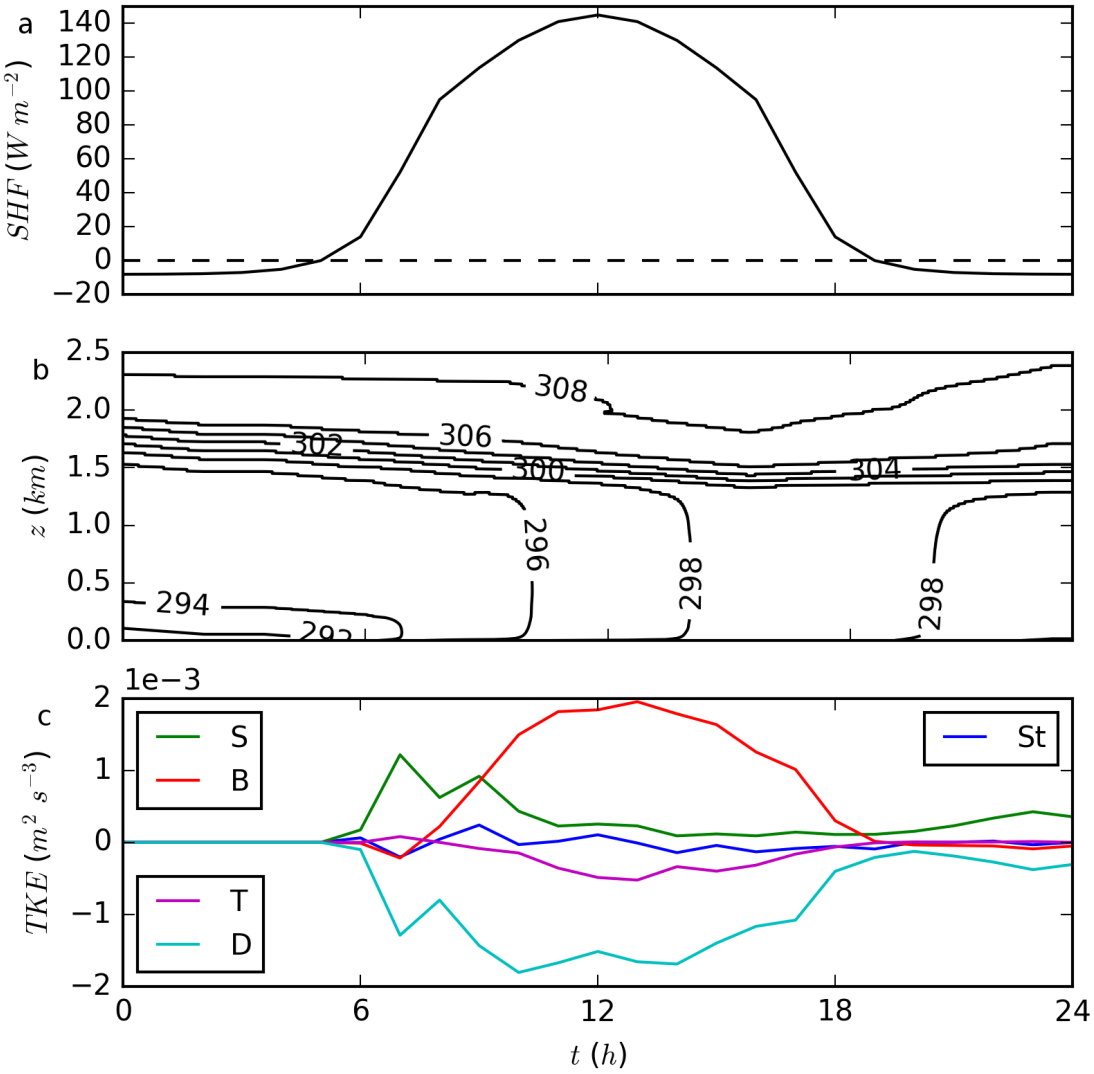

Figure 2.4: Temporal evolution of the sensible heat flux in W m^{-2} in *a*, time and space variation of the horizontal average of the potential temperature in K in *b* and of the TKE budget in m^2 s^{-3} in *c*. The individual TKE budget terms from Eq. (2.21) are integrated over the height of the ABL, defined as the altitude at which the vertical gradient of the potential temperature reaches its maximum (Sullivan et al., 1998).

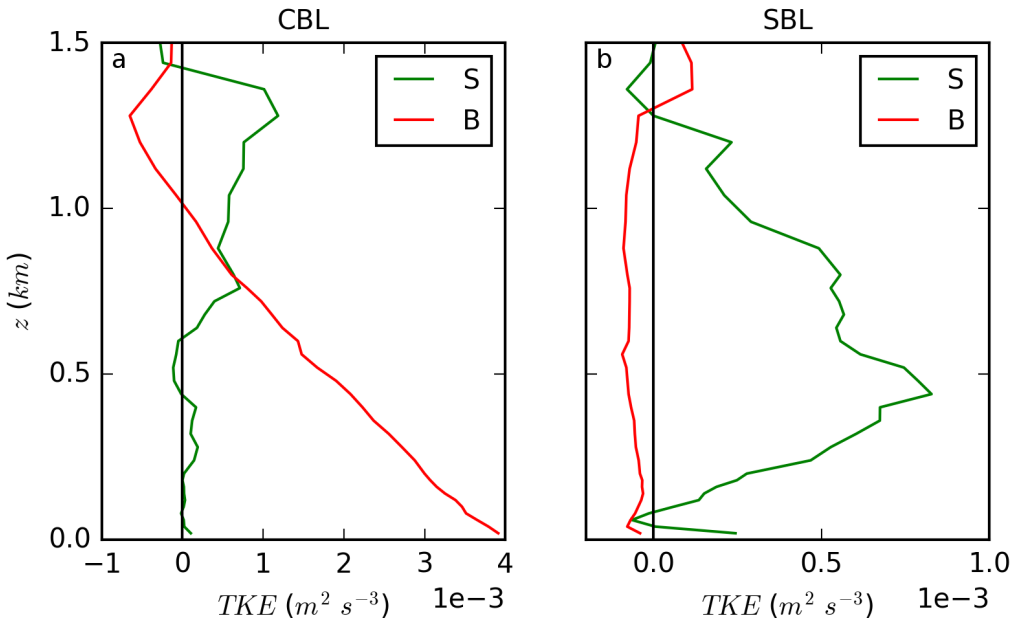

Figure 2.5: Vertical evolution of shear and buoyancy as defined in the TKE budget in Eq. (2.21) after 12 h in *a* and after 24 h in *b* (note the different scale on the x-axis).

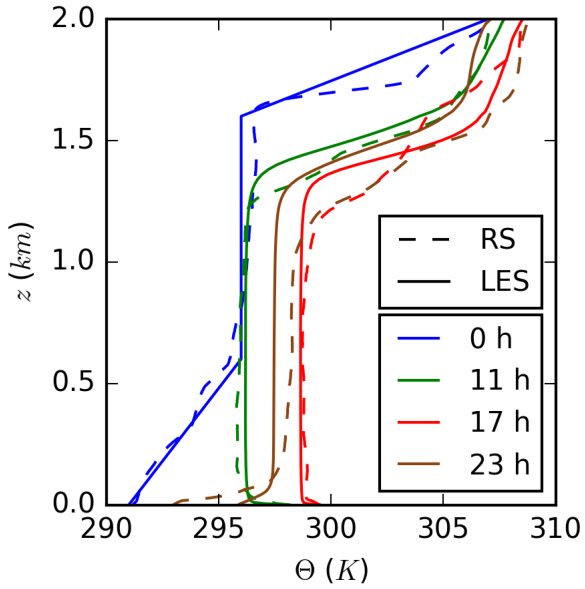

Figure 2.6: The temporal evolution of the horizontal average of $\Theta(z)$ (solid lines) and the corresponding radiosonde measurements (dashed lines) at 0 h, 11 h, 17 h, and 23 h for the lowest 2 km.

They, however, could be important, even for a surface driven weather situation with minimum larger scale disturbances. This point is considered and the simulation strategy is intended, because a more quantitative comparison is not required for the purpose of the BLLAST simulation.

The qualitative comparison of the temporal evolution of the potential temperature and the analysis of the TKE budget together with the quantitative comparison of the LES results with the potential temperature profiles of radiosonde measurements at 1100 UTC, 1700 UTC, and 2300 UTC give confidence in the ability of the numerical model EULAG to simulate the diurnal cycle of the idealized ABL simulation in the following.

3 Impact of neutral boundary layer turbulence on wind-turbine wakes

In this chapter, the impact of NBL turbulence on wind-turbine wakes is investigated by applying the turbulence preserving method and the wind-turbine parameterizations A, B, and C from Chapter 2. A detailed investigation of the reference simulation B_1 (base case) with $\alpha = 1$ (Eq. 2.18) and wind-turbine parameterization B is given to confirm the application of the turbulence preserving model in a wind-turbine simulation. Further, the dependence of the wake characteristics of the reference simulation B_1 are investigated regarding the impact of,

- a, the perturbation amplitude
- b, the wind-turbine parameterization
- c, the rotation of the disc
- d, the SGS closure model.

The corresponding parameters of B_1 and of all other simulations are listed in Table 3.1.

As explained in the Introduction, this investigation is the groundwork to understand the operation of a wind turbine under different atmospheric conditions.

3.1 Reference simulation B_1

Figure 3.1 shows the vertical (in a) and horizontal (in b) cross-sections of the streamwise wind field of wind-turbine simulation B_1. The general wake structure reveals a minimum of the velocity right behind the rotor with a velocity increase in the radial and streamwise directions. This pattern results from the entrainment of surrounding air with higher velocity values and is observed prevalently in field experiments in the atmosphere (Heimann et al., 2011, Fig. 3) or in wind-tunnel measurements (Zhang et al., 2012, Fig. 4), as well as simulated numerically (Porté-Agel et al., 2010, Fig. 5; Wu and Porté-Agel, 2012, Fig. 3; Aitken et al., 2014, Fig. 5; Mirocha et al., 2014, Fig. 5).

The x-y cross-section of u shows a nearly axisymmetric distribution (Fig. 3.1b), whereas the x-z cross-section of u displays a non-axisymmetric mean velocity profile (Fig. 3.1a), as a consequence of the vertically sheared upstream wind profile and the effect of the surface.

Table 3.1: List of all performed simulations in this chapter with information of the perturbation amplitude, the type of the wind-turbine parameterization, the tangential force, and the SGS closure model used in the LES model.

simulation	perturbation amplitude α	wind-turbine parameterization	tangential force F_Θ	SGS closure model
B_1	1	B	$\neq 0$	TKE
B_5	5	B	$\neq 0$	TKE
B_10	10	B	$\neq 0$	TKE
A_1	1	A	$\neq 0$	TKE
C_1	1	C	$\neq 0$	TKE
A_NR	1	A	$= 0$	TKE
B_S	1	B	$\neq 0$	Smagorinsky
B_I	1	B	$\neq 0$	no (implicit LES)

Another feature in the x-z cross-section (Fig. 3.1a) represents the region of higher velocity air at the lowest part of the rotor in comparison to the surroundings. The velocity deficit plotted as contour lines in Fig. 3.1 enables a comparison with lidar measurements (Iungo et al., 2013; Käsler et al., 2010) or with remotely piloted aircraft measurements (Wildmann et al., 2014). These measurements for similar sized turbines and wind speeds result in a wind speed deficit of about 50 to 60 % at $x = 4D$, which is in line with the contours of the reference simulation in Fig. 3.1. In Fig. 3.2, the mean values of u, v, and w are plotted in a y-z cross-sections for selected downstream positions at $x = 3D$, $x = 5D$, and $x = 10D$. With increasing streamwise distance from the rotor, the flow field u recovers and starts to converge towards the upstream wind profile. The general structure of the position of the velocity minimum as well as the recovery of the wind field is comparable to published results (e.g., Wu and Porté-Agel, 2012, Fig. 4; Mirocha et al., 2014, Fig. 4). Depending on the implementation of a nacelle, the flow field directly behind the centre of the wind turbine changes. Among others, Wu and Porté-Agel (2011) and Meyers and Meneveau (2013) include the nacelle, whereas it is neglected in Aitken et al. (2014) and Mirocha et al. (2014). The slices of the lateral wind component v reveal a maximum at the upper rotor part and a minimum at the lower part, which corresponds to the vertical velocity field w with a maximum for $y/D \in [-1, 0]$ and a minimum for $y/D \in [0, 1]$. The intensity of this rotational effect decreases with increasing streamwise distance from the rotor. The regions with the maximum swirl of the flow are veering away from the rotor centre for an increasing downstream distance. The pattern in v and w is comparable to Mirocha et al. (2014, Fig. 4). In contrast to these results, the y-z cross-sections in Mirocha et al. (2014) are asymmetric, which is most likely induced by the weakly convective ABL in their simulations.

In Fig. 3.3, the temporally averaged velocity component in streamwise direction $\overline{u_{i,j,k}}$ is plotted as a function of streamwise distance for different positions (top, bottom, right ($y/D \in [0, 1]$), left ($y/D \in [-1, 0]$)) 60 m away from the centre of the rotor. These positions,

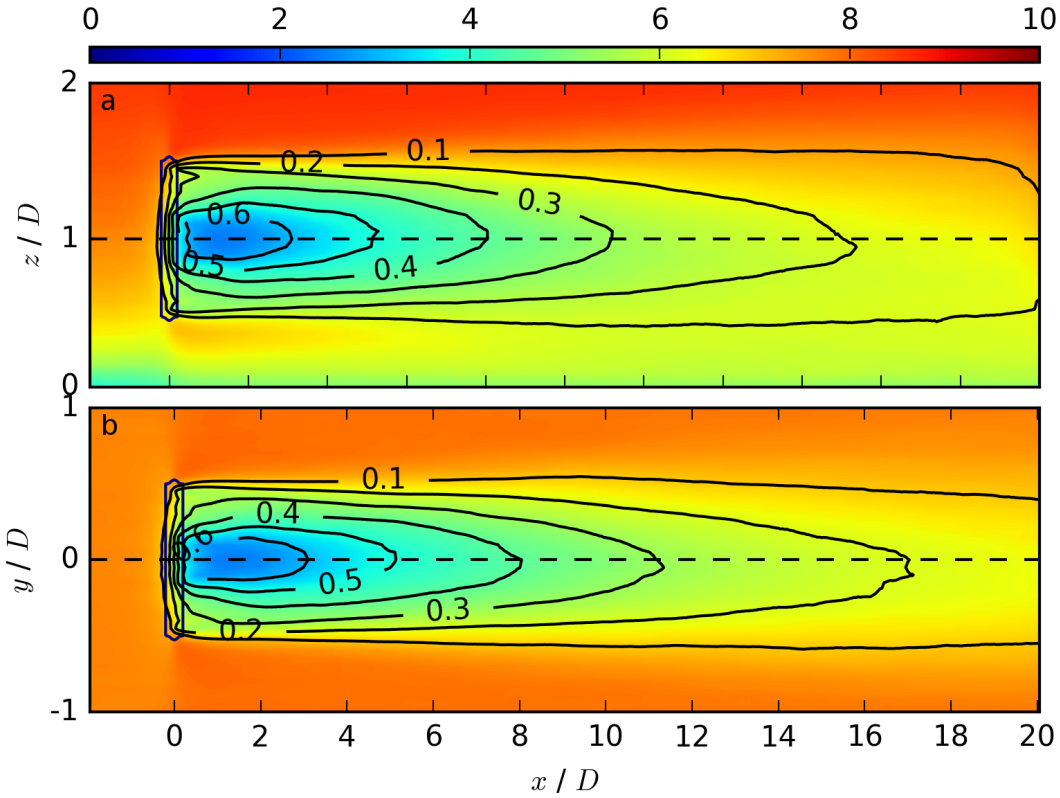

Figure 3.1: Streamwise wind field in a vertical x-z cross-section at j_0 in a and in a horizontal x-y cross-section at k_h in b. The contours represent the velocity deficit $(u_{i_1,j_0,k} - u_{i,j_0,k})/u_{i_1,j_0,k}$ in a and $(u_{i_1,j,k_h} - u_{i,j,k_h})/u_{i_1,j,k_h}$ in b. Note, that in these cross-sections, the scale in the z or y-direction is exaggerated compared to the horizontal scale the in x-direction.

although located outside of the actuator ($R = 50\,\mathrm{m}$), are still close enough to represent the effect of the forces resulting from Eq. 2.10 on the flow field. In the upstream region, the velocities at the top and the bottom locations differ due to the incoming logarithmic wind profile whereas the wind speeds right and left of the rotor are the same. Approaching the rotor, the flow is decelerated in front of the wind turbine and accelerated behind it. This behaviour is induced by the flow deceleration due to the axial force F_x, which causes a pressure increase in front of the rotor and a decrease behind (Bernoulli equation) (Hansen, 2008) .

The difference of the flow in the spanwise direction for $x/D > 2$ results from the rotation of the actuator, leading to an accelerated (decelerated) flow on the right (left) due to downward (upward) transport of air with higher (lower) momentum. The flow recovers with increasing distance and the velocity values start approaching the values of the incoming wind field for $x \geq 10D$. The effect of the wind turbine on the wake is not negligible even at a streamwise distance of $x = 20D$ in Fig. 3.1, therefore a full recovery in Fig. 3.3 at positions $x > 20D$ is expected.

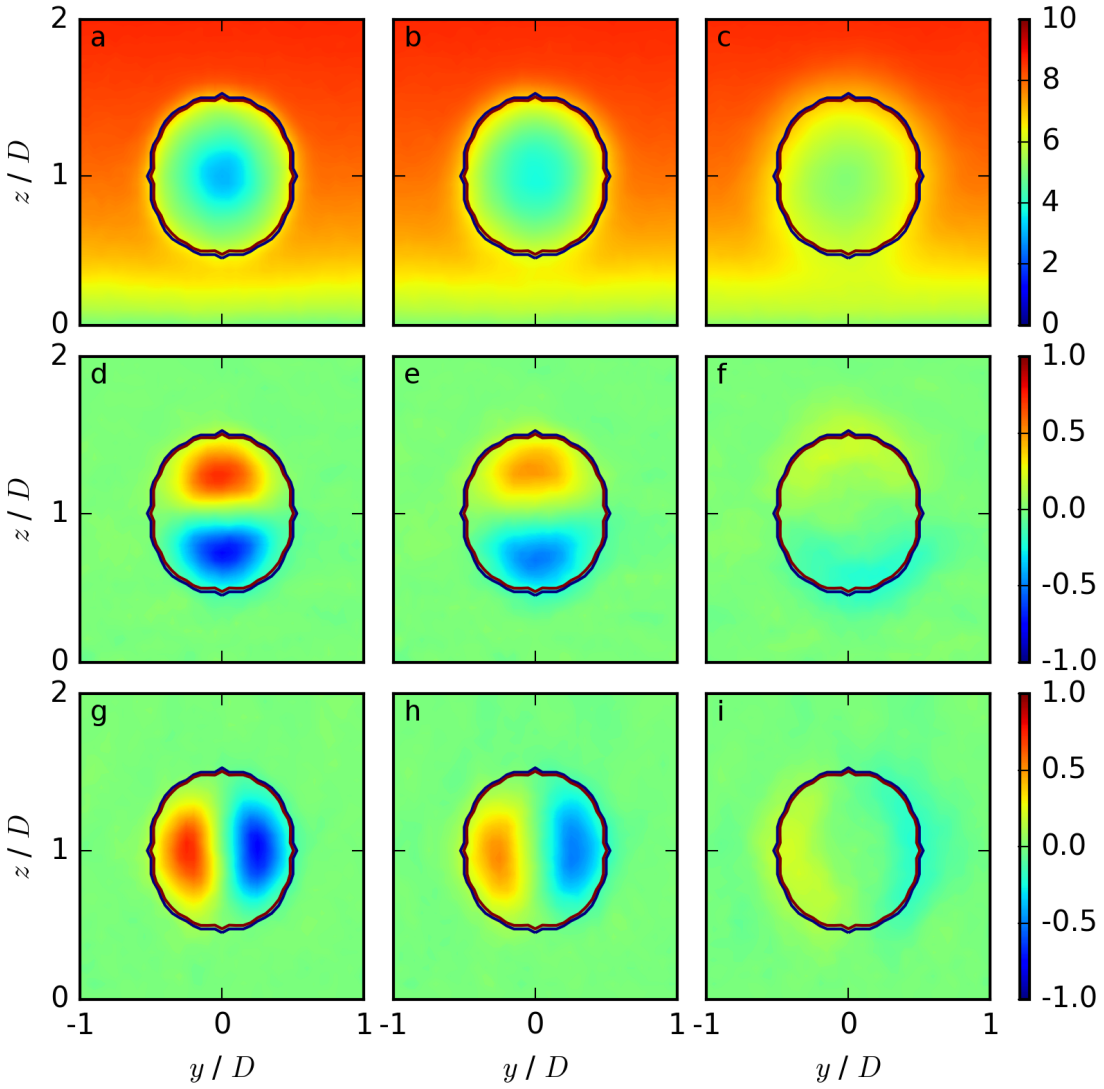

Figure 3.2: The averaged values of the base-case simulation (B_1) of $\overline{u_{i,j,k}}$ in *a*-*c*, $\overline{v_{i,j,k}}$ in *d*-*f* and $\overline{w_{i,j,k}}$ in *g*-*i*) in *y*-*z* cross-sections at downstream positions $x = 3D$ (*a*, *d*, *g*), $x = 5D$ (*b*, *e*, *h*) and $x = 10D$ (*c*, *f*, *i*).

3.2 Impact of the perturbation amplitude

The method of preserving the background turbulence includes the factor α in Eq. 2.18, which was introduced as the amplitude of the perturbation. The impact of α is studied in simulations B_5 ($\alpha = 5$) and B_10 ($\alpha = 10$) and compared to the reference simulation B_1 ($\alpha = 1$).

Figure 3.4*a* shows the streamwise profiles of the velocity ratio from Eq. 2.22 for different values of the perturbation amplitude α. A larger α value leads to a progressively shorter

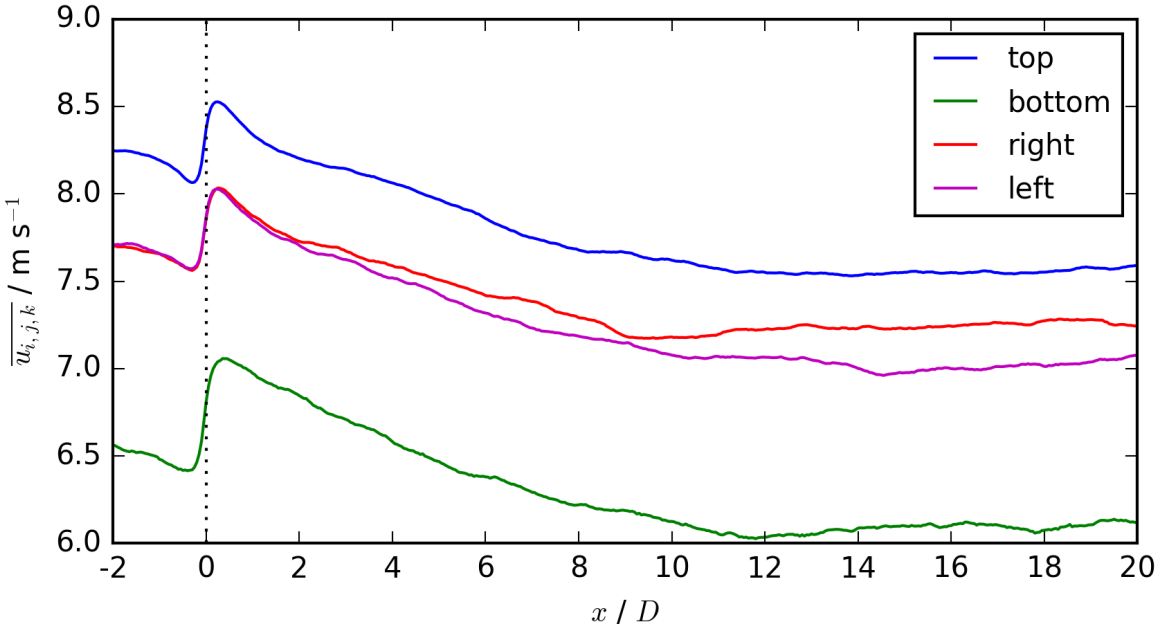

Figure 3.3: The streamwise velocity component $\overline{u_{i,j,k}}$ of the base-case simulation B_1 at four positions, which are located 60 m away from the rotor centre ($R = 50$ m), in both spanwise (left and right) and vertical (top and bottom) directions. The spanwise directions correspond to Figs. 3.1 and 3.2 with right $\equiv y/D \in [0, 1]$ and left $\equiv y/D \in [-1, 0]$.

streamwise extension of the wake, induced by a stronger entrainment of ambient air. Further, the minimum of the velocity ratio in the near wake directly behind the nacelle increases.

The markers in Fig. 3.4*a* correspond to different wind-turbine studies, as described in detail in Table 3.1. The simulation results of B_1 are comparable to lidar measurements and WRF-LES model results for a stable ABL (Aitken et al., 2014). By increasing the value of α, the velocity ratio approaches values found in observations and simulations of cases with enhanced turbulence. The numerical results of simulation B_5 correspond to a neutral ABL (Wu and Porté-Agel, 2011; Gomes et al., 2014), whereas the results of simulation B_10 are almost comparable to measurements and WRF-LES model results in a convective ABL (Mirocha et al., 2014). This comparison with other studies leads to the hypothesis that the factor α from Eq. 2.18 could be related quantitatively to different levels of atmospheric turbulence.

Further, various precursor simulations were tested (convection or Coriolis force as trigger to excite turbulence), resulting in different spectral energy densities. The velocity ratio for a larger amount of the spectral energy density is in agreement with a larger value of α (not shown here). The parameter α is also comparable to the different roughness lengths used in Wu and Porté-Agel (2012), with a larger roughness length corresponding to a higher perturbation amplitude.

Table 3.2: List of all used markers for the velocity ratio and the turbulent intensity of a wind turbine, resulting from various studies.

Symbol	Origin	Reference
+	NBL LES	Wu and Porté-Agel (2011, Fig. 4)
+	NBL LES	Wu and Porté-Agel (2011, Fig. 4)
×	RANS	Gomes et al. (2014, Fig. 1)
●	SBL lidar measurements	Aitken et al. (2014, Fig. 6)
⋆	SBL WRF-LES	Aitken et al. (2014, Fig. 6)
▲	CBL measurements	Mirocha et al. (2014, Fig. 8)
▲	CBL WRF-LES (SHF = 20 W m^{-2})	Mirocha et al. (2014, Fig. 8)
▲	CBL WRF-LES (SHF = 100 W m^{-2})	Mirocha et al. (2014, Fig. 8)
■	NBL LES $z_0 = 1 \times 10^{-5}$ m	Wu and Porté-Agel (2012, Fig. 5)
■	NBL LES $z_0 = 1 \times 10^{-1}$ m	Wu and Porté-Agel (2012, Fig. 5)

The streamwise profiles of the turbulent intensity in Eq. 2.25 are presented in Fig. 3.5*a* for different α values. The turbulent intensity $I_{x_{i,j_0,k_h}}$ increases with increasing α. In the upstream as well as in the downstream region, the streamwise distribution of $I_{x_{i,j_0,k_h}}$ is proportional to α. Wu and Porté-Agel (2012) investigate an increase of $\mathrm{I}_{x_{i,j_0,k_h}}$ for increasing z_0. This study also results in an increase of $\mathrm{I}_{x_{i,j_0,k_h}}$ for increasing α, reinforcing the assumption that larger α values are comparable to a surface with an increased roughness length.

The investigations lead to the conclusion that the entrainment in the wake can be easily modified by adjusting the value of α in the numerical simulations. In this way, a realistic level of atmospheric background turbulence intensity corresponding to various atmospheric stratifications or different roughness lengths can be parameterized by applying the turbulence preserving model.

3.3 Impact of the wind-turbine parameterization

The impact of the three wind-turbine parameterizations A, B, and C on the wake is studied for $\alpha = 1$ (Eq. 2.18) in simulations A_1, B_1 and C_1. The different parameterizations influence the velocity ratio in the wake as documented in Fig. 3.4*b*.

A comparison between simulation A_1 and simulation B_1 focuses on the difference between the MMT and the BEM method. Approaching a downstream distance of $x = 5D$, the difference in the wake structure becomes marginal. Therefore, a streamwise distance of $x = 5D$ is defined as the transition between the near wake and the far wake. Further, the value of the minimum of the velocity ratio in the near wake is larger for parameterization A in A_1 due to no radial dependence of the thrust and power coefficients in Eqs. 2.8 and 2.9.

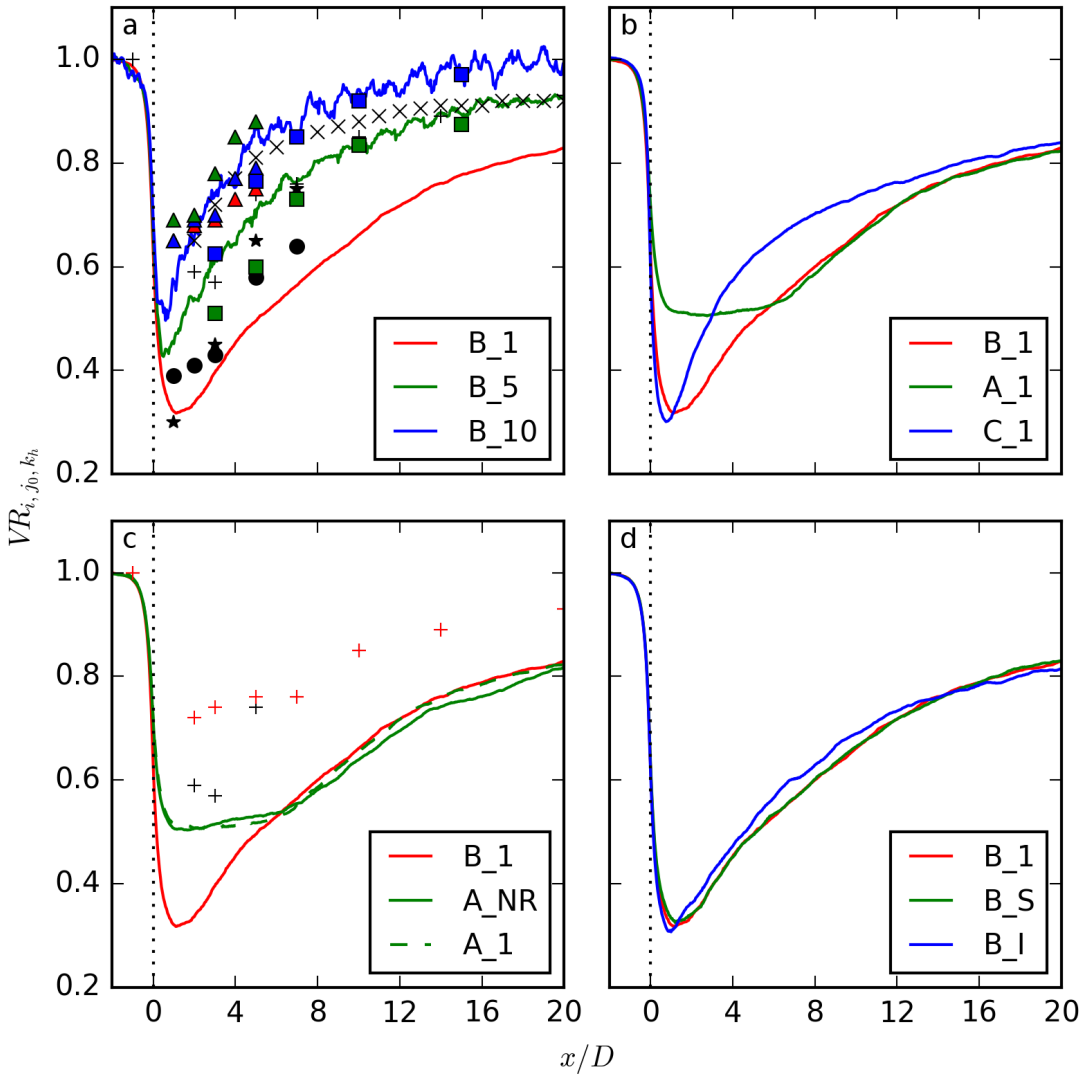

Figure 3.4: Dependency of the streamwise velocity ratio from Eq. 2.22 at j_0 and k_h for all simulations listed in Table 3.1, grouped together regarding the wake impact of the perturbation amplitude in *a*, the wind-turbine parameterization in *b*, the rotation of the disc in *c*, and the SGS closure model in *d*. All used markers are listed in Table 3.2.

The difference between wind-turbine parameterizations B and C are the local blade characteristics of the two airfoils. In wind-turbine parameterization C the velocity field in the streamwise direction recovers more rapidly up to approximately $x = 14D$ in comparison to type B. This is caused by the sharper gradient in the axial force at the edge of the nacelle between 0.2 r/R and 0.3 r/R in Fig. 2.3.

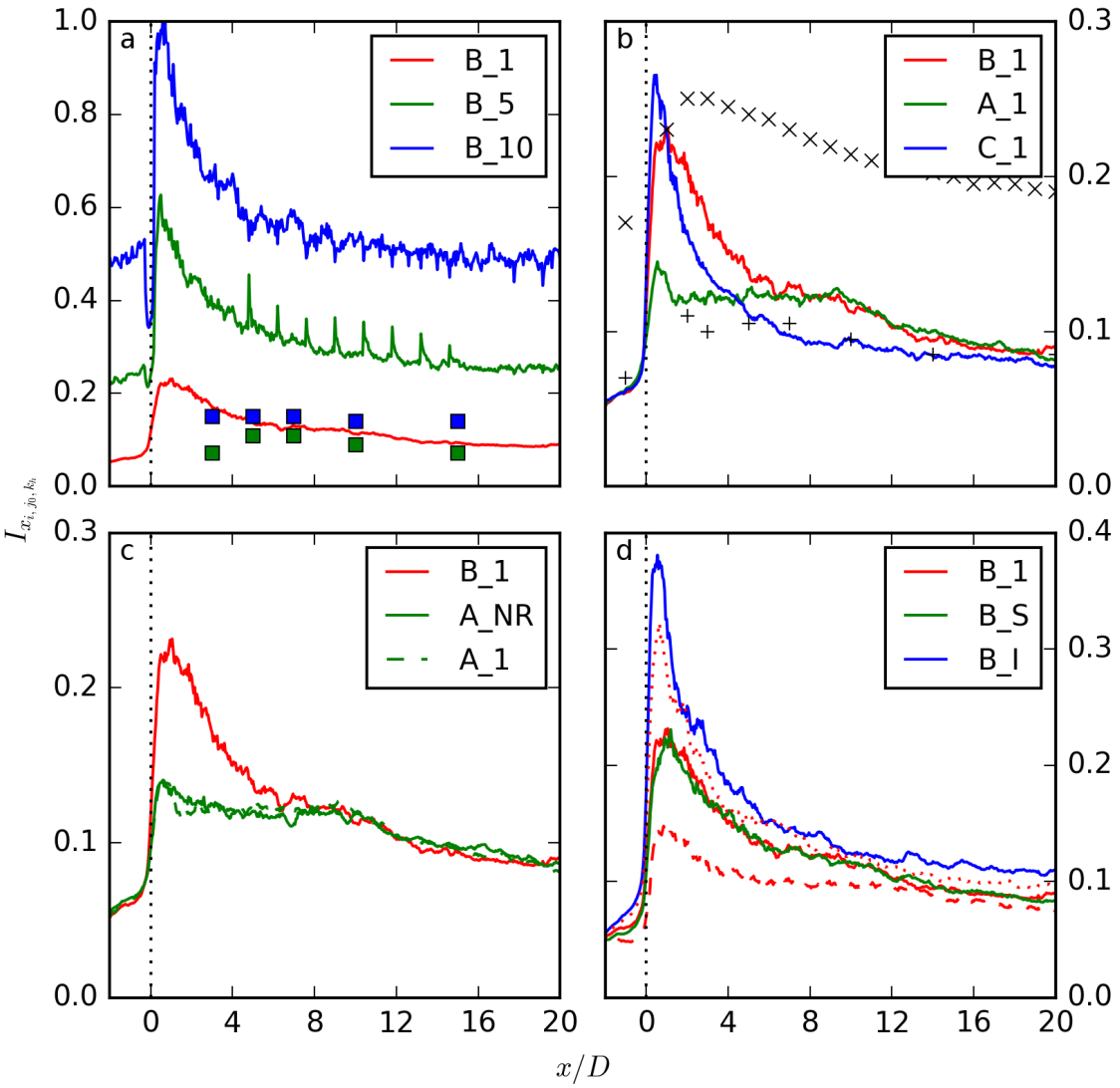

Figure 3.5: Dependence of the streamwise turbulence intensity from Eq. 2.24 at j_0 and k_h for all simulations listed in Table 3.1, grouped together regarding the wake impact of the perturbation amplitude in *a*, the wind-turbine parameterization in *b*, the rotation of the disc in *c*, and the SGS closure model in *d*. All used markers are listed in Table 3.2. The dotted line in plot *d* represents simulation B_1 with 1/2 times the length scale in the SGS closure model, whereas the dashed line represents simulation B_1 with twice the length scale in the SGS closure model.

The different wind-turbine parameterizations also have an impact on the value of the maximum of the streamwise turbulent intensity in Fig. 3.5*b*. The maximum is larger for wind-turbine parameterization B in comparison to wind-turbine parameterization A. This is

caused by the radial gradient of the axial force in wind-turbine parameterization B, which contrasts a constant force in wind-turbine parameterization A, as shown in Fig. 2.3. The streamwise turbulent intensities of wind-turbine parameterizations A and B are very similar in the far wake. The difference in the maximum between wind-turbine parameterizations B and C correlates with the gradient of the axial force close to the nacelle in Fig. 2.3. A larger maximum corresponds to a sharper gradient. A sharper gradient also results in a more rapid decline in wind-turbine parameterization C in comparison to wind-turbine parameterization B up to approximately $x = 14D$.

Comparing these results to other studies, the streamwise turbulent intensity values of all three wind-turbine parameterizations are rather small in comparison to the Reynolds-averaged Navier-Stokes (RANS) simulation of Gomes et al. (2014) approaching $x \geq 2D$. A comparison with the LES of Wu and Porté-Agel (2011) results in a rather good agreement in the near wake for wind-turbine parameterization A and in the far wake for wind-turbine parameterization C. The agreement of wind-turbine parameterization C is referable to a similar radial distribution of the forces yielded from the same blade characteristics. The near-wake difference can be related to the SGS closure model, as described in detail later.

Similar to the results from Ivanell et al. (2008), Porté-Agel et al. (2010), Wu and Porté-Agel (2011), and Tossas and Leonardi (2013), who compared the Rankine-Froude approach to the BEM approach, this analysis leads to the conclusion that the MMT, who in comparison to the Rankine-Froude approach also accounts for a tangential force, is sufficient as simplification of the BEM parameterization if only the far wake is of interest. In the near wake the radial dependence of the axial force becomes important. Further, the local blade characteristics influence the wake up to a downstream distance of $x = 14D$.

In the scope of this work, I also implemented an advanced version of the MMT. It considers the radial distribution of the forces in Eqs. 2.8 and 2.9, which is adopted from the radial chord length dispersion in Micallef et al. (2013). The forces in Eqs. 2.8 and 2.9 are modified similarly to the procedure in Gomes et al. (2014). Numerical simulations using this approach led to a better agreement of the near-wake structure with the BEM method in wind-turbine parameterization B in comparison to the MMT approach (not shown here).

3.4 Impact of the rotation of the disc

To investigate the impact of the rotation of the actuator on the wake structure, simulation A_NR with wind-turbine parameterization A, no rotation of the disc ($F_\Theta = 0$ in Eq. 2.9), and $\alpha = 1$ (Eq. 2.18) is performed and compared to simulations A_1 and B_1.

The minimum of the velocity ratio in simulation B_1 is smaller in comparison to simulation A_NR. This finding is in agreement with the results from Wu and Porté-Agel (2011) (markers in Fig. 3.4*c*). A comparison between simulation A_1 and simulation A_NR results in a marginal impact of the tangential force on the streamwise velocity ratio according to

Fig. 3.4*c*. Therefore, the difference between simulation B_1 and simulation A_NR is evoked by the uniform thrust force distribution over the disc, which has a larger impact on the velocity ratio than the marginal effect of rotation.

Wu and Porté-Agel (2011) show an increase of the turbulence intensity applying the BEM method instead of the classical Rankine-Froude approach. The streamwise turbulent intensity at the centre line in Fig. 3.5*c* is also larger for the BEM parameterization in the near wake. The effect of rotation is marginal. Consequently, not the swirl, but the non-uniform distribution of the axial force in the BEM method (Fig. 2.3) is responsible for the near-wake difference in the streamwise turbulent intensity in Fig. 3.5*c*.

The rotation of the disc in simulation A_1 leads to a swirl in the wake as shown in Figs. 3.6*a-c*. The rotational effect of the disc is evident at $x = 3D$. Approaching $x = 10D$, the swirl in the disc region decays while it is transported outwards. Both effects originate from entrainment processes. At a downstream position of $x = 20D$, the rotation in the disc region approaches zero, whereas there is still some swirl in the air around the disc. In contrast to this rotational behaviour, there is no swirl of the air downstream of the non-rotating disc of simulation A_NR in Figs. 3.6*d-f*. The pattern of the streamwise velocity u in the rotor region as well as in the surroundings is comparable in both simulations at $x = 3$D and 10D. At $x = 20$D, the wake pattern in simulation A_NR is symmetric, whereas in simulation A_1 it is shifted towards $y/D \in [-1, 0]$. This asymmetric streamwise velocity field results from the rotation of the disc and is also prevalent in the study of Wu and Porté-Agel (2012, Fig. 4). This investigation leads to the conclusion that the rotation has a minor effect on the velocity ratio and on the streamwise turbulent intensity at the centre line. However, the effect of the tangential force on the v and w wind components is prevailing even in the far-wake region, with an influence on the streamwise velocity field in the y-z plane.

3.5 Impact of the SGS closure model

The impact of the SGS closure models is investigated by comparing the TKE SGS closure model simulation B_1 with the Smagorinsky SGS closure model simulation B_S. The geophysical flow solver EULAG provides a reliable numerical testbed to study the SGS closure model sensitivities. Further, it depends on the non-oscillatory forward-in-time integrations of Eqs. 2.1 to 2.6 and therefore offers the possibility to integrate these equations without an explicit SGS closure model by setting $\boldsymbol{\mathcal{V}} = 0$ and $\mathcal{H} = 0$ in Eqs. 2.1 and 2.5 in the implicit LES B_I.

The streamwise dependency of the velocity ratios in Fig. 3.4*d* agrees quantitatively very well for simulation B_1 and simulation B_S. The contrast to simulation B_I is insignificant.

The streamwise turbulent intensities in Fig. 3.5*d* are also rather similar for the TKE and the Smagorinsky SGS closure model. For the implicit LES, the maximum of $I_{x_{i,j_0,k_h}}$ is roughly 1.7 times larger than in the simulations with the SGS closure model. In the far wake the difference becomes rather small. The dependency of the difference in the streamwise turbulent intensity in the near wake between an implicit LES and a simulation

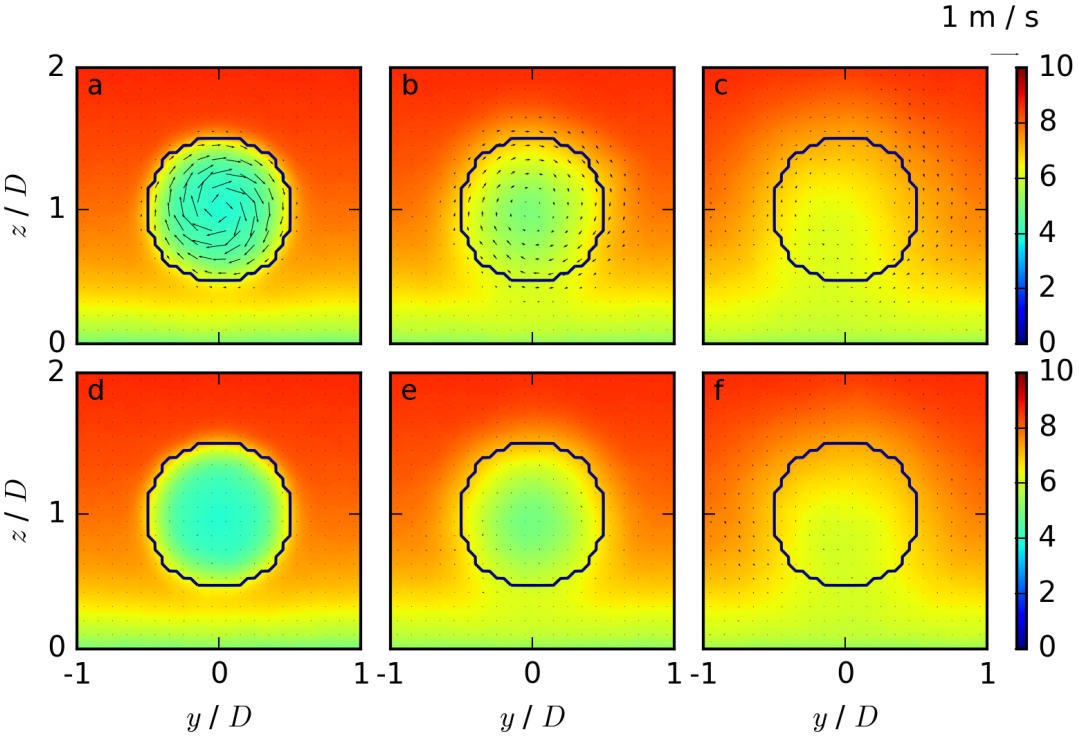

Figure 3.6: The averaged value of $\overline{u_{i,j,k}}$ in a y-z cross-section at downstream positions $x = 3D$ (a, d), $x = 10D$ (b, e), and $x = 20D$ (c, f) for simulation A_1 (a-c) and simulation A_NR (d-f). The arrows represent the wind vectors ($\overline{v_{i,j,k}}$, $\overline{w_{i,j,k}}$). The magnitude of 1 m s^{-1} is shown at the right edge of the plot.

using an explicit SGS closure model is verified with two further simulations, modifying the SGS closure model of simulation B_1. In the first simulation, the length scale of the TKE SGS closure model is multiplied by a factor of 1/2, resulting in the dotted red line in Fig. 3.5d, whereas in the second simulation, the length scale is multiplied by a factor of 2, resulting in the dashed red line. Decreasing (increasing) the length scale of the closure model results in a weaker (stronger) damping. A weaker damping induces larger turbulence, approaching the streamwise turbulent intensity behaviour of the implicit LES, whereas a stronger damping results in a weaker turbulent behaviour. The streamwise velocity ratios are nearly unaffected by the length scale of the closure model (not shown here).

The agreement between the established SGS schemes (TKE and Smagorinsky) is a remarkable result and confirms earlier findings by Smolarkiewicz et al. (2007). The possibility of an implicit LES of wind-turbine flows enables numerical simulations with stretched or adaptive meshes, where an explicit SGS parameterization might be difficult and troublesome.

The length scale of the closure model offers another tuning parameter in addition to α, which can explain the difference in the streamwise turbulent intensity in comparison to other simulation results from Wu and Porté-Agel (2011), Wu and Porté-Agel (2012), and Gomes et al. (2014), as mentioned before.

3.6 Summary

The investigation of the impact of NBL turbulence on wind-turbine wakes presents the following results:

The turbulence preserving method preserves the atmospheric background turbulence by applying the spectral energy distribution at every time step taken once from three 3 D fields (u, v, w) of the equilibrium state of an NBL precursor simulation. The entrainment in the wake can be modified in numerical simulations by adjusting the perturbation amplitude. An increase of the perturbation amplitude corresponds to larger atmospheric background turbulence and enhances the entrainment of air into the wake region, resulting in a shorter streamwise wake extension and an increase of the streamwise turbulent intensity.

According to the investigation of the wind-turbine parameterization, the BEM model yields a more accurate prediction of the near-wake characteristics and the wake structure of the two considered airfoils in the BEM model differs up to a streamwise distance of 14 D, whereas the MMT is a reasonable simplification of the BEM model for studies of the far wake. The rotation of the disc has an effect on the v and w wind components, resulting in a swirl in the whole wake.

Further, both SGS closure models as well as the implicit LES approach have a rather small impact on the streamwise velocity ratio. However, there is an impact on the streamwise turbulent intensity in the near wake, resulting in larger values for the implicit LES approach in comparison to the SGS closure models. The streamwise turbulent intensity of the simulations performed with the SGS closure models is strongly affected by the amount of damping in the corresponding SGS closure model.

The investigation of the impact of NBL turbulence on wind-turbine wakes constitutes the first step towards an increase of the wind-energy contribution to the primary energy demand. This investigation was necessary as first step, laying the groundwork for the investigation of the impact of ABL turbulence on wind-turbine wakes and also to validate the application of the turbulence preserving method, which is the basic concept for the numerically efficient parameterization of turbulent wind-turbine flows for LES of different thermal stratifications.

4 Impact of the diurnal cycle of the atmospheric boundary layer on wind-turbine wakes

In this chapter, the impact of the diurnal cycle of the ABL on wind-turbine wakes is investigated by applying the diurnal cycle simulation setup and the interface between ABL and wind-turbine simulations from Chapter 2. A detailed investigation of the idealized ABL simulations of the diurnal cycle over homogeneous and heterogeneous surface is given in the following. Further, wind-turbine simulations are investigated for the CBL, the EBL, the SBL, and the MBL over homogeneous surface, with special attention given to the wake structure, the wake deflection, the streamwise velocity ratio, the turbulent intensity, the temporal average, and the second diurnal cycle. Over heterogeneous surface, the wind-turbine simulations are investigated for the CBL and the SBL and are compared to the corresponding simulation over homogeneous surface.

As explained in the Introduction, this investigation is the key to understand how a wind turbine operates under different atmospheric conditions, additionally influenced by different surface conditions.

4.1 Idealized atmospheric boundary-layer simulation

Evolution

The temporal evolution of the sensible heat flux at the surface, the vertical time series of the simulated potential temperature $\Theta = \Theta_e + \Theta'$, and of the resolved TKE (Eq. (2.20)) are shown in Fig. 4.1. The evolution of the potential temperature corresponds to the sensible heat flux with a warming of the surface during the day and a cooling at night and corresponds to the BLLAST ABL simulation and to Stull (1988), Kumar et al. (2006), and Basu et al. (2008). The magnitude and the vertical extent of the resolved TKE in Fig. 4.1*c* show a maximum during the day and a minimum during the night, in response to the simulated turbulence in the ABL. The maximum of TKE has a delayed response to the maximum surface heat flux of approximately 2 h. The resolved TKE evolution with a higher reaching maximum at the second day is comparable to Abkar et al. (2016).

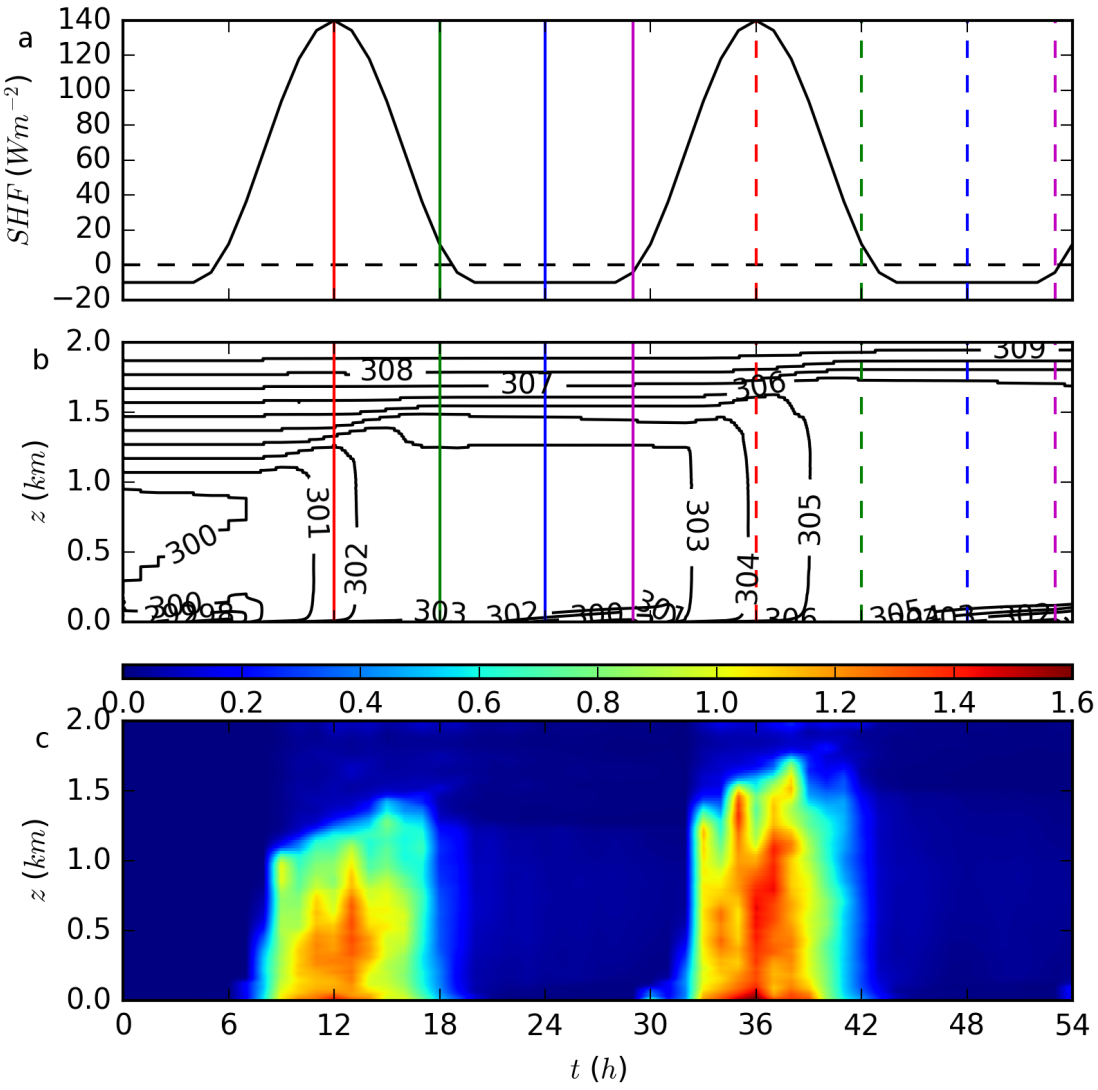

Figure 4.1: Temporal evolution of the sensible surface heat flux in W m^{-2} in *a*, vertical time series of the horizontal average of the potential temperature Θ in K in *b*, and of the horizontal average of the resolved TKE $\overline{e}$ in m^2 s^{-2} in *c*. The red (green, blue, magenta) line corresponds to the times when the background and initial fields are extracted for the CBL (EBL, SBL, MBL) wind-turbine simulation. The solid lines correspond to day 1, whereas the dashed lines represent day 2.

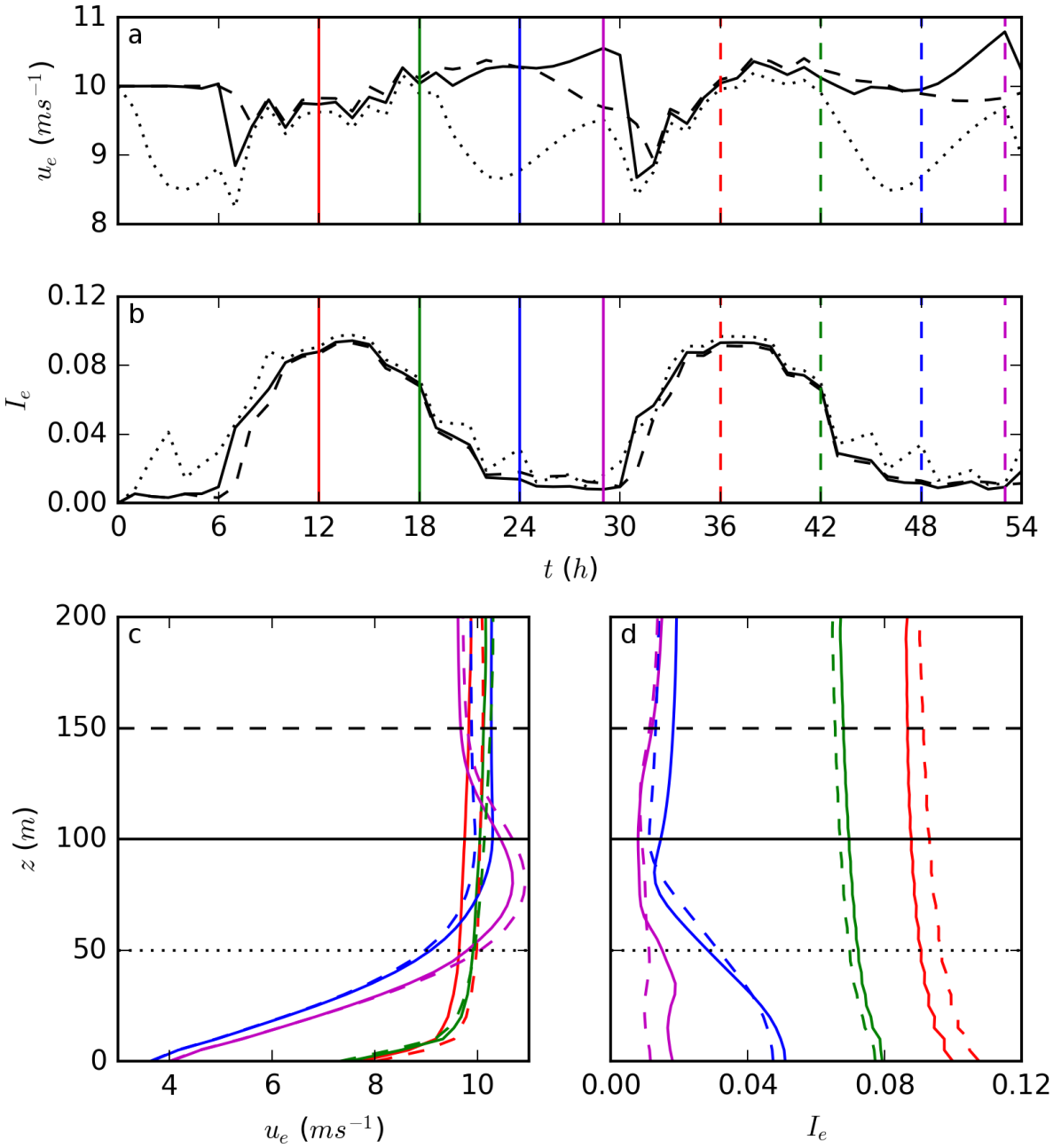

Figure 4.2: Temporal evolution of the horizontal average of u and I as u_e and I_e at hub height (100 m; black solid line), top tip (150 m; black dashed line) and bottom tip (50 m; black dotted line) of a wind turbine with $D = 100$ m and $z_h = 100$ m in *a* and *b*. Vertical profiles of u and I are shown in *c* and *d*.

Atmospheric variables relevant to wind-energy research

Wind speed, wind shear, and the level of atmospheric turbulence are the most important atmospheric variables in wind-energy research (Naughton et al., 2011; Emeis, 2013, 2014; Abkar and Porté-Agel, 2014; Abkar et al., 2016), with a major impact on the structure of the flow field behind a wind turbine, the power loss, and the flow-induced dynamic loads on downwind turbines. The temporal evolution of the horizontal average of the streamwise velocity u and the turbulent intensity I of the idealized ABL simulation are presented in Fig. 4.2*a* and *b* as u_e and I_e at hub height and at the height of the top tip and bottom tip of a wind turbine with $D = 100$ m and $z_h = 100$ m. The corresponding vertical profiles of u_e and I_e are shown in Fig. 4.2*c* and *d*. In the following, the total turbulent intensity from Eq. 2.25 is used instead of the turbulent intensity from Eq. 2.24, as the spanwise and vertical contribution of the turbulent intensity becomes important during the diurnal cycle (Abkar et al., 2016).

The streamwise wind speed u_e at a certain height in Fig. 4.2*a* is marginally impacted by the prescribed forcing during daytime conditions. All heights have nearly the same u_e-values due to the presence of the CBL. The variation between top tip, hub height, and bottom tip increases during the night. This difference between the day and the nighttime behaviour results from the vertical wind shear, as shown in Fig. 4.2*c*. Specifically, in the CBL and in the EBL the vertical wind shear is rather small, whereas in the SBL and in the MBL it is very pronounced. A supergeostrophic situation prevails during the MBL near hub height corresponding to an LLJ with a change in wind shear from a positive value below to a negative value above the LLJ.

Similar wind characteristics are found in Magnusson and Smedman (1994), Beare et al. (2006, Fig. 3), Kumar et al. (2006, Fig. 5), Basu et al. (2008, Fig. 3), Beare (2008, Fig. 2*b*), Bhaganagar and Debnath (2014, Fig. 1), Abkar and Porté-Agel (2014, Fig. 2*a*), Vollmer et al. (2016, Fig. 3*a*), and Abkar et al. (2016, Fig. 5*a*), amongst others. Further, a supergeostrophic situation also exists in the SBL simulation of Aitken et al. (2014, Fig. 4), Bhaganagar and Debnath (2014, Fig. 1*a*), and Bhaganagar and Debnath (2015, Fig. 1), as well as in the diurnal cycle simulation of Abkar et al. (2016, Fig. 15*a*). In this simulation, the LLJ is not yet prevalent in the SBL, only a positive wind shear exists between bottom tip and hub height (Fig. 4.2*c*). Generally, the onset time as well as the height of the LLJ depend on the amount of infrared irradiation at night and on the atmospheric situation of the previous day (Bhaganagar and Debnath, 2014, 2015).

The diurnal cycle has a large impact on the total turbulent intensity in Fig. 4.2*b* with a maximum during the day and a minimum during the night, because the negative buoyancy damps the turbulence at night (Fig. 4.1*c*). The stratification results in much larger values of I_e for the CBL and the EBL and only small values for the SBL and the MBL, as shown in Fig. 4.2*d*. Further, a maximum in the streamwise turbulent intensity occurs below the LLJ (not shown here).

The diurnal behaviour, the order of magnitude, and the shape of the vertical profiles in Fig. 4.2*b* and *d* agree with investigations of Beare (2008, Fig. 4), Blay-Carreras et al. (2014, Fig. 7), Bhaganagar and Debnath (2014, Fig. 1), Abkar and Porté-Agel (2014, Fig. 2$a, e-f$), Vollmer et al. (2016, Fig. 3a), and Abkar et al. (2016, Fig. 3f, Fig. 5c, Fig. 15a), amongst others.

Therefore, the larger turbulent intensity in the CBL in comparison to the SBL is supposed to result in an enhanced entrainment of ambient air into the wake region and, therefore, in a more rapid flow recovery in the wake. The similar structures of u_e and I_e in the CBL and in the EBL as well as in the SBL and in the MBL reveal a strong influence of the convective or stable stratification on the subsequent transitions. Similar transition behaviours are documented in Abkar et al. (2016). Therefore, the flow field in the wake of the wind turbine is supposed to be rather similar in the CBL and in the EBL as well as in the SBL and in the MBL. Amongst others, both assumptions are investigated in the following.

4.2 Wind-turbine simulations

The flow from the idealized ABL simulation over homogeneous surface is used as background, initial, and inflow conditions in the following wind-turbine simulations to investigate the wake structure for different diurnal cycle regimes with the coupling method described in Chapter 2.

Wake structure

The streamwise velocity for all four cases (CBL, EBL, SBL, MBL) is displayed in the x-z plane in Fig. 4.3 and in the x-y plane in Fig. 4.4. The upstream region differs for the CBL and the EBL in comparison to the SBL and the MBL. This is caused by the difference in the upstream u_e profiles in Fig. 4.2*c*. The general spatial structure results in a flow deceleration in the wake of the wind turbine and a recovery of the flow further downstream of the wind turbine. The downstream position of the flow recovery depends on the state of the ABL evolution, particularly on I_e. It is closer to the wind-turbine rotor for the CBL and further away for the SBL.

More precisely, the maximum velocity deficit is 50 % in the CBL and 70 % in the SBL. The flow in the wake also recovers more rapidly in the CBL in comparison to the SBL. The enhanced entrainment in the CBL results from larger vertical and lateral momentum fluxes in Fig. 4.5. The large momentum fluxes are related to the increase of TKE, as shown in Fig. 4.1*c*, and the largest values of I_e during the diurnal cycle, as shown in Fig. 4.2*b* and *d*. The different entrainment rate results in a longer streamwise wake extension in the SBL in comparison to the CBL. These wake characteristics confirm the assumption of the more rapid flow recovery in the wake for decreasing stability of the atmospheric regime and

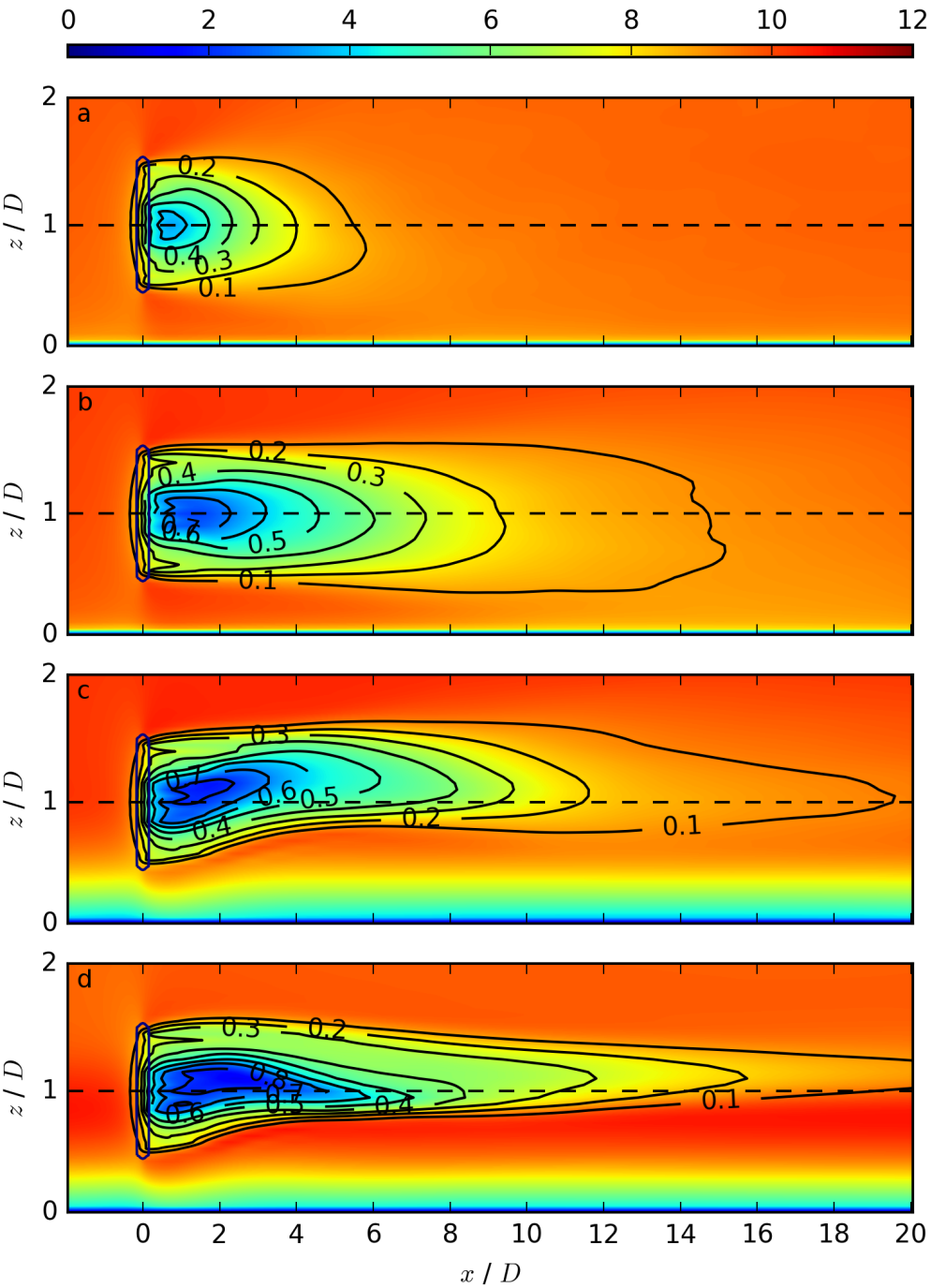

Figure 4.3: Contours of the streamwise velocity $\overline{u_{i,j_0,k}}$ in m s^{-1} at a spanwise position of j_0, corresponding to the centre of the rotor, for CBL in *a*, EBL in *b*, SBL in *c*, and MBL in *d*. The black contours represent the velocity deficit $VD_{i,j_0,k}$ at the same spanwise location.

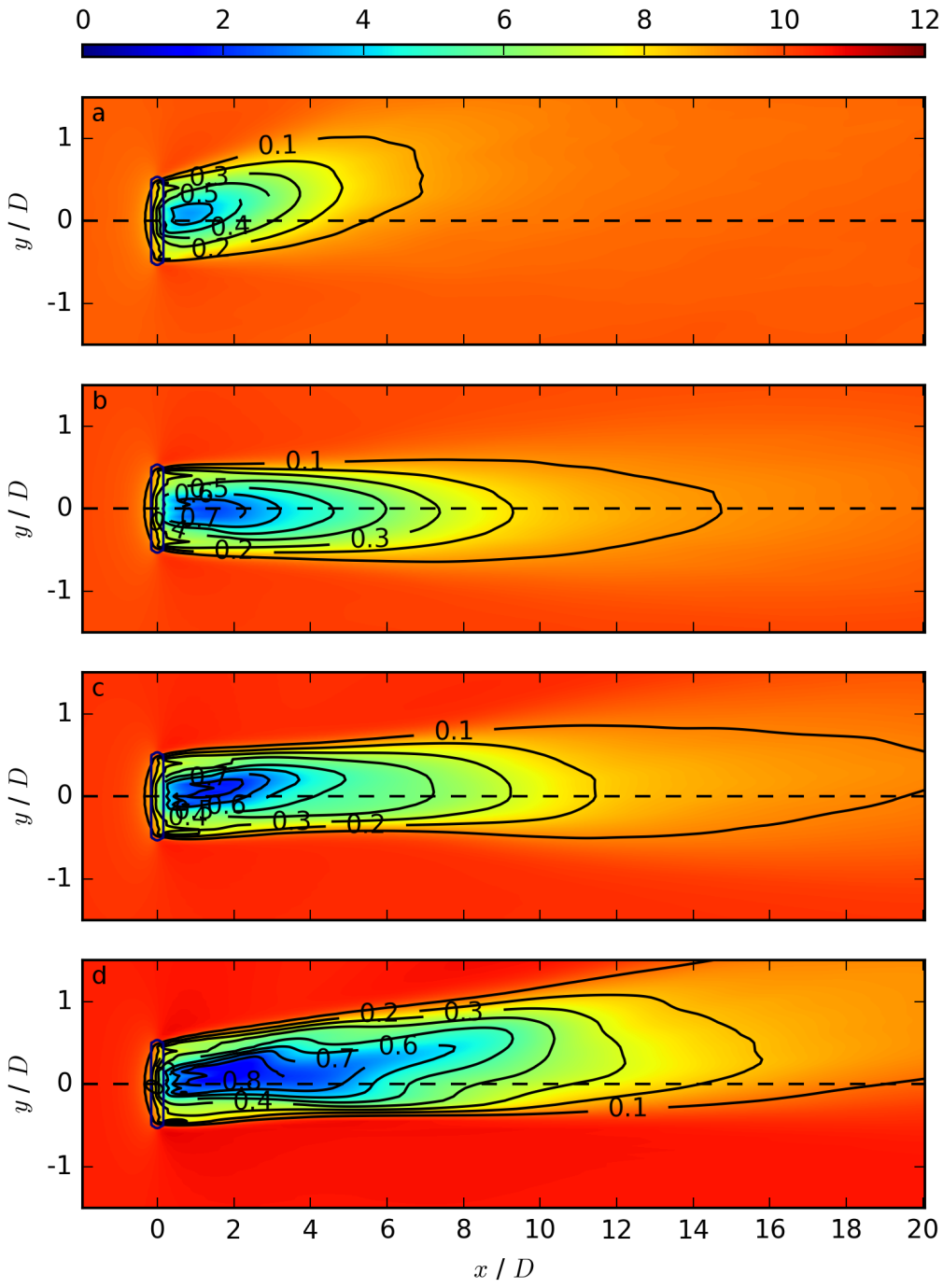

Figure 4.4: Contours of the streamwise velocity $\overline{u_{i,j,k_h}}$ in m s^{-1} at hub height z_h for CBL in *a*, EBL in *b*, SBL in *c*, and MBL in *d*. The black contours represent the velocity deficit VD_{i,j,k_h} at the same vertical location.

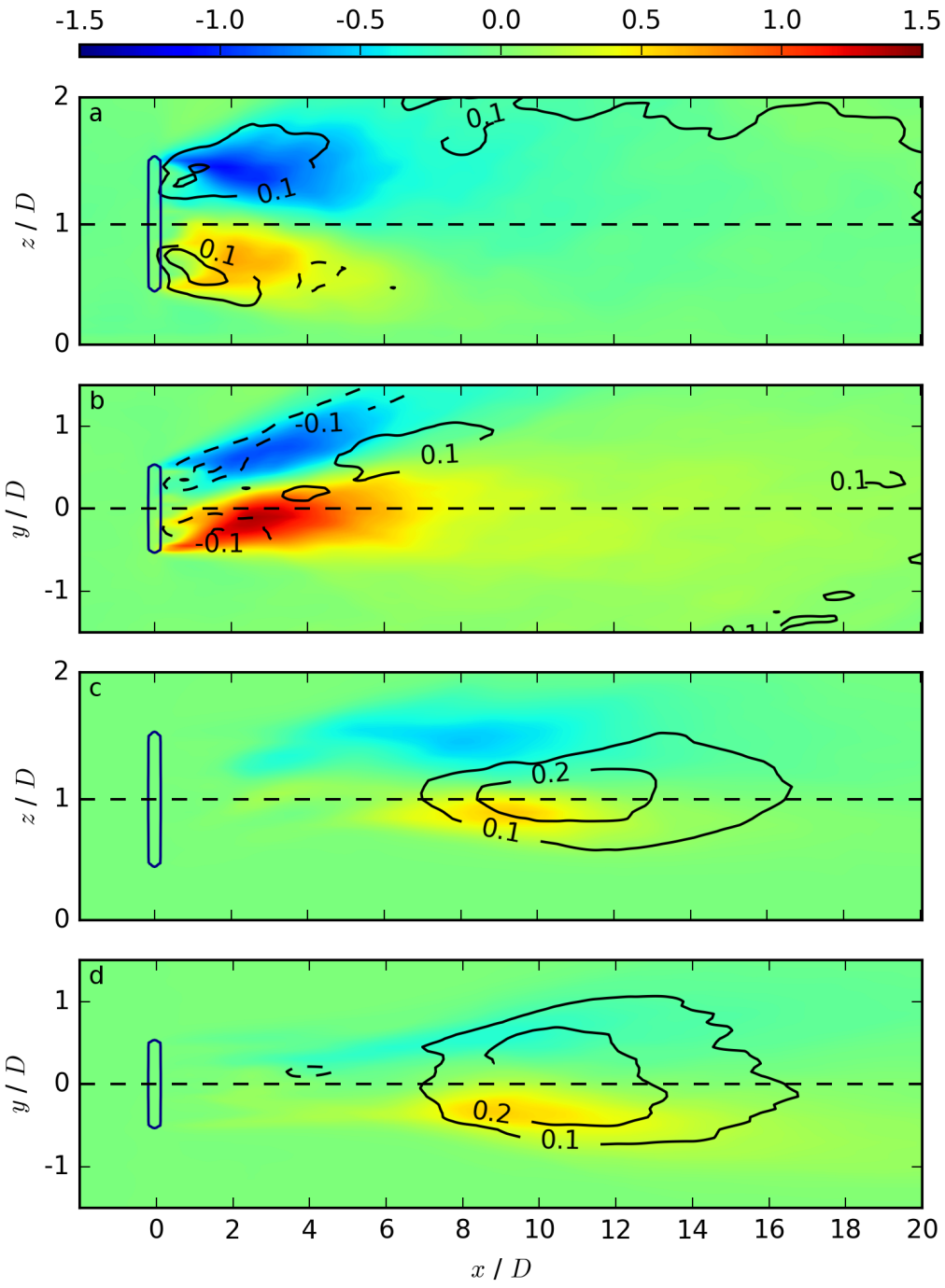

Figure 4.5: Contours of the vertical momentum flux $\overline{u'w'}$ in the x-z plane at a spanwise position of j_0, corresponding to the centre of the rotor, for the CBL in *a* and for the SBL in *c*, and of the lateral momentum flux $\overline{u'v'}$ in the x-y plane at hub height z_h for the CBL in *b* and for the SBL in *d*. The contours represent $\overline{v'w'}$.

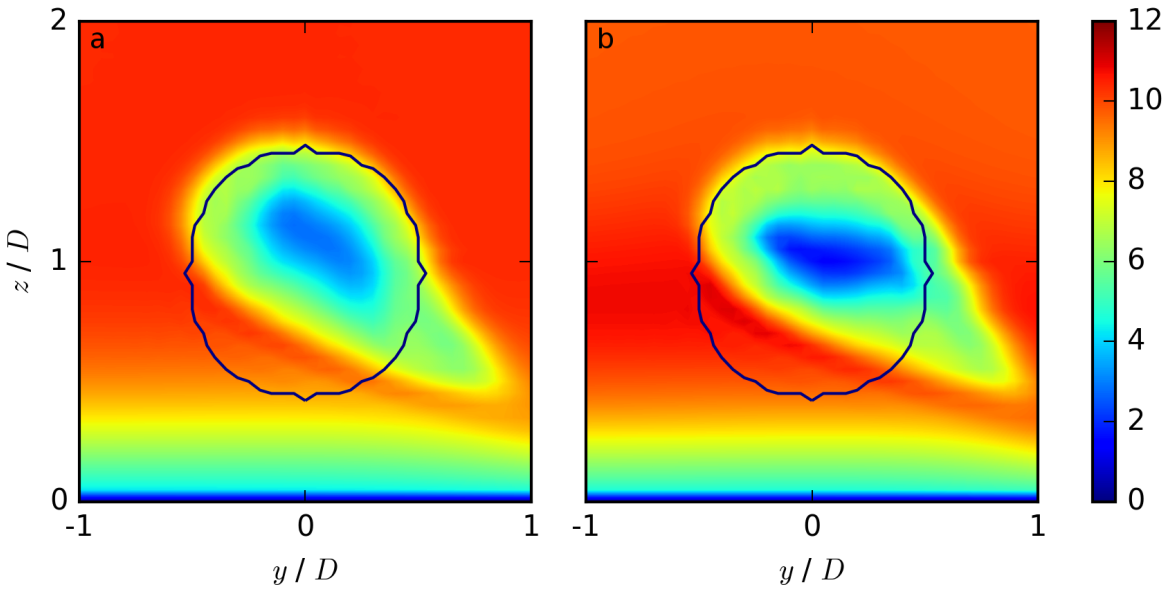

Figure 4.6: Contours of the streamwise velocity $\overline{u_{i=3D,j,k}}$ in m s^{-1} at a downward position of 3 D for the SBL in *a* and the MBL in *b*. Here, $y/D \in [0, 1]$ corresponds to a northwards direction (wind direction $> 270°$ and wake deflection $< 90°$) and $y/D \in [-1, 0]$ to a southwards direction (wind direction $< 270°$ and wake deflection $> 90°$).

agree with previous investigations by Abkar and Porté-Agel (2014), Mirocha et al. (2015), Vollmer et al. (2016), and Abkar et al. (2016).

The recovery of the flow in the wake and the velocity deficit of the EBL (MBL) are comparable to the CBL (SBL) with a slightly longer wake region and larger velocity deficit values of 60 % for the EBL (80 % for the MBL). The vertical and lateral momentum fluxes of the EBL (MBL) are also comparable to the CBL (SBL), with slightly smaller values for increasing stability of the atmospheric regime. The wake pattern verifies the assumption of the influence of the flow regime prior to the transitions on the wake during the transition phases.

The positive (negative) vertical and lateral momentum fluxes of $\overline{u'w'}$ and $\overline{u'v'}$ for the CBL and the SBL in Fig. 4.5 correspond to negative (positive) vertical and lateral gradients of the streamwise velocity in the wake (Figs. 4.3 *a* and *c*, 4.4 *a* and *c*). The large lateral momentum flux $\overline{u'v'}$ in the CBL can be attributed to a higher level of turbulence during the day (Fig. 4.2*b* and *d*) and the deflection of both maxima of $\overline{u'v'}$ towards the north can be attributed to the wake deflection in Fig. 4.4*a*. The positive momentum fluxes of $\overline{v'w'}$ in the CBL (Fig. 4.5*a*) are in agreement with a negative vertical gradient of the lateral velocity, whereas the negative momentum fluxes of $\overline{v'w'}$ (Fig. 4.5*b*) correspond to a positive vertical gradient of the lateral velocity. The maxima and minima of $\overline{u'w'}$, $\overline{u'v'}$, and $\overline{v'w'}$ are located in the near wake in the CBL, whereas they are in the far wake in the SBL. This difference is caused by the enhanced turbulent mixing in the near wake during the day. At night, the

near wake is dominated by advection processes and a deflection of the wake resulting from the Coriolis effect, and turbulent diffusion is gradually amplified in the far wake.

The wake structure, as shown in Fig. 4.3, is symmetric with respect to the centre line in the CBL and in the EBL, whereas it is asymmetric in the SBL and in the MBL. The asymmetric wake structure is presented in Fig. 4.6, where large u-values occur in the lower rotor part for $z < z_h$. This characteristic wake structure of the SBL and the MBL results from the deflection of the wake towards the north ($y/D \in [0, 1]$) and will be explained in the following.

Wake deflection

Different horizontal deflections of the wake from an eastward propagating wake (no wake deflection ≡ wake deflection angle of 90°) occur for the different regimes (Fig. 4.4). The wake deflections at hub height averaged over the near and the far-wake region are 6° to the north in the CBL (wake deflection angle = 84°), 0° in the EBL (wake deflection angle = 90°), and 1° to the north in the SBL and in the MBL (wake deflection angle = 89°). To investigate the height dependence of the wake deflection, the wind directions during the diurnal cycle at bottom tip, hub height, and top tip are shown in Fig. 4.7*c*. Additionally, the wake deflections at these three heights (bt, hub, tt) are plotted as averages over the whole wake for the CBL, the EBL, the SBL, and the MBL. Vertical profiles of the horizontal average of the wind direction for the four regimes are shown in Fig. 4.7*a* and the corresponding wind hodographs in Fig. 4.7*b*. The upstream wind conditions at bottom tip, hub height, and top tip correspond to the markers in Fig. 4.7*b*.

The upstream wind direction is nearly constant in the CBL and in the EBL, corresponding to nearly uniform values of u_e and v_e in the hodograph for the EBL. The hodograph for the CBL is comparable to the EBL and is not shown here. For the SBL and the MBL, the upstream wind direction has a large vertical gradient between bottom tip and top tip and, therefore, a significant veering in the hodograph, which is especially pronounced in the lower rotor part. The wake deflections (markers in Fig. 4.7*c*) in the CBL and in the EBL are nearly constant at the height of the rotor area. They change with height in the SBL and in the MBL from bottom tip to top tip from a northwards wake deflection (wake deflection angle 75°) towards no wake deflection (wake deflection angle 90°). This corresponds to the deformed wake towards the north in the lower rotor part in the y-z plane for the SBL in Fig. 4.6 *a* and for the MBL in Fig. 4.6 *b*. Similar wake behaviour as in the SBL and in the MBL was found in the stable regime simulated by Lu and Porté-Agel (2011), and Vollmer et al. (2016), and in the low-stratified regime simulated by Bhaganagar and Debnath (2014). Further, the different wake deflections with height result in a rather compact streamwise and spanwise domain extension in the CBL and in the SBL and a correspondingly larger streamwise and spanwise domain extension in the SBL and in the MBL.

The wake deflections in Fig. 4.7*c* correspond largely to the upstream wind directions for all ABL regimes and at all heights. The small deviations in the CBL and in the EBL decrease, if only the averaged wind direction of the part of the precursor simulation which directly interacts with the wind turbine (20 grid points instead of 512) is considered. In this case, the meridional component in the CBL (EBL) is slightly stronger (weaker) than the horizontal average over the complete domain. The modified wind direction results in a larger (smaller) deviation from a westward wind than it is the case for the whole domain, and therefore the wake deflection direction of the CBL (EBL) perfectly reflects the wind deflection.

Streamwise velocity ratio and turbulent intensity

Figure 4.8 compares the dependencies of the streamwise velocity ratio and the total turbulent intensity through the centre of the rotor with measurements and numerical studies as listed in Table 3.2. The velocity ratio values of the CBL in Fig. 4.8*a* are in agreement with the CBL results from Mirocha et al. (2014) for $x \geq 3$D. The EBL results are compared to NBL results, as no other published EBL wind-turbine simulations exist. For the EBL, the EULAG results are in agreement with the NBL simulations of Wu and Porté-Agel (2011, 2012) for the smaller roughness length value. For the SBL, the simulation results of this study are in good agreement with SBL measurements and numerical simulation results from Aitken et al. (2014). For the MBL, the EULAG results are comparable to the SBL with smaller values resulting from the more stable situation (Fig. 4.2*d*).

The total turbulent intensity profiles in Fig. 4.8*b* through the rotor centre in the EBL, the SBL, and the MBL are comparable to the range of other NBL LES results with different values of the roughness length in Wu and Porté-Agel (2011, 2012). The values are larger in the near wake in the CBL in comparison to the EBL, the SBL, and the MBL, resulting from the domination of the streamwise turbulent intensity component over the spanwise and vertical components (not shown here). Compared to the RANS simulation of Gomes et al. (2014), the values are smaller in the LES of this study. The velocity ratio in Fig. 4.8*a*, however, is comparable for LESs and RANS simulations, which indicates a strong dependence of the total turbulent intensity in the far wake on the numerical model, as shown in Chapter 3.

To test whether the velocity ratio and the total turbulent intensity values at i, j_0, and k_h are representative for the whole wake, especially regarding the wake deflections in Fig. 4.4, an average of VR and I (dashed lines) is taken at k_h for all grid points with a velocity deficit > 0.1 in lateral direction, denoted by $< VR_{i,j,k_h} >_{VR>0.1}$ and $< I_{i,j,k_h} >_{VR>0.1}$. This lateral average corresponds to the area within the 0.1 contour in Fig. 4.4 and considers the wake deflections. For the calculation of the velocity deficit in Eq. 2.22, $< \overline{u_{i_1,k_h}} >_j$ is used in the denominator as lateral average instead of a grid point value $\overline{u_{i_1,j,k_h}}$.

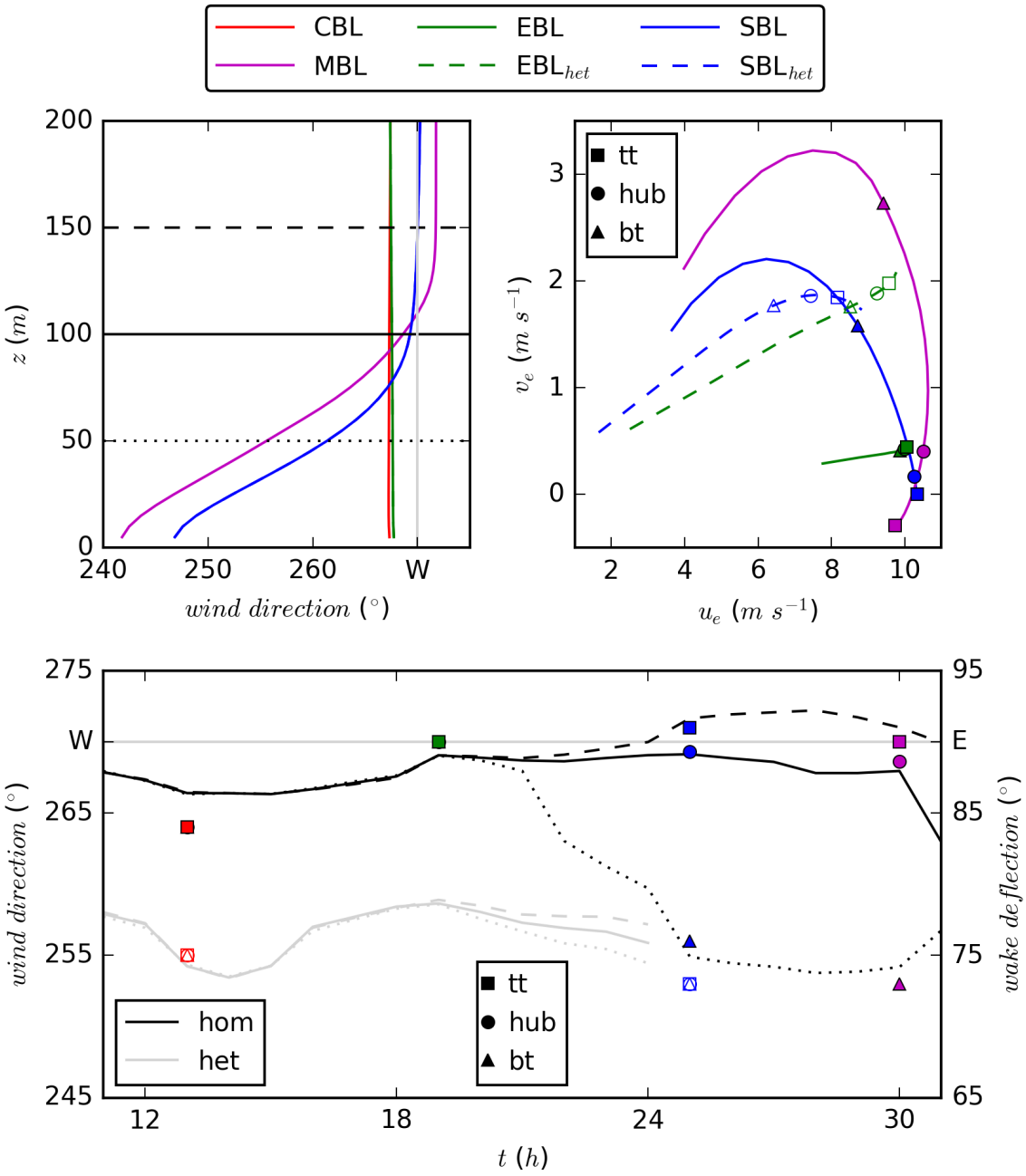

Figure 4.7: Vertical profiles of the wind direction of the idealized ABL precursor simulation over homogeneous surface are shown in *a*. The solid vertical gray line in *a* corresponds to a wind from the west. Wind hodographs, based on the mean zonal and meridional wind velocities u_e and v_e are shown in *b* for EBL, EBL$_{het}$, SBL, SBL$_{het}$, and MBL. Time evolution of the wind direction for the idealized ABL over homogeneous (black) and heterogeneous (gray) surface is shown in *c*. The markers correspond to the wind direction (in *b*) and wake deflection (in *c*) at bottom tip (bt), hub height (hub), and top tip (tt). The filled markers represent the homogeneous case, whereas the empty markers represent the heterogeneous case. The black lines in *a* and *c* correspond to a height of 50 m (dotted line), 100 m (solid line), and 150 m (dashed line).

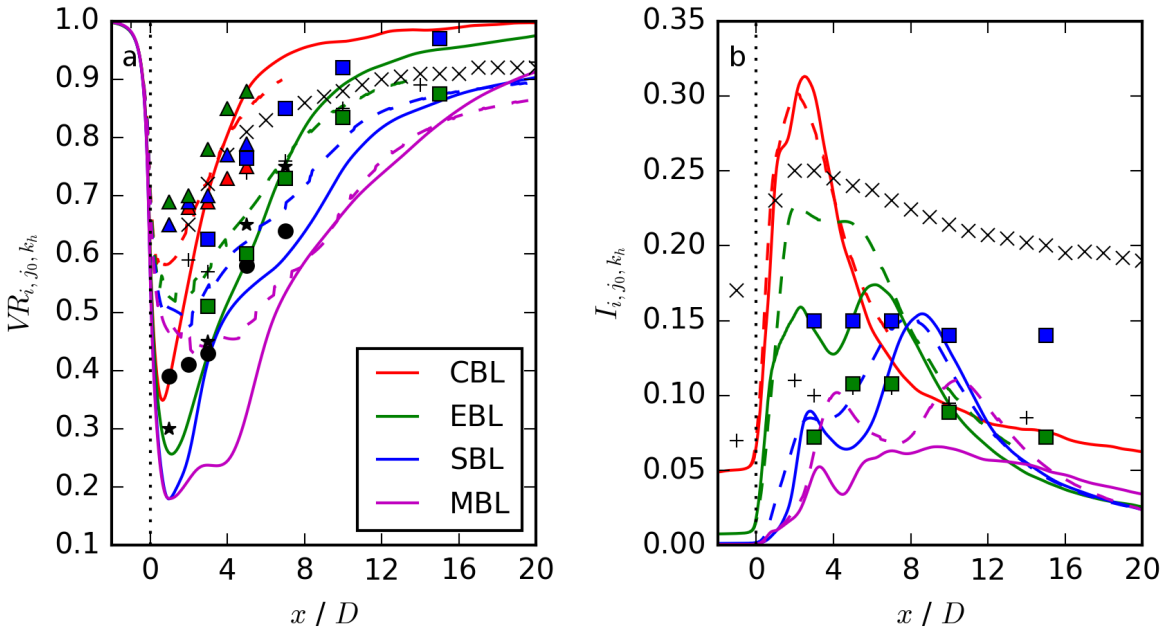

Figure 4.8: Dependency of the streamwise velocity ratio VR_{i,j_0,k_h} in a and the total turbulent intensity I_{i,j_0,k_h} in b for the wind-turbine simulations CBL, EBL, SBL, and MBL through the centre of the rotor in spanwise (j_0) and vertical (k_h) direction (solid lines). The dashed lines correspond to the average of the streamwise velocity ratio and the total turbulent intensity in the wake at hub height z_h for $VR > 0.1$. The markers correspond to various studies as listed in Table 3.2.

The averaged velocity ratio in Fig. 4.8a (dashed lines) is smaller due to including the complete wake with decreasing VR values at the rotor edges. The individual relation between the different regimes is comparable to VR_{i,j_0,k_h}, with the maximum VR in the CBL and the minimum in the MBL. A comparison to other studies is not possible, as the markers correspond to downstream values located at the centre of the rotor area.

The averaged total turbulent intensity values in Fig. 4.8b (dashed lines) are rather comparable to I_{i,j_0,k_h}. Especially in the CBL and in the SBL, the dashed and solid lines are nearly overlapping. Minor differences occur in the EBL and in the MBL. Further, the individual relation between the different regimes is still prevalent, with a maximum of the total turbulent intensity in the CBL and a minimum in the MBL.

The streamwise development of VR_{i,j_0,k_h} and I_{i,j_0,k_h} through the centre of the rotor are in agreement with the averaged values of $< VR_{i,j,k_h} >_{VR>0.1}$ and $< I_{i,j,k_h} >_{VR>0.1}$ and can therefore be considered as representation of the whole wake. For a larger deviation of the wind direction from a westward wind than it is the case in this study, the averaged values might be more significant.

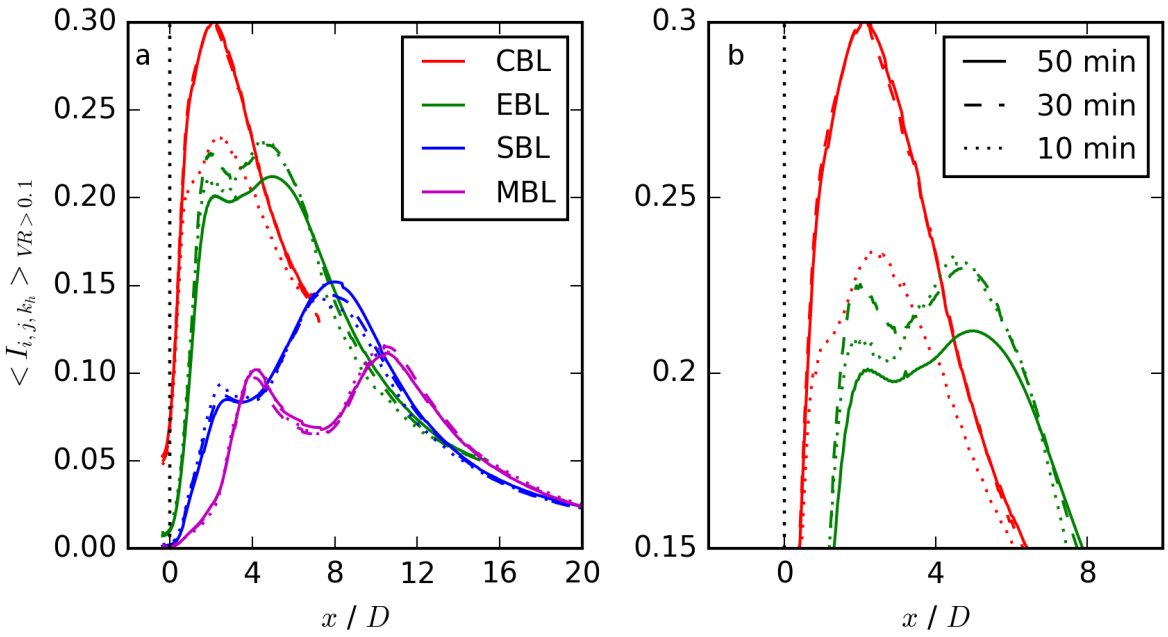

Figure 4.9: Turbulent intensity $< I_{i,j,k_h} >_{VR>0.1}$ as function of x/D averaged over all grid points at hub height z_h with $VR > 0.1$ for the CBL, the EBL, the SBL, and the MBL wind-turbine simulations in *a*. $< I_{i,j,k_h} >_{VR>0.1}$ is plotted for time average periods of 10 min, 30 min, and 50 min, respectively. The upper section of the difference time averages of $< I_{i,j,k_h} >_{VR>0.1}$ for the CBL and the EBL in *b*.

Temporal average

To test whether the applied 50-min averaging period is sufficient to generate statistically converged results, the total turbulent intensities for the CBL, the EBL, the SBL, and the MBL are shown in Fig. 4.9 for time averages of 10 min, 30 min, and 50 min, respectively. Here, $< I_{i,j,k_h} >_{VR>0.1}$ is averaged over all grid points at hub height with $VR > 0.1$.

The total turbulent intensities for the SBL and the MBL are independent of the averaging time and follow the same spatial profiles. The difference of $< I_{i,j,k_h} >_{VR>0.1}$ for the CBL between the 10-min and the 30-min averages is large. However, between the 30-min and 50-min averages, there is no significant difference. Already an averaging time of 20 min already corresponds to the 30-min profile (not shown here), which means the simulation results are statistically stable after about 20 min averaging time. The difference after 10 min in comparison to the longer temporal averages results from insufficient time for the wake to reach an equilibrium state with statistical convergence of the results.

In the EBL, the 10-min and 30-min averages are rather similar, whereas the total turbulent intensity profiles deviate significantly for the 50-min values. The 40-min values correspond to the 50-min values (not shown here). The difference between an averaging time of 30 min and 40 min can be related to the buoyancy contribution to turbulence, which is controlled

by the temporal evolution of the surface heat flux as shown in Fig. 4.1*a*. The decreasing surface flux is still positive after 10 min (17 h and 10 min) and 30 min (17 h and 30 min), crossing zero after 40 min (17 h and 40 min), and is negative after 50 min averaging time (17 h and 50 min).

In contrast to the EBL, no changes in the total turbulent intensities occur in the MBL for longer averaging periods. Here, the surface fluxes become positive after about 10 min. This different behaviour can be explained by the longer time scales in the MBL related to the growth of turbulent eddies by forming a fully convective layer. In contrast, the surface cooling leads to a fast response of the lowest few hundred metres of the atmosphere to the absence of thermals in the EBL.

Different time periods were chosen in previous studies to average the respective numerical results. For the SBL, Bhaganagar and Debnath (2014) averaged over 100 s, Mirocha et al. (2015) over 10 min, Vollmer et al. (2016) over 20 min, and Abkar et al. (2016) over 1 h. According to the investigation in this study, all of these averaging periods lead to the same result. Therefore, an averaging period of 10 min is sufficient and preferred, regarding the computational costs.

As other wind-turbine simulations of the EBL have not yet been published, the applied averaging period is compared to available simulations of the NBL. For example, Vollmer et al. (2016) averaged over 20 min, similar to their SBL case. If the surface fluxes did not cross zero, this time period would also be appropriate for my simulation. However, as mentioned above, the situation is different for the EBL due to the surface cooling. Therefore, the applied time scale cannot be compared to the NBL simulation with zero surface heat flux.

For the CBL, the values used in the literature reveal a wide spread of averaging time. Mirocha et al. (2015) averaged over 10 min, Abkar et al. (2016) and Vollmer et al. (2016) over 1 h. Vollmer et al. (2016) motivated this long averaging period by positive and negative meridional winds, resulting in a local inflow wind direction, which differs from the wind direction averaged over the whole domain. In the presented CBL simulation, the meridional wind component is always positive from 12 h to 13 h for the 20 grid points, that have a direct influence on the wind-turbine wake. Therefore, a 20-min average is sufficient in the CBL case of this thesis to reach an equilibrium state with statistical convergence of the results.

Second diurnal cycle impact

The impact of the second diurnal cycle on the wind direction of the idealized precursor simulation over homogeneous surface and the velocity deficit of the synchronized wind-turbine simulations are investigated in Fig. 4.10 for CBL_2, EBL_2, SBL_2, and MBL_2 and are compared to the results of the first diurnal cycle of CBL, EBL, SBL, and MBL. The vertical profiles at $x = 4$D in Fig. 4.10*c* and the lateral profiles in Fig. 4.10*d* indicate small differences

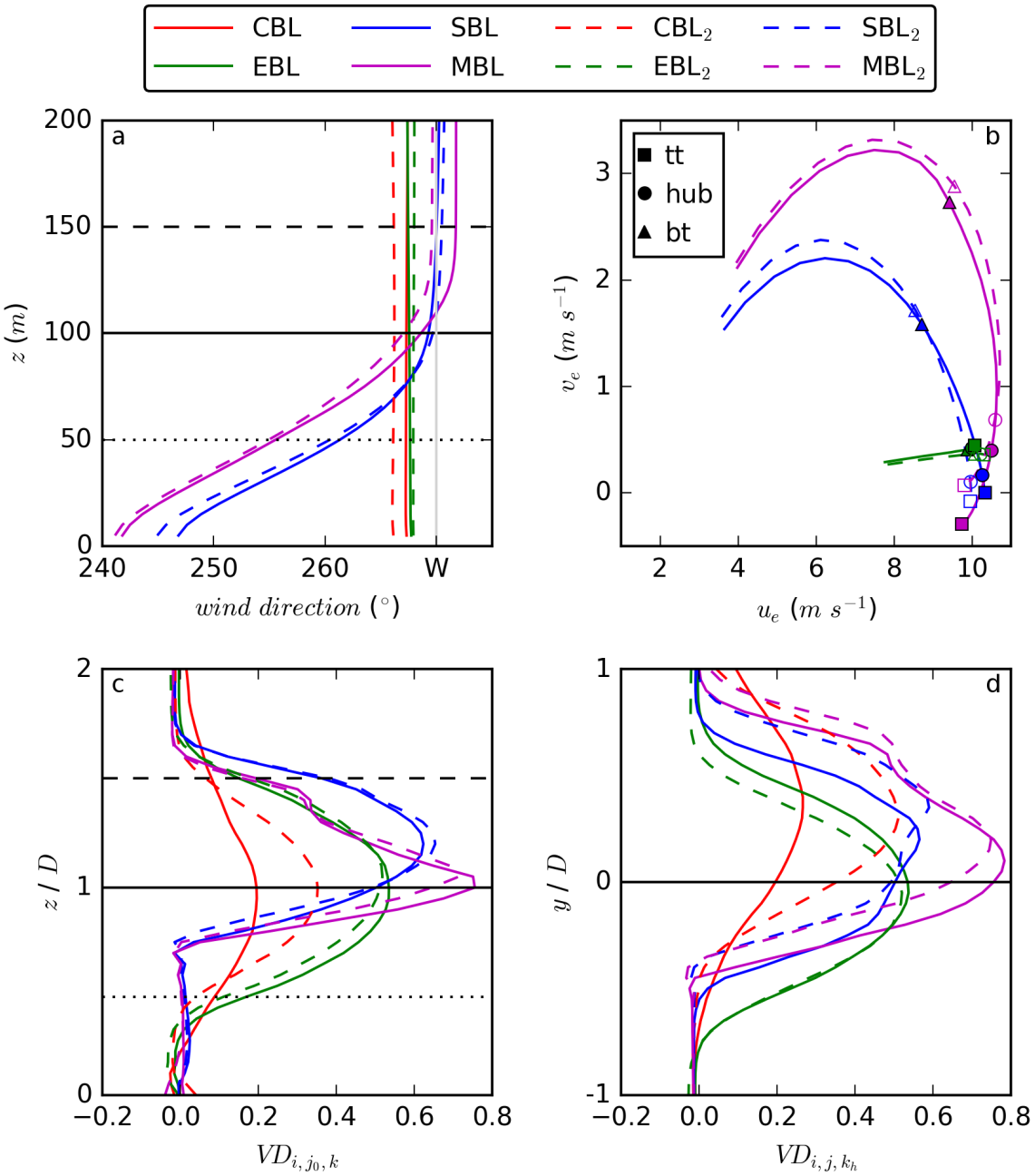

Figure 4.10: Vertical profiles of the wind direction of the idealized ABL precursor simulation over homogeneous surface are shown in *a*. The solid vertical gray line in *a* corresponds to a wind from the west. Wind hodographs, based on the mean zonal and meridional wind velocities u_e and v_e are shown in *b* for EBL, EBL_2, SBL, SBL_2, MBL, and MBL_2. The markers correspond to a height of 50 m (bottom tip, bt), 100 m (hub height, hub), and 150 m (top tip, tt). The filled markers represent day 1, whereas the empty markers represent day 2. A comparison of the vertical profiles of $VD_{i,j0,k}$ between day 1 and day 2 of the wind-turbine simulations at $x = 4$D in *c* and of the horizontal profiles of VD_{i,j,k_h} at $x = 4$D in *d*.

in the wake extension: The larger wake deflection in SBL_2 and MBL_2 in comparison to SBL and MBL in Fig 4.10*d* results from the slightly different angle of the wind direction and the deviation in the hodograph at hub height in Fig. 4.10*a* and *b*. The similar wake deflections in CBL_2 and EBL_2 in comparison to CBL and EBL correspond to the rather similar vertical profiles of the wind direction and the wind hodograph in Fig 4.10*a* and *b*. Further, the streamwise wake extension in Fig. 4.10*c* and *d* is larger in CBL_2 in comparison to CBL, whereas it is rather comparable for all other stratifications. This is contradictory to the slightly higher total turbulent intensity in Fig. 4.2*d* for CBL_2 in comparison to CBL. However, the larger wake extension in CBL_2 can be related to the more stable atmospheric stratification at night 1 in comparison to the initialisation night zero in Fig. 4.1*b*. In addition, the vertical profiles of $VD_{i,j_0,k}$ in CBL and CBL_2 are influenced by the slightly different wake deflection and are not directly comparable at grid point j_0.

The general wake structure is rather similar for the two corresponding wind-turbine simulations on both days. Individual minor differences are possible and are affected by the previous ABL characteristics. The investigation of the second diurnal cycle results in no significant influence on the initial conditions of the idealized ABL simulation after 12 h. This verifies the application of the first diurnal cycle in the previous section for the investigation of the wind-turbine wake.

4.3 Heterogeneous surface

Idealized diurnal cycle simulation over heterogeneous surface

The vertical time series of potential temperature and resolved TKE for the idealized diurnal cycle simulation over a heterogeneous surface (as described in Section 5.2) show essentially the same behaviour above the blending height as those from the idealized diurnal cycle simulation over a homogeneous surface shown in Fig. 4.1. The main difference occurs below the blending height, which is > 200 m, due to the enhanced shear induced by the obstacles on the ground. Figure 4.11 reveals that the shear production term is significantly larger compared to the homogeneous run during the complete diurnal cycle. Further, the shear production term has the same order of magnitude as the buoyancy budget term during daytime.

The heterogeneous surface has an impact on wind speed, wind shear, and the level of atmospheric turbulence (Dörnbrack and Schumann, 1993; Belcher et al., 2003; Bou-Zeid et al., 2004; Millward-Hopkins et al., 2012; Kang et al., 2012; Kang and Lenschow, 2014; Calaf et al., 2014). Figure 4.12 displays vertical profiles of the horizontal averages of the zonal and meridional wind components in *a* and *b* as well as the wind direction in *c* and the total turbulent intensity in *d* after 12 h and 24 h of both idealized ABL simulations for the CBL and the SBL over homogeneous and heterogeneous terrain. In the following, the EBL and the MBL over heterogeneous surface are not discussed. Over homogeneous

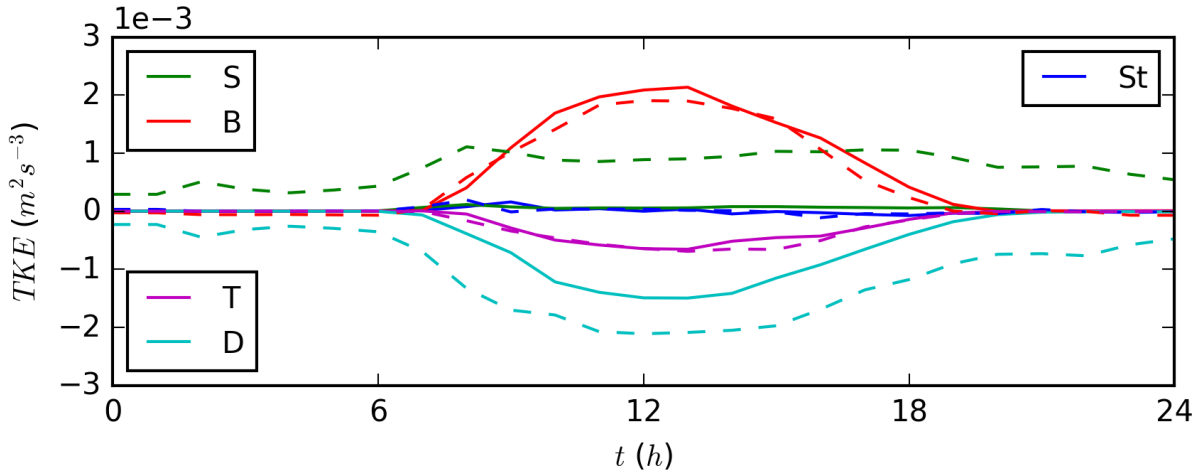

Figure 4.11: Temporal evolution of the TKE budget terms from Eq. 2.21 for the idealized ABL over homogeneous surface as solid lines and for the idealized ABL over heterogeneous surface as dashed lines. S corresponds to shear, B to buoyancy production, T to turbulent transport, D to dissipation, and St to storage.

surface, the results for the MBL are similar to those of the SBL due to the dominant shear effect. The results for the EBL are already influenced by the averaging, which makes an investigation of the general impact of the surface condition rather difficult.

For daytime and nighttime conditions, the horizontally-averaged zonal winds above the heterogeneous surface are smaller than for the homogeneous runs (Fig. 4.12*a*). As expected, they are smaller in SBL_{het} than in CBL_{het} at the rotor levels between 50 m and 150 m altitude. In contrast, the homogeneous simulations produce approximately the same magnitudes for the SBL and the CBL at these heights. Furthermore, the zonal velocity shear at the lower rotor part is less pronounced in SBL_{het} and has nearly the same values across the whole rotor. No significant zonal velocity shear is prevalent in both, CBL and CBL_{het}. The vertical profiles of the meridional velocity components for the homogeneous SBL and CBL cases differ as shown in Fig. 4.12*b*. In contrast, the heterogeneous results show nearly the same magnitude and shape of the v_e-profiles for CBL_{het} and SBL_{het}. Their vertical structure is similar to the well-mixed profiles of a convective boundary layer with nearly vanishing vertical shear at the rotor levels. However, the meridional velocities are significantly higher in both heterogeneous runs in comparison to the homogeneous CBL.

The horizontal averages of the zonal and meridional velocity profiles of both heterogeneous cases result in nearly straight hodographs with minimal directional shear across the rotor levels as shown as dashed lines in Fig. 4.7*b* (CBL_{het} is rather similar to EBL_{het}, which is plotted as counterpart of the EBL, and is therefore not shown in the hodograph). The marginal change in the wind direction with height is also visible in Fig. 4.12*c*: A wind

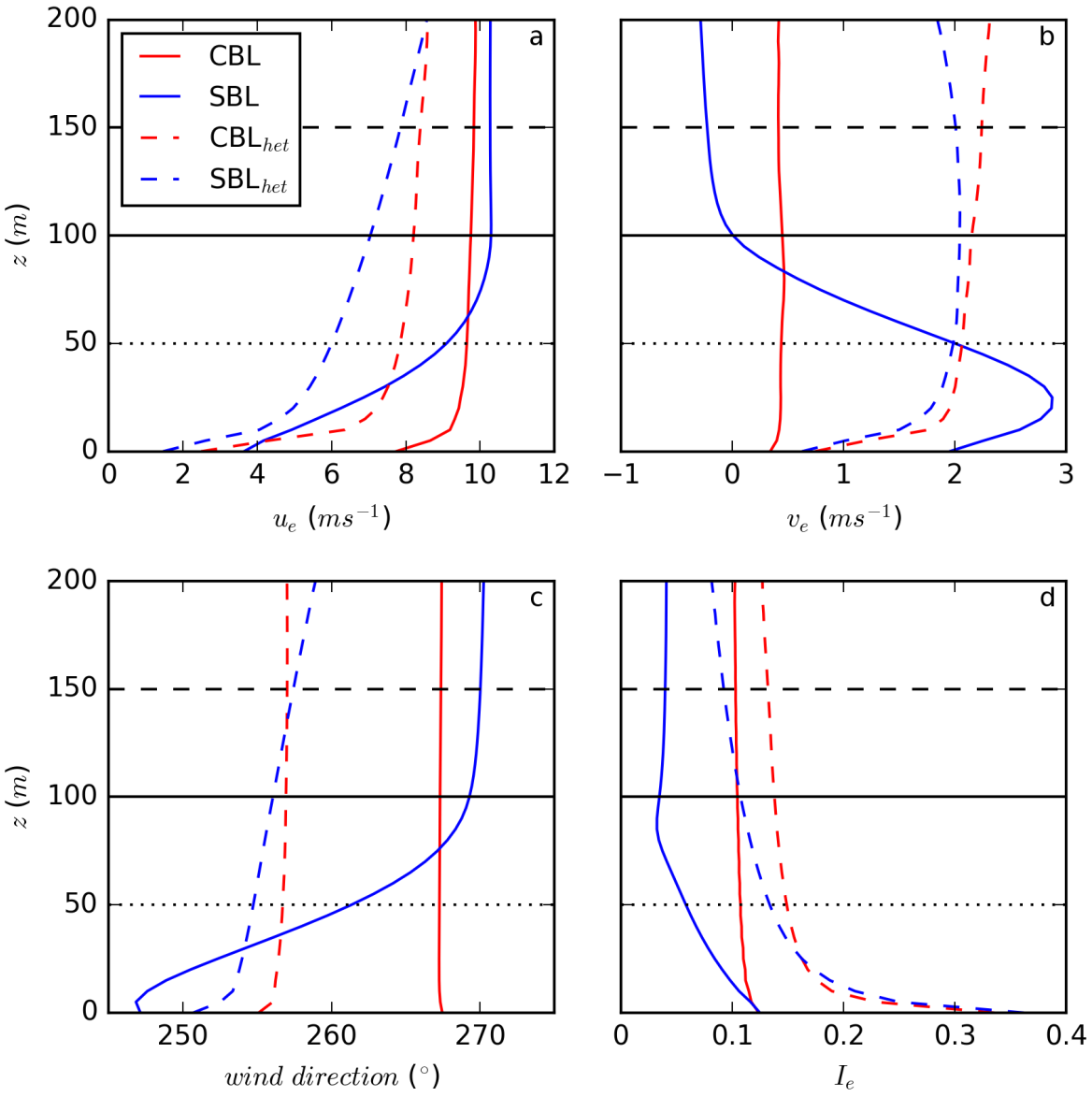

Figure 4.12: Vertical profiles of u, v, the wind direction, and I are shown as horizontal average in a, b, c, and d. The solid red (blue) line corresponds to the CBL (SBL) and the dotted red (blue) line to the CBL$_{het}$ (SBL$_{het}$).

direction difference of 15° towards the south for SBL$_{het}$ in comparison to SBL and of 12° towards the south for CBL$_{het}$ in comparison to CBL exists at hub height.

The enhanced shear produced by the flow over the obstacles results in a much larger total turbulent intensity I_e in the lowest levels for CBL$_{het}$ and SBL$_{het}$ in comparison to CBL and SBL as shown in Fig. 4.12d. The magnitude of the horizontally-averaged total turbulent

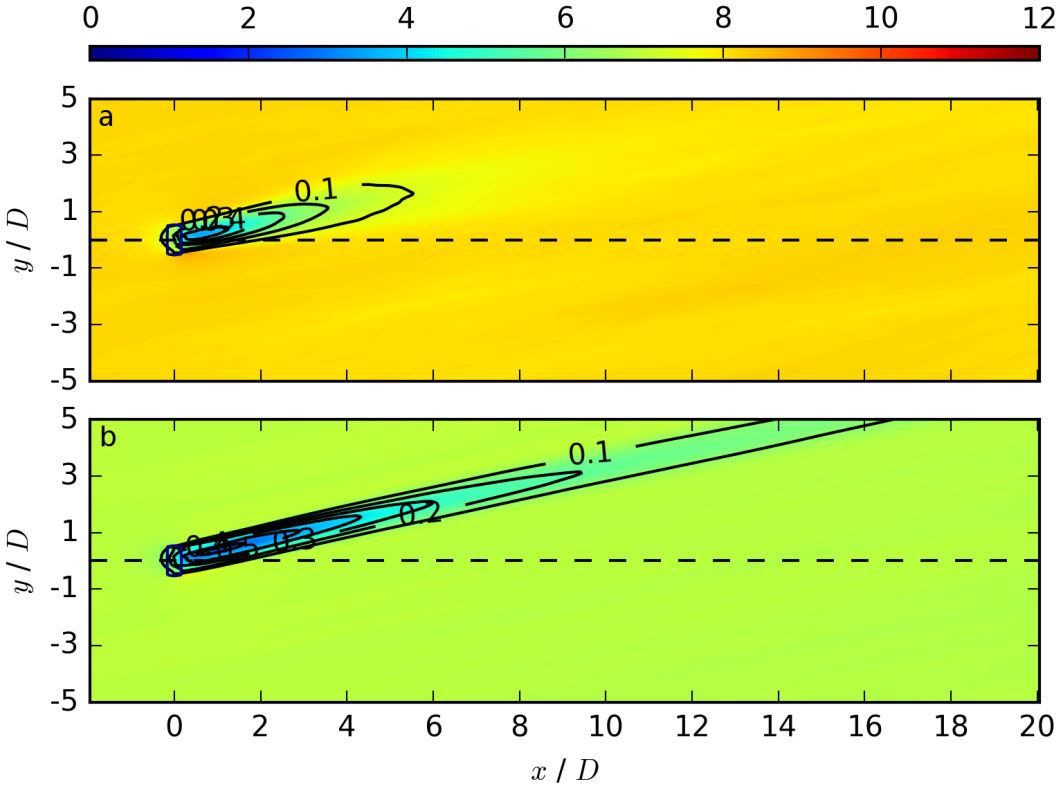

Figure 4.13: Contours of the streamwise velocity $\overline{u_{i,j,k_h}}$ in m s^{-1} at hub height z_h, averaged over the last 50 min, for CBL$_{het}$ in *a* and SBL$_{het}$ in *b*. The black contours represent the velocity deficit VD_{i,j,k_h} at the same vertical location.

intensity is approximately the same for CBL$_{het}$ and SBL$_{het}$ up to a height of roughly 25 m. At the height of the rotor, I_e is larger for CBL$_{het}$ in comparison to SBL$_{het}$ and the values even exceed I_e for the homogeneous CBL. Moreover, I_e in SBL$_{het}$ is approximately five times larger than in the homogeneous SBL. As for the zonal wind component, the vertical gradient of I_e is nearly constant across the rotor levels for SBL$_{het}$ whereas the I_e-profile for the homogeneous SBL run shows pronounced shear across the lower part of the rotor. The differences of I_e between CBL and CBL$_{het}$ and likewise between SBL and SBL$_{het}$ result from the intensified contribution of shear production over the heterogeneous surface (Fig. 4.11), whereas the differences between CBL and SBL and likewise between CBL$_{het}$ and SBL$_{het}$ are related to the buoyancy budget term with a maximum value during the day.

The significantly different profiles of the mean quantities for the heterogeneous cases are caused by the mechanical production of TKE (Fig. 4.11). The enhanced turbulent mixing in the lower part of the ABL compensates the formation of an Ekman spiral in the stably-stratified case (Fig. 4.7*b*). Moreover, the increased turbulence causes nearly similar vertical profiles of the horizontal average of the zonal and meridional wind components, the wind direction, and the total turbulent intensity for SBL$_{het}$ and CBL$_{het}$.

Wind-turbine simulations over heterogeneous surface

The ABL flow fields from the idealized simulation over the heterogeneous surface are used as background profiles and as initial and inflow conditions for the subsequent wind-turbine simulations. The aim is to investigate the wake structure during the day and the night over the heterogeneous terrain and to compare the results to the corresponding homogeneous wind-turbine simulations. The impact on the wake is shown in the x-y cross-sections in Fig. 4.13 for CBL_{het} in a and for SBL_{het} in b. First of all, the upstream values of the streamwise velocity in the CBL_{het} and SBL_{het} runs are smaller in comparison to the results for the homogeneous CBL and SBL runs in Fig. 4.4a and c, as already indicated by Fig. 4.12a. Furthermore, as also indicated by Fig. 4.12a, they are smaller for SBL_{het} in comparison to CBL_{het}.

The maximum velocity deficit is smaller for CBL_{het} (0.4 compared to 0.5 for the homogeneous case) and for SBL_{het} (0.5 compared to 0.7 for the homogeneous case). In accordance with the enhanced turbulence provided by the precursor simulation, the ambient flow recovers more rapidly in both heterogeneous cases whereby the CBL_{het} run shows a shorter downstream wake extension than the SBL_{het} run. Both wakes in Fig. 4.13 are deflected towards the north (wake deflection angle $< 90°$). As the ABL is well mixed at the rotor heights, even at night, the northward deflection occurs at all vertical levels. Similar to the homogeneous runs, the wake deflections coincide with the ambient wind direction averaged over the upstream section of the domain which directly interacts with the wind turbine.

This investigation reveals a profound impact of the surface conditions on the low-level wind and turbulence of the precursor ABL simulations and, therefore, on the resulting wake structures in the wind-turbine simulations. Especially the wake during the nighttime is completely different for heterogeneous surface conditions in comparison to the homogeneous case. As mentioned before, the difference results from the large increase of the shear production term of the TKE budget, which leads to enhanced vertical mixing and compensates the Ekman spiral of the homogeneous SBL. In this work, an upstream region of 300 m is used for the heterogeneous wind-turbine simulations to make them comparable to the homogeneous ones. The impact of the surface condition from the precursor simulation can be less distinct if the upstream region between the obstacles and the wind turbine is increased, however, the impact should not be negligible.

4.4 Summary

The investigation of the impact of the diurnal cycle of the ABL on wind-turbine wakes presents the following results:

The simulation results from the idealized diurnal cycle simulation of the ABL over homogeneous surface reveal a significant effect on low-level wind shear, wind veer, and total turbulent intensity in the lowest 200 m over the course of a day. In particular, the vertical

low-level wind shear is strong in the SBL and in the MBL, whereas it is insignificant in the CBL and in the EBL. The total turbulent intensity is much larger in the CBL and in the EBL in comparison to the SBL and the MBL. During the night an LLJ forms at the height of the wind-turbine rotor and is prevalent in the MBL, resulting in a change of the wind direction with height.

The wakes resulting from the interaction of the time-dependent ABL flow and the wind turbine are strongly influenced by the respective regimes of the ABL evolution. Specifically, the wake recovers more rapidly under convective conditions during the day, compared to at night. The wake characteristics of the transitional periods are strongly influenced by the flow regime prior to the transition. Further, the horizontal wake deflections vary with height in the SBL and in the MBL in response to the change of the upstream wind direction between bottom tip and hub height of the rotor. In the CBL and in the EBL, the wake deflections are also determined by the incoming wind direction, which is, however, constant over the rotor area. The different wake deflections result in a rather compact streamwise and spanwise domain extension during the day and in the evening and a correspondingly larger streamwise and spanwise domain extension during the night and in the morning, to represent the less rapid entrainment and the wake deflection with height. Furthermore, a short temporal averaging period of about 10 min is sufficient for obtaining reliable statistical results for the wind-turbine simulations representing the SBL and the MBL. However, the averaging period for the EBL is strongly affected by the occurrence of thermals, and in the CBL by the temporal meridional wind fluctuations. Furthermore, there is barely seen any difference between the corresponding wake structures throughout two full diurnal cycles.

The main difference of the heterogeneous ABL simulation to the results of the homogeneous ABL simulation is the occurrence of nearly identical low-level wind profiles during the day and the night. They reveal almost no vertical and directional shear of the horizontal wind components across the levels of the wind-turbine rotor. The resulting wakes under convective and stable conditions are very similar to each other regarding the absolute wake deflection and the vertical gradient. During the day, the flow in the wake recovers more rapidly as it was the case for the corresponding homogeneous runs. The simulated wakes produced for the nighttime situation completely differ between heterogeneous and homogeneous surface conditions. The heterogeneous run reveals a less pronounced velocity deficit and the enhanced entrainment, caused by the shear-induced mixing, leads to a more rapid recovery of the ambient flow.

The investigation of the impact of the diurnal cycle of the ABL on wind-turbine wakes constitutes the second step towards an increase of the wind-energy contribution to the primary energy demand. This was extremely important as it demonstrates how a wind-turbine operates under different atmospheric conditions, additionally influenced by different surface conditions. Further, it completes the basic concept, necessary for the development of the numerically efficient parameterization of turbulent wind-turbine flows for LES of different thermal stratifications and it offers wind-turbine simulations necessary to validate the parameterization.

5 A numerically efficient parameterization of turbulent wind-turbine flows for LES of different thermal stratifications

In this chapter, a numerically efficient parameterization of turbulent wind-turbine flows for LES of different thermal stratifications is developed and successfully validated by applying and combining the results of the previous two chapters. The turbulence preserving method is modified to make it appropriate for different thermal stratifications. To achieve this, the turbulence preserving method is extended to a stratification dependent turbulent inflow, and combined with different background wind profiles towards the parameterization, valid under homogeneous surface conditions. The data of both, the stratification dependent turbulent inflow and the background wind profiles, are extracted from the diurnal cycle simulation over homogeneous surface from the previous chapter. Three different levels of complexity are applied as stratification dependent turbulent inflow with the aim of making the diurnal cycle simulation obsolete in the simplest case. The following wind-turbine simulations, performed with the parameterization, are successfully validated against the wind-turbine simulations, which result from the diurnal cycle simulation over homogeneous surface of the previous chapter.

As explained in the Introduction, the development of this parameterization is necessary to offer a simple, numerically efficient, and computationally fast approach, which serves as testbed to investigate the wind-turbine response under different atmospheric conditions.

5.1 Different thermal stratifications

The development of a numerically efficient parameterization of turbulent wind-turbine flows for LES of different thermal stratifications requires an atmospheric NBL regime as well as different representative thermal stratifications occurring during a diurnal cycle. As representations, the NBL simulation from Chapter 2 as well as the diurnal cycle simulation implemented in Chapter 2 and discussed in Chapter 4 are used.

Snapshots of the instantaneous wind fields u, v, and w of the NBL precursor simulation, as well as of the CBL, the EBL, the SBL, and the MBL regime of the idealized diurnal cycle simulation, are presented in Fig. 5.1, with the following characteristics:

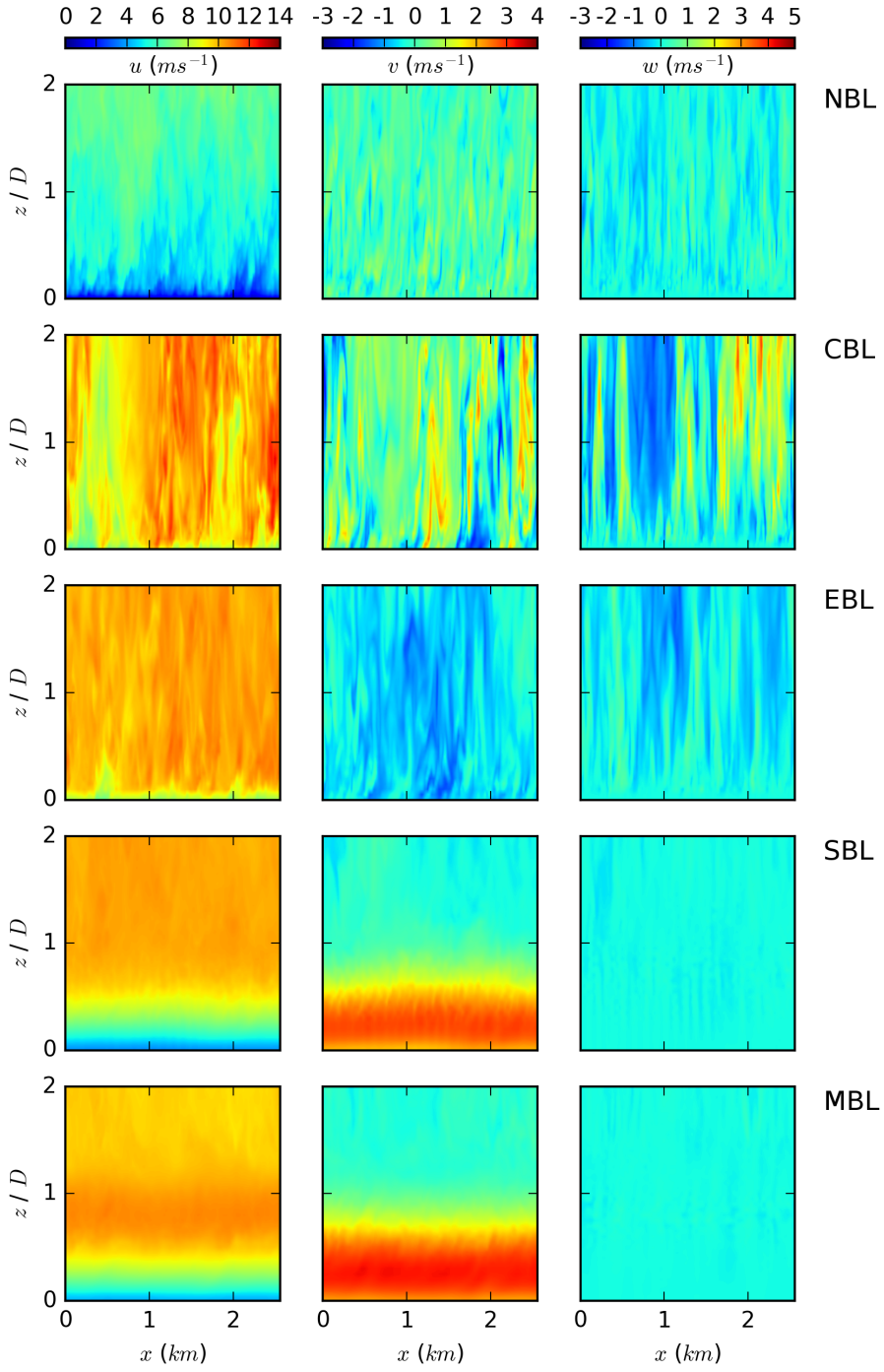

Figure 5.1: Contours of u, v, and w for the NBL equilibrium state (first row) of the precursor simulation, the CBL state at 12 h (second row), the EBL state at 18 h (third row), the SBL state at 24 h (fourth row), and the MBL state at 29 h (fifth row) of the idealized diurnal cycle simulation.

The NBL exhibits a shallow ABL with low vertical wind speeds. In the CBL, the ABL reaches higher altitudes with significant meridional and vertical winds. Further, the turbulence structure consists of larger turbulent eddies in comparison to the other stratifications, which results from the maximum of positive buoyancy, induced by the surface heat flux. In the EBL, the convective updrafts as well as the horizontal wind weakens. In the SBL, an LLJ starts to develop with a wind turning with height and no significant vertical wind. The situation in the MBL is very similar to the SBL, with an intensification of the LLJ.

The horizontal means of the corresponding wind profiles u_e and v_e are shown in Fig. 5.2*a* and *b*. The zonal and meridional background wind fields of the CBL and in the EBL are fundamentally different in comparison to the SBL and the MBL. In the CBL and the EBL, the vertical wind shear of the zonal wind is rather small above the ground, and only small deviations from no meridional wind are prevalent. In the SBL and in the MBL, the vertical wind shear of the zonal and meridional wind is very pronounced, with a supergeostrophic situation prevailing in the MBL. The different profiles of the SBL and the MBL in contrast to the CBL and the EBL are induced by the Coriolis force and its Ekman spiralling, which dominates the buoyancy effects at night. A more detailed description of the background wind profiles is given in Chapter 4 and Figs. 4.2*c* and 4.12*a* and *b*.

This results in two different background wind fields in the proposed parametrization: A daytime representation of the CBL and the EBL profile and a nighttime profile representing the SBL and the MBL. The daytime representation is described by a zonal background wind profile

$$ue(z) = \frac{u_*}{\kappa} \cdot ln(\frac{z}{z_0}), \tag{5.1}$$

with a friction velocity $u_* = 0.35$ m s^{-1}, a von Karman constant $\kappa = 0.4$, a roughness length $z_0 = 0.001$ m, and the meridional background wind profile $ve(z) = 0$. The nighttime representation of the zonal and meridional wind profiles can be expressed with

$$ue(z) = u_g \cdot \left(1 - \exp\left(-\frac{z \cdot \sqrt{f/K_0}}{\sqrt{2}}\right) \cdot \cos\left(\frac{z \cdot \sqrt{f/K_0}}{\sqrt{2}}\right)\right), \tag{5.2}$$

$$ve(z) = u_g \cdot \exp\left(-\frac{z \cdot \sqrt{f/K_0}}{\sqrt{2}}\right) \cdot \sin\left(\frac{z \cdot \sqrt{f/K_0}}{\sqrt{2}}\right). \tag{5.3}$$

They result in the best fit with the SBL and the MBL background wind profiles for $t = 0$, a Coriolis parameter $f = 1.0 \times 10^{-4}$ s^{-1}, a geostrophic wind $u_g = 10$ m s^{-1}, and $v_g = 0$ m s^{-1}, and an eddy viscosity coefficient $K_0 = 0.06$ m^2 s^{-1} according to Shapiro and Fedorovich (2010, Eqs. 36 and 37). The vertical background wind profiles *we* are set to zero for the day and the nighttime representations.

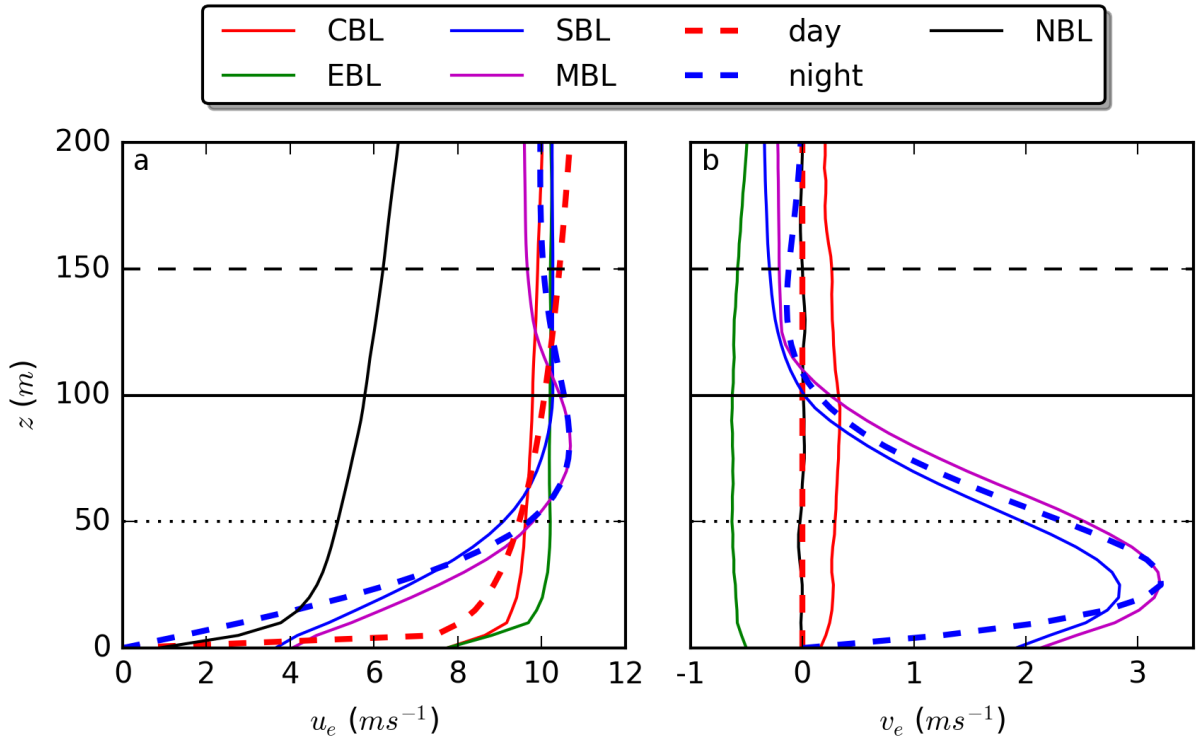

Figure 5.2: Vertical profiles of the horizontal average of the background profiles u_e in a and v_e in b for the NBL, the CBL, the EBL, the SBL, and the MBL precursor simulation. The applied fits for the day and the night are plotted as dashed lines. The hub height (100 m; black solid line), the top tip (150 m; black dashed line) and the bottom tip (50 m; black dotted line) region of a wind turbine with $D = 100$ m and $z_h = 100$ m are highlighted by horizontal lines.

5.2 Stratification dependent turbulent inflow

For the stratification dependent turbulent inflow, a modified version of the turbulence preserving method in Eq. 2.18 is used. The version of the turbulence preserving method from Chapter 2 is therefore hereafter referred to as original version of the turbulence preserving method.

A comparison of the streamwise velocity ratio VR_{i,j_0,k_h} and the total turbulent intensity I_{i,j_0,k_h} between wind-turbine simulations performed with the original version of the turbulence preserving method for $\alpha = 1$ (B_1), $\alpha = 5$ (B_5), and $\alpha = 10$ (B_10) in Figs. 3.4a and 3.5a and synchronized diurnal cycle wind-turbine simulations for the CBL, the EBL, the SBL, and the MBL regime from Figs. 4.3 and 4.4.

The velocity ratio resulting from the original version of the turbulence preserving method is comparable to the values of the SBL and the MBL wind-turbine simulations B_1 for $\alpha = 1$. For $\alpha = 5$, the values of B_5 are comparable to the EBL wind-turbine simulation and for $\alpha = 10$ (B_10) to the CBL wind-turbine simulation. The $VR_{i,j_0,k}$ - gradient of the wake

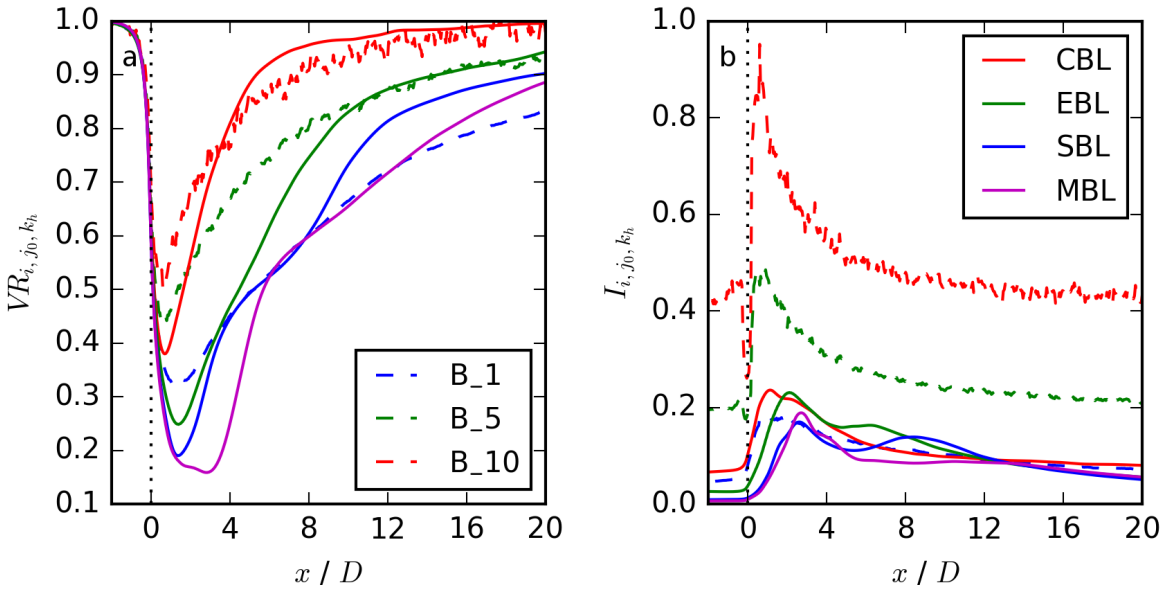

Figure 5.3: A comparison of the dependency of the streamwise velocity ratio VR_{i,j_0,k_h} in a, and the total turbulent intensity I_{i,j_0,k_h} in b between the wind-turbine simulations performed with the original version of the turbulence preserving model for $\alpha = 1$ (B_1), $\alpha = 5$ (B_5), and $\alpha = 10$ (B_10), and the CBL, the EBL, the SBL, and the MBL situation.

recovery is only slightly smaller. The total turbulent intensity values are comparable for $\alpha = 1$. However, for $\alpha = 5$ and $\alpha = 10$ they are too large in comparison to all synchronized diurnal cycle wind-turbine simulations.

Various tests studying the sensitivity of the numerical results to the choice of $\alpha \cdot \beta$ revealed that the random number β, impressed at every time step in the whole domain, destroys the NBL turbulence structure in II. This problem could be solved by eliminating β. It results in a more rapid wake recovery and smaller values of the streamwise turbulent intensity for increasing α. In addition, the factor α from Eq. 2.18 has been adapted in the modified version of the turbulence preserving method: An adjustable value α_0 is applied, which is required for a comparison between the synchronized diurnal cycle wind-turbine simulations and the wind-turbine simulations performed in this chapter. In more general applications of this apporach, α_0 can be set to 1. Further stratification related parameters $\boldsymbol{\alpha}_{i,j,k}$ are applied, which represent the velocity perturbations, to account for the different atmospheric regimes during the diurnal cycle. They are extracted from the corresponding situation of the idealized first day of the diurnal cycle simulation over homogeneous surface. This results in a modification of the turbulence preserving method from Eq. 2.18

$$\mathbf{u}_p^*\big|_{i_1,j,k}^{\xi} = \alpha_0 \cdot \boldsymbol{\alpha}_{i^*,j,k} \cdot \left(\mathbf{u}_p\big|_{i^*,j,k} - \frac{1}{n \cdot m} \sum_{i=1}^{n} \sum_{j=1}^{m} \mathbf{u}_p\big|_{i,j,k} \right). \tag{5.4}$$

The term in the brackets of Eq. 5.4 corresponds to II in Eq. 2.18. However, the perturbation velocities $\mathbf{u}_p^*\big|_{i_1,j,k}^{\xi}$ contribute only to the first grid point in x-direction. This modification was necessary, as a permanent impressing of the perturbation velocities in the whole domain resulted in large positive and negative tendencies, which were compensated in Eq. 2.18 by the randomness of β.

Three sets of functions are applied as adjustable stratification related parameters for $\boldsymbol{\alpha}_{i^*,j,k}$, representing different levels of complexity: Function set A uses three 3 D matrices for the three wind components, function set B uses three 1 D vectors for each of the wind components, and, finally, function set C uses only three scalar values to modify u, v, and w, respectively.

A: $\boldsymbol{\alpha}_{i^*,j,k}$ corresponds to three 3 D matrices for each wind component, resulting in:

$$\boldsymbol{\alpha}_{i^*,j,k} = \frac{1}{3} \cdot (\mathbf{u}_{\alpha_{i^*}} + \mathbf{u}_{\alpha_j} + \mathbf{u}_{\alpha_k}), \tag{5.5}$$

defined as

$$\mathbf{u}_{\alpha_i^*} \equiv \frac{\max(\mathbf{u}_{dc_{i,1:m,1:l}}) - \min(\mathbf{u}_{dc_{i,1:m,1:l}})}{\max(\mathbf{u}_{NBL_{i,1:m,1:l}}) - \min(\mathbf{u}_{NBL_{i,1:m,1:l}})}, \tag{5.6}$$

$$\mathbf{u}_{\alpha_j} \equiv \frac{\max(\mathbf{u}_{dc_{1:n,j,1:l}}) - \min(\mathbf{u}_{dc_{1:n,j,1:l}})}{\max(\mathbf{u}_{NBL_{1:n,j,1:l}}) - \min(\mathbf{u}_{NBL_{1:n,j,1:l}})}, \tag{5.7}$$

$$\mathbf{u}_{\alpha_k} \equiv \frac{\max(\mathbf{u}_{dc_{1:n,1:m,k}}) - \min(\mathbf{u}_{dc_{1:n,1:m,k}})}{\max(\mathbf{u}_{NBL_{1:n,1:m,k}}) - \min(\mathbf{u}_{NBL_{1:n,1:m,k}})}. \tag{5.8}$$

Here, $\mathbf{u}_{dc_{i,j,k}}$ are the corresponding 3 D wind fields of the CBL, the EBL, the SBL, or the MBL, extracted from the diurnal cycle precursor simulation, whereas $\mathbf{u}_{NBL_{i,j,k}}$ corresponds to the equilibrium state of the NBL precursor simulation. The differences in the numerator as well as in the denominator correspond to the maximum of the fluctuations in the corresponding atmospheric state. The maximum of the fluctuations of the NBL state is used for the normalization. This is motivated by II in Eq. 5.4, which also corresponds to the NBL situation. Therefore, the 1 D vectors in Eqs. 5.6 - 5.8 include the spatial structure and the normalized turbulence.

B: $\boldsymbol{\alpha}_{i^*,j,k}$ corresponds to three vertical 1 D vectors for the three wind components, resulting in:

$$\boldsymbol{\alpha}_{i^*,j,k} = \mathbf{u}_{\alpha_k} \tag{5.9}$$

C: One value for all three wind components, resulting in α_u, α_v, and α_w. The values are an approximation taken at 100 m, which corresponds to the hub height of a common wind turbine.

The vertical profiles of $\boldsymbol{\alpha}_{i^*,j,k}$ for different thermal stratifications for function set type B are shown in Fig. 5.4 together with the horizontally-averaged fluctuations of u, v, and w for the NBL, the CBL, the EBL, the SBL, and the MBL. The fluctuations contribute to the nominator as well as to the denominator of Eqs. 5.8. They are very small for the SBL and the MBL situation, increase in the EBL, and are largest in the CBL. More precisely, they increase by a factor of eight from the SBL and the MBL to the EBL and by a factor of three from the EBL to the CBL, whereas the amount of NBL fluctuations correspond most closely to the EBL situation for all three wind components. Therefore, the values of u_{α_k}, v_{α_k}, and w_{α_k} are roughly one in the EBL. During the day (night), they are larger (smaller) in comparison to the transitional state, resulting from a larger (smaller) numerator in comparison to the denominator in Eq. 5.8. Further, the values α_u, α_v, and α_w of function set type C result from u_{α_k}, v_{α_k}, and w_{α_k} of function set type B at a height of 100 m. They are listed in Table 5.1 for all three regimes.

Due to this same-sized fluctuations and stratification related weighting values of function set type B in the SBL and in the MBL and the rather similar u, v, and w structures in Fig. 5.1, all wind-turbine simulation characteristics are rather similar for the SBL and the MBL and are, therefore, only discussed for the SBL case in the following.

Therefore, the investigation results in a classification into three regimes with two different background wind fields:

- A daytime situation, which is prescribed by a logarithmic background wind profile (Eq. 5.1) with relatively large wind fluctuations.
- A nighttime situation, which is prescribed by a background wind profile with a wind direction change with height (Eqs. 5.2 and 5.3) and very small wind fluctuations.
- A transition between the daytime and the nighttime situation, which is prescribed by the same logarithmic background wind profile (Eq. 5.1) as the daytime situation, however, characterized by smaller (larger) wind fluctuations in comparison to the day (night).

This parameterization proposed in this thesis is tested in the following wind-turbine simulations for these three regimes of the daytime, the nighttime, and the transition.

The reference and the parametrization wind-turbine simulations consider the temporal fluctuations only in the wind field. No potential temperature deviations from the prescribed background profile $\Theta(z) = 300$ K are considered during the 1 h wind-turbine simulation. This will be explained in more detail the following.

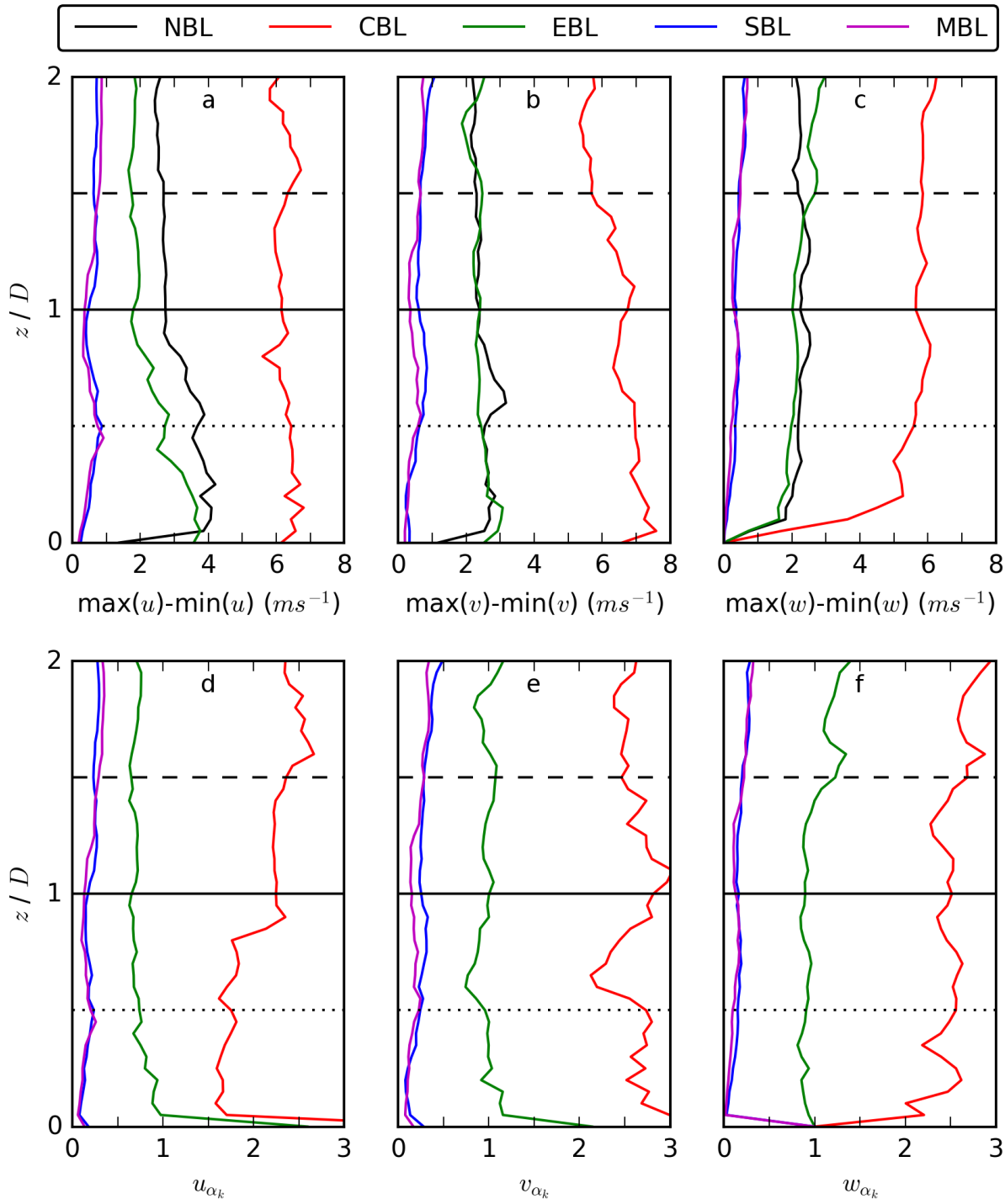

Figure 5.4: Vertical profiles of the maximum of the difference of u in a, v in b, and w in c, calculated as $\max(\mathbf{u}_{NBL_{1:n,1:m,k}}) - \min(\mathbf{u}_{NBL_{1:n,1:m,k}})$ for the NBL and $\max(\mathbf{u}_{dc_{1:n,1:m,k}}) - \min(\mathbf{u}_{dc_{1:n,1:m,k}})$ for the CBL, the EBL, the SBL, and the MBL situations. Vertical profiles of $\boldsymbol{\alpha}_{i^*,j,k}$ are presented for u_{α_k} in d, v_{α_k} in e, and w_{α_k} in f of type B calculated with Eq. 5.8 for the CBL, the EBL, the SBL, and the MBL situation.

Table 5.1: List of the applied background wind profiles u_e, v_e, and w_e as well as the values α_u, α_v, and α_w, used for the wind-turbine simulations representing the daytime, the transition, and the nighttime situation.

state	day	transition	night
u_e	Eq. 5.1	Eq. 5.1	Eq. 5.2
v_e	0	0	Eq. 5.3
w_e	0	0	0
α_u	2.5	0.6	0.15
α_v	2.8	1.0	0.24
α_w	2.5	0.9	0.13

Table 5.2: Summary of the main characteristics of the performed wind-turbine simulations of Chapter 5.

wind-turbine simulation type	benchmark simulation	reference simulation	parameterization simulation
parameterization	no	yes	yes
precursor simulation	CBL, EBL, SBL	CBL, EBL, SBL	NBL
coupling method	synchronized diurnal cycle state	12 h, 18 h, 24 h diurnal cycle state	equilibrium state

5.3 Numerical Experiments

Three types of wind-turbine simulations are considered in this chapter, with a schematic illustration in Fig. 5.5 and their main characteristics summarized in Table 5.2. A detailed description is given in the following:

Benchmark wind-turbine simulations

The benchmark wind-turbine simulations correspond to the synchronized diurnal cycle wind-turbine simulations over homogeneous surface. The CBL, the EBL, and the SBL wind-turbine simulations are used as representatives for the daytime, the transition, and the nighttime regime. For the synchronized coupling between the diurnal cycle precursor simulation and the wind-turbine simulations, the background fields $\psi_e(t) = (u_e(t), v_e(t), w_e(t), \Theta_e(t))$ with $u_e(t) = < u(t) >_z$, $v_e(t) = < v(t) >_z$, $w_e(t) = < w(t) >_z$, and $\Theta_e(t) = \Theta_e(t = 0 \text{ h}) + < \Theta'(t) >_z$, the initial fields, and the inflow data of all prognostic variables $\psi(t) = (u(t), v(t), w(t), \Theta'(t))$ are taken from the idealised ABL simulation of the diurnal cycle after 12 h for the CBL, 18 h for the EBL, and 24 h for the SBL regime. The

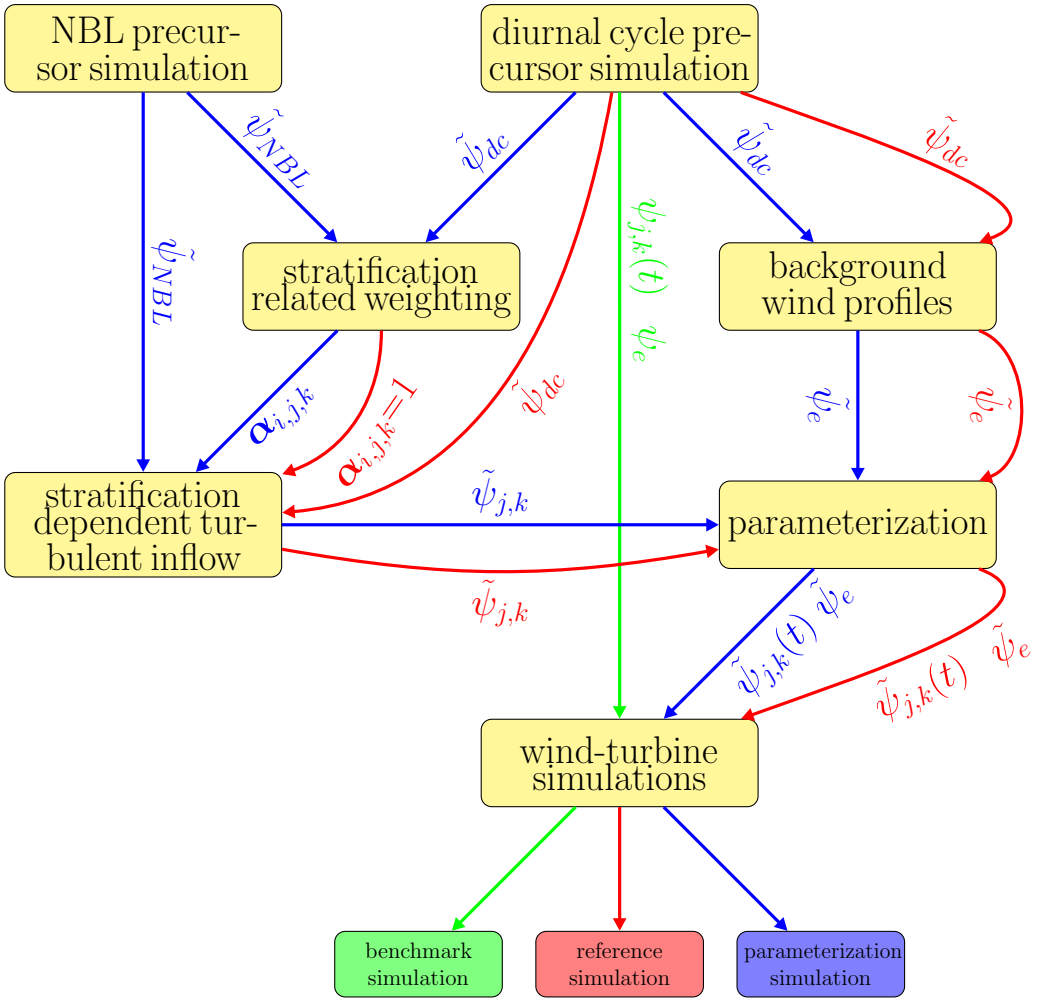

Figure 5.5: Schematic of benchmark, reference, and parameterization wind-turbine simulations input, with $\psi = (u, v, w, \Theta')$, $\psi = (u_e, v_e, w_e, \Theta_e)$, $\tilde{\psi} = (u, v, w)$, and $\tilde{\psi}_e = (u_e, v_e, w_e)$.

horizontal averages of the initial conditions are taken as background profiles, as denoted by $<>_z$. Due to the open streamwise boundary condition, the wind-turbine simulation has to be fed continuously with inflow data from the idealised ABL precursor simulation. The inflow data are taken as 2 D y-z slices $\psi_{j,k}(t)$ at $i = \mathrm{n}$ of ψ from the diurnal cycle simulation at each time step for 1 h time intervals from 12 h to 13 h for the CBL, from 18 h to 19 h for the EBL, and from 24 h to 25 h for the SBL, to ensure synchronized wind-turbine simulations. In the corresponding synchronized timestep of the benchmark wind-turbine simulation, $\psi_{j,k}(t)$ represents the upstream values of ψ at $i = 1$. This process is described in detail in Chapter 2.

Only the spanwise position j of the ABL precursor simulation ($\psi(t)_{j_1 \le j \le j_2}$), which interacts with the wind turbine, differs in these benchmark wind-turbine simulations ($j_1 = 22$; $j_2 = 42$) from the ones in Fig. 4.3 and 4.4 ($j_1 = 246$; $j_2 = 266$). This difference is related to the use of another lateral sector $j_1 \le j \le j_2$ of the ABL simulation, which is applied in the

corresponding wind-turbine simulation. In the wind-turbine simulations of Chapter 4, the wind turbine is located in the lateral domain center ($m = 512$), whereas in the benchmark wind-turbine simulations shown in this chapter, the wind turbine is located at $j = 32$, corresponding to the domain center in the following parametrization and reference wind-turbine simulations performed on 64 grid points in spanwise direction with open spanwise boundary conditions. Both benchmark wind-turbine simulations (Chapter 4 and 5) are performed on 512 spanwise grid points with periodic spanwise boundary conditions. The resulting deviations of the wake deflection and the entrainment rate between these two types of benchmark wind-turbine simulations are negligibly small.

Parameterization wind-turbine simulations

The wind-turbine simulations performed with the proposed parameterization for the daytime, the transitional, and the nighttime situation, are referred to hereafter as parametrization wind-turbine simulations of type A, B, and C. They correspond to the three sets of functions A, B, and C for $\boldsymbol{\alpha}_{i^*,j,k}$ (Eq. 5.5). A schematic illustration of the procedure is given in Fig. 5.5.

A fit to the horizontal average of the atmospheric state of the diurnal cycle simulation $\tilde{\psi}(t) = (u(t), v(t), w(t))$ is applied for the background wind profiles $\tilde{\psi}_e(t) = (u_e(t), v_e(t), w_e(t))$. The CBL regime at 12 h and the EBL regime at 18 h result in a logarithmic zonal background wind profile (Eq. 5.1) and no meridional and vertical background wind. For the SBL, the atmospheric state after 24 h is considered, resulting in a wind direction change with height of the horizontal background wind profiles (Eqs. 5.2 and 5.3). All applied wind profiles, which contribute to the parameterization, are listed in Table 5.1. In addition to the background wind profiles, $\Theta_e(z) = 300$ K at all times and in all heights. In contrast to the benchmark wind-turbine simulations, no inflow data of the prognostic variables $\psi(t) = (u(t), v(t), w(t), \Theta'(t))$ are applied as 2 D y - z slices at each time step, instead, $\tilde{\psi}_{i=1,j,k}(t) = \mathbf{u}_p^*|_{i=1,j,k}^{\xi}$ is modified by the use of the turbulence preserving method following Eq. 5.4. This implies a consideration of the fluctuations only in the wind field, no potential temperature deviations from Θ_e are considered during the 1 h wind-turbine simulation.

Further, the stratification related weighting $\boldsymbol{\alpha}_{i^*,j,k}$ is calculated with $\tilde{\psi}_{NBL}$ of the NBL precursor simulation and $\tilde{\psi}_{dc}$ of the corresponding regime of the diurnal cycle as three 3 D matrices for parameterization type A, three 1 D vectors for parameterization type B, or three values for parameterization type C. The 12 h regime is used for the daytime, the 18 h regime for the transitional, and the 24 h regime for the nighttime representative (Eqs. 5.6 - 5.8).

The resulting stratification related weighting $\boldsymbol{\alpha}_{i^*,j,k}$ and the wind conditions $\tilde{\psi}_{NBL}$ of the NBL equilibrium state contribute to the calculation of the stratification dependent turbulent inflow in Eq. 5.4 with $\alpha_0 = 0.5$. The value of α_0 is motivated later on.

The stratification dependent turbulent inflow $\tilde{\psi}_{j,k}$ and the background profiles $\tilde{\psi}_e$ represent the parameterization and contribute to the parameterization wind-turbine simulations.

Reference wind-turbine simulations

The parameterization wind-turbine simulations consider $\tilde{\psi}_{dc}$ as well as $\tilde{\psi}_{NBL}$. The contribution of $\tilde{\psi}_{NBL}$ in combination with $\boldsymbol{\alpha}_{i^*,j,k}$ is the general idea of the parameterization. The benchmark wind-turbine simulations consider $\psi_{j,k}(t)$ of the diurnal cycle without applying the parameterization. Therefore, to examine the applicability of $\tilde{\psi}_{NBL}$ and $\boldsymbol{\alpha}_{i^*,j,k}$, reference wind-turbine simulations are required.

They apply the parameterization, however, without including the NBL precursor simulation. Instead, the stratification dependent inflow in Eq. 5.4 uses $\tilde{\psi}_{dc}$ together with a stratification related weighting of 1 and $\alpha_0 = 0.5$, as in the parameterization wind-turbine simulations. This procedure is schematically shown in Fig. 5.5.

These reference wind-turbine simulations serve as simplification of the benchmark wind-turbine simulations with the following limitations: They consider only one physical point of time of the diurnal cycle precursor simulation (12 h for the day, 18 h for the transition, 24 h for the night) instead of the 1-h evolution of the atmospheric state (12 h - 13 h for the day, 18 h - 19 h for the transition, 24 h - 25 h for the night). Further, they do not include Θ, resulting in $\tilde{\psi}$ and $\tilde{\psi}_e$ instead of ψ and ψ_e. In addition, the background wind profiles are not the horizontal averages of the diurnal cycle precursor simulation, instead, the fitted profiles from Table 5.1 and Fig. 5.2 are applied. The Θ_e profile is constant with height at 300 K. The reference wind-turbine simulations represent an intermediate step towards the parameterization wind-turbine simulations, which in addition include the NBL precursor simulation contribution to the stratification related weighting and to the stratification dependent turbulent inflow.

Additional remarks on the simulations

In the following, further general remarks on the numerical experiments are given:

- The parameterization and the reference wind-turbine simulations, both performed with the stratification dependent turbulent inflow from Eq. 5.4, are implemented with $\alpha_0 = 0.5$, as stated before. This value results in a slightly less (more) rapid wake recovery of the reference wind-turbine simulation in comparison to the benchmark wind-turbine simulation of the CBL (SBL). The best fit of the reference wind-turbine simulation with the benchmark wind-turbine simulation is achieved for $\alpha_0 = 0.7$ in the CBL, for $\alpha_0 = 0.5$ in the EBL, and for $\alpha_0 = 0.3$ in the SBL. Taking this into account, the following reference wind-turbine simulations and the parameterization wind-turbine simulations of type A, B, and C are performed with $\alpha_0 = 0.5$, as this value results on average over all three regimes in the best fit of the wake structure of the reference wind-turbine simulation with the corresponding benchmark wind-turbine simulation.

- Daytime parameterization wind-turbine simulations of type A, B, and C are further modified by applying the same perturbation velocities $\mathbf{u}_p^*\big|_{i_1,j,k}^{\xi}$ (Eq. 5.4) for three time steps. This is used as a simple approach to mimic the larger turbulent eddies prevalent in the CBL. The resulting entrainment process results in a better agreement of parameterization wind-turbine simulations of type A, B, and C with the corresponding reference wind-turbine simulations. This modification is only applied in the daytime parameterization wind-turbine simulations, not in the transitional and stable simulations.

5.4 Results

In the following, the three types of wind-turbine simulations (benchmark, reference, parameterization) are investigated in detail for the three ABL regimes (daytime, transition, nighttime) to verify the applicability of the parameterization for different thermal stratifications.

The streamwise velocity of the benchmark wind-turbine simulations (in a), the reference wind-turbine simulations (in b), and the parameterization wind-turbine simulations of type A (in c), B (in d), and C (in e) are displayed in the x-z plane in Figs. 5.6, 5.8, and 5.10 and in the x-y plane in Figs. 5.7, 5.9, and 5.11. Figures 5.6 and 5.7 represent the daytime ABL regime, Figs. 5.8 and 5.9 the ABL of the transitional state, and Figs. 5.10 and 5.11 the nighttime ABL regime.

The general wake structure of the simulated streamwise velocity of all simulations in Figs. $5.6 - 5.11$ reveals a deceleration of the flow right behind the rotor with a velocity increase in radial and streamwise directions, resulting from the entrainment of air with higher velocity values from the surrounding. The upstream region differs for the CBL and the EBL in comparison to the SBL and the MBL. This is caused by the difference in the zonal upstream velocity profile in Fig. 5.2a. A more detailed discussion of the wake structure differences for the different atmospheric regimes were presented in Chapter 4. In the following, all wind-turbine simulations corresponding to the same regime are compared.

Benchmark and reference wind-turbine simulations

As first step, the reference wind-turbine simulations are compared to the benchmark wind-turbine simulations, to investigate the impact of the simplifications. The wake structures between the reference and the benchmark wind-turbine simulations are quantitatively consistent. Especially for the transitional state, the agreement between the benchmark and the reference wind-turbine simulations is very good, whereas the wake recovers less rapidly during the day and more rapidly during the night. Further, there are differences in the wake deflection angle. These differences can be attributed to the simplifications.

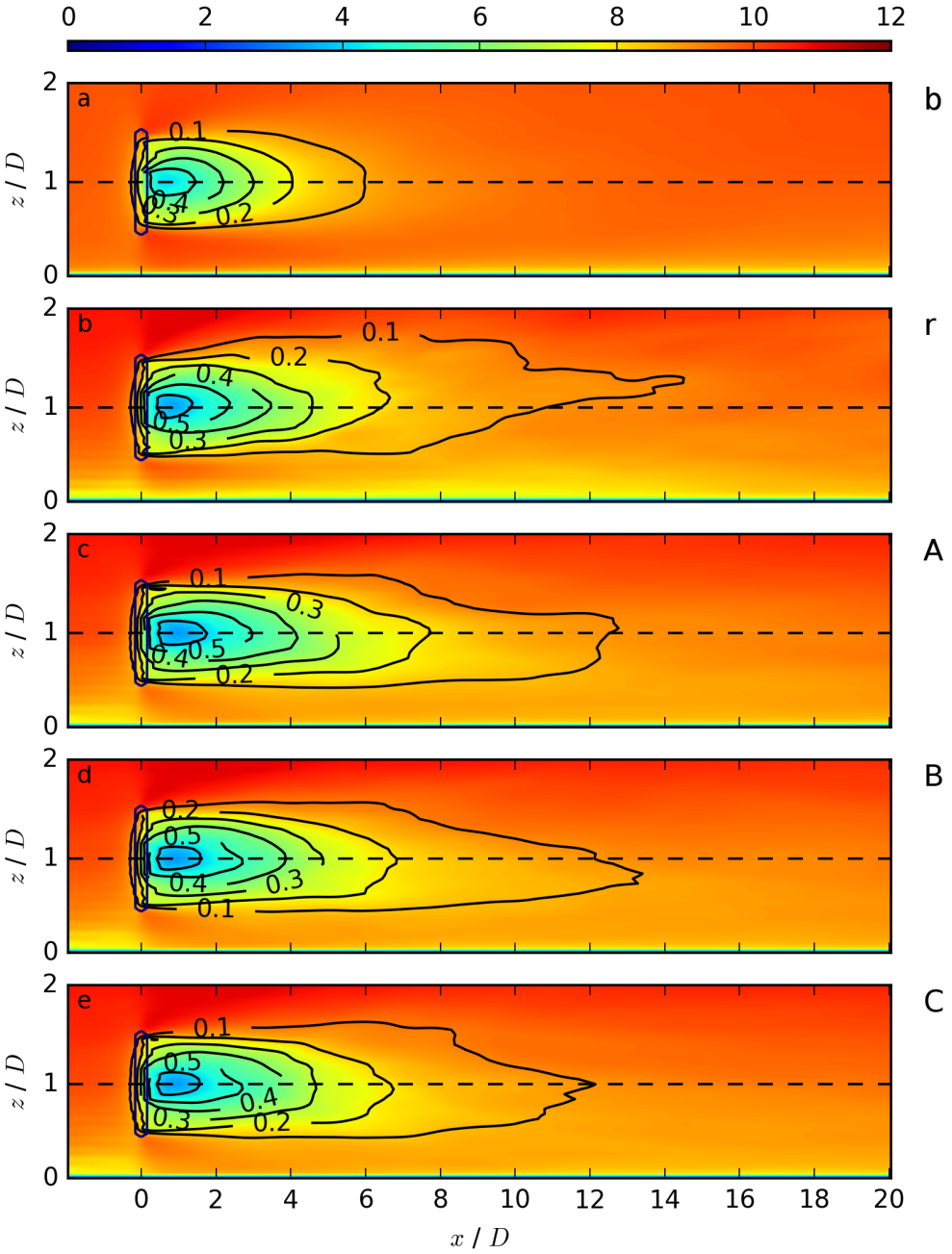

Figure 5.6: Daytime vertical cross sections of $\overline{u_{i,j_0,k}}$ in m s^{-1} for the benchmark wind-turbine simulation in *a*, the reference wind-turbine simulation in *b* and parameterization wind-turbine simulations of type *A*, *B*, and *C* in *c*, *d*, and *e* respectively. The black contours represent $VD_{i,j_0,k}$.

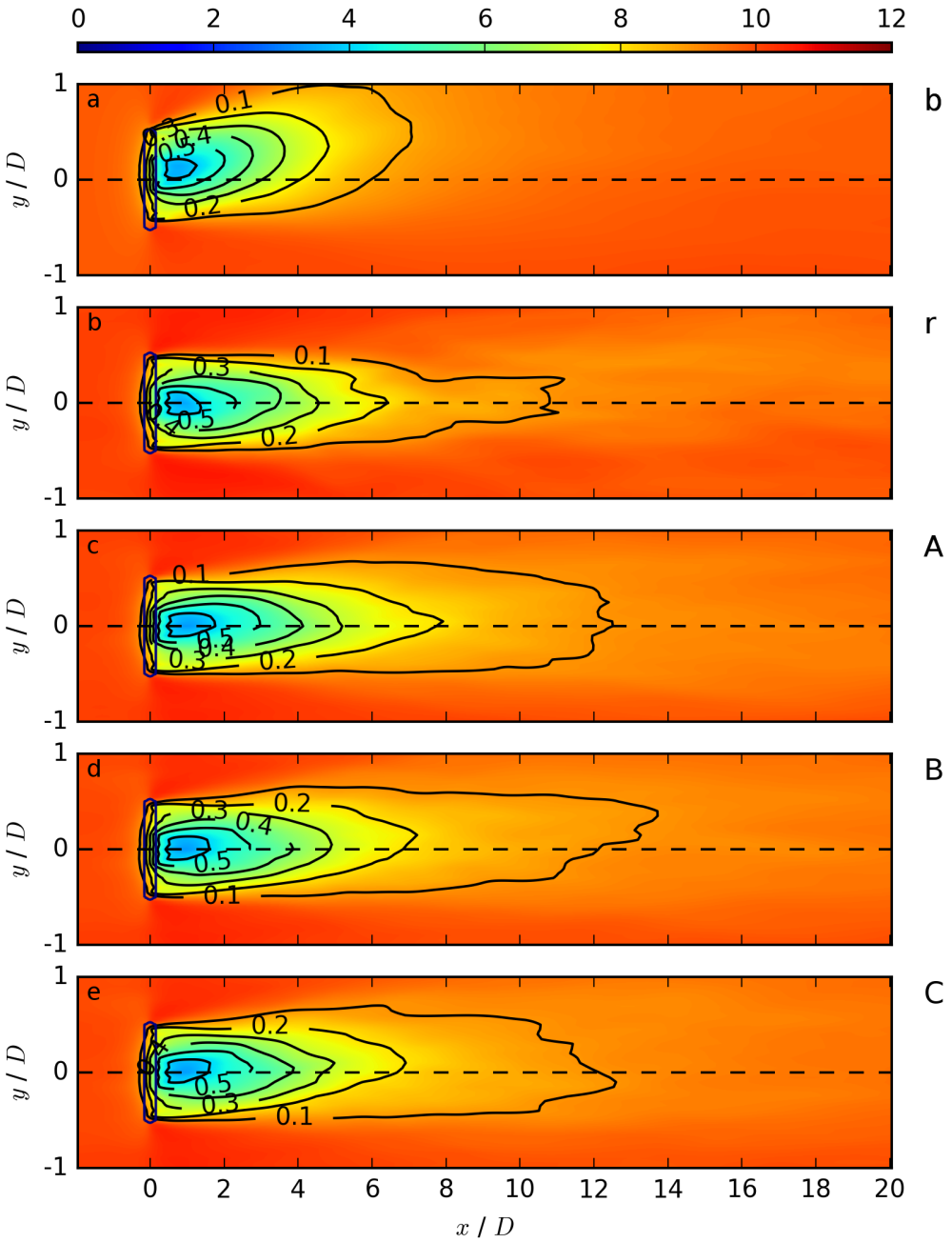

Figure 5.7: Daytime horizontal cross sections of $\overline{u_{i,j,k_h}}$ in m s^{-1} for the benchmark wind-turbine simulation in a, the reference wind-turbine simulation in b and parameterization wind-turbine simulations of type A, B, and C in c, d, and e respectively. The black contours represent VD_{i,j,k_h}.

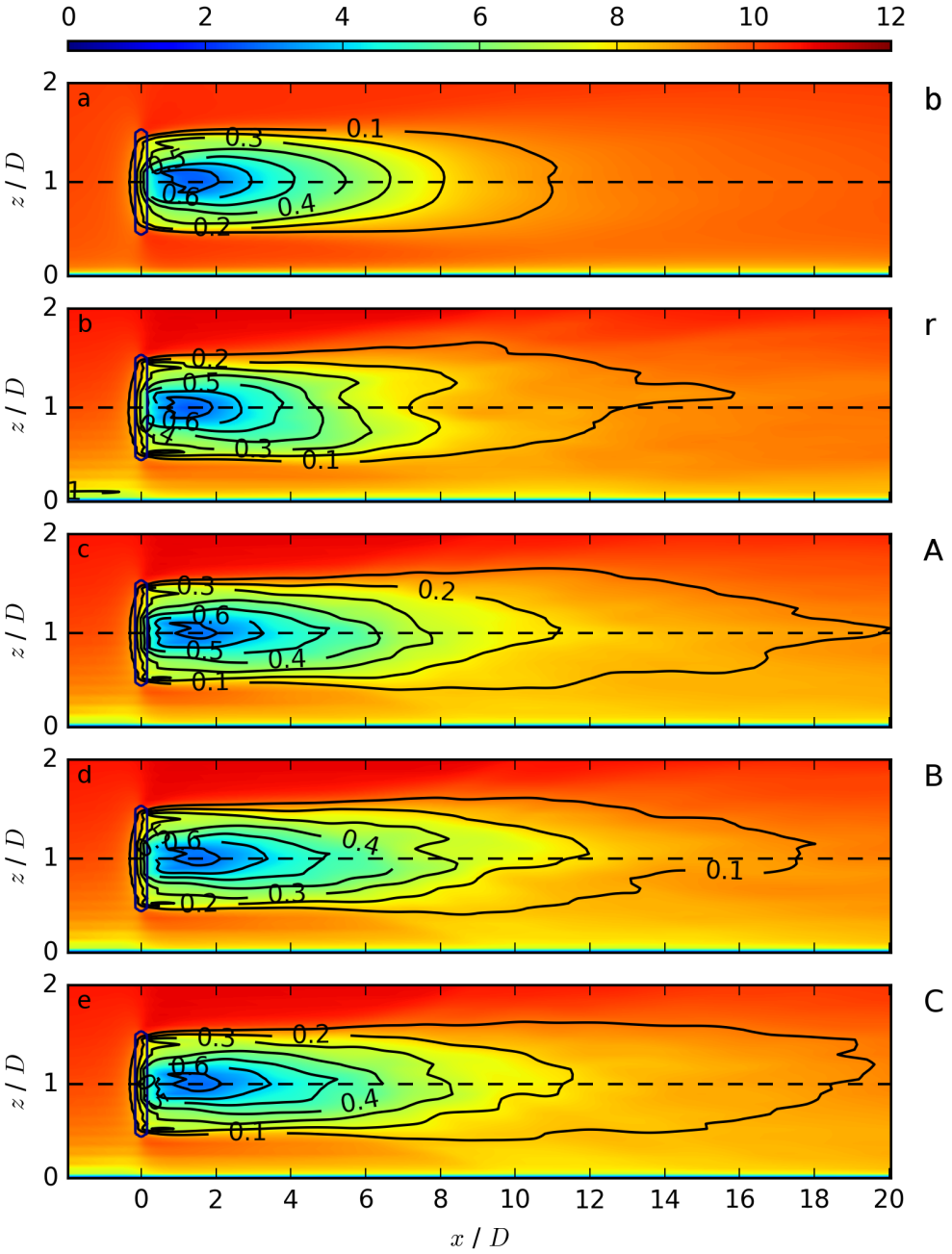

Figure 5.8: Transitional vertical cross sections of $\overline{u_{i,j_0,k}}$ in m s^{-1} for the benchmark wind-turbine simulation in a, the reference wind-turbine simulation in b and parameterization wind-turbine simulations of type A, B, and C in c, d, and e respectively. The black contours represent $VD_{i,j_0,k}$.

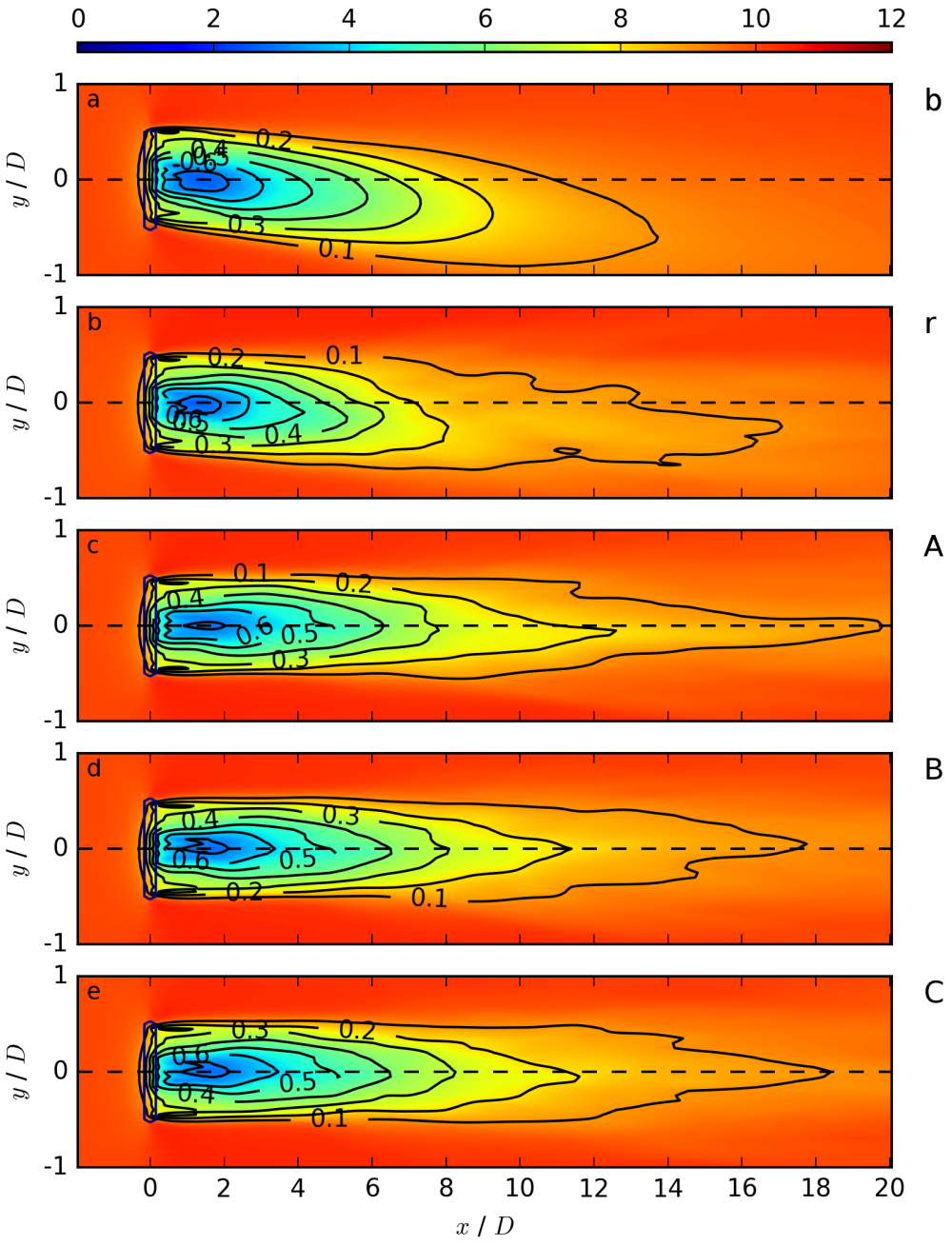

Figure 5.9: Transitional horizontal cross sections of $\overline{u_{i,j,k_h}}$ in m s^{-1} for the benchmark wind-turbine simulation in a, the reference wind-turbine simulation in b and parameterization wind-turbine simulations of type A, B, and C in c, d, and e respectively. The black contours represent VD_{i,j,k_h}.

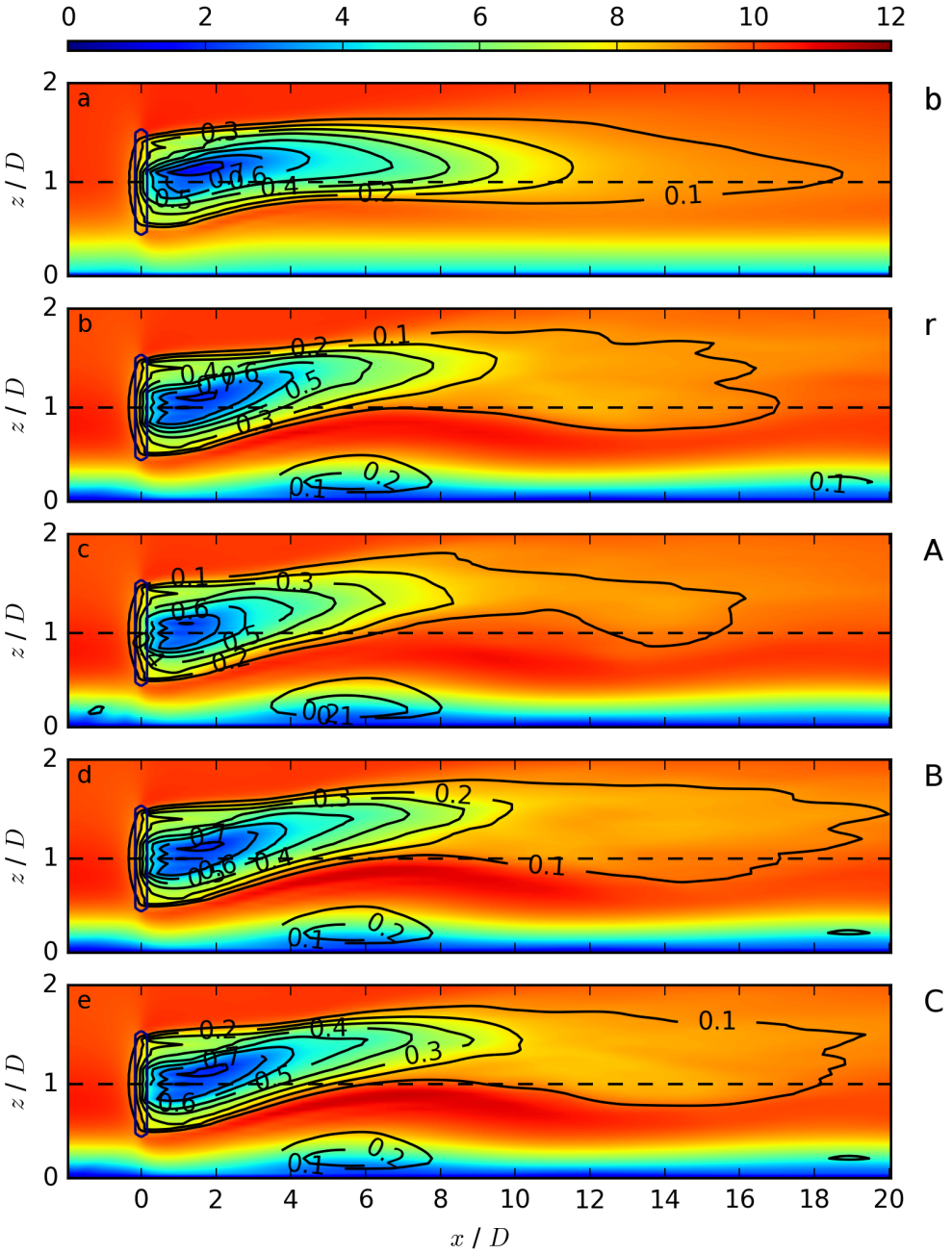

Figure 5.10: Nighttime vertical cross sections of $\overline{u_{i,j_0,k}}$ in m s^{-1} for the benchmark wind-turbine simulation in *a*, the reference wind-turbine simulation in *b* and parameterization wind-turbine simulations of type *A*, *B*, and *C* in *c*, *d*, and *e* respectively. The black contours represent $VD_{i,j_0,k}$.

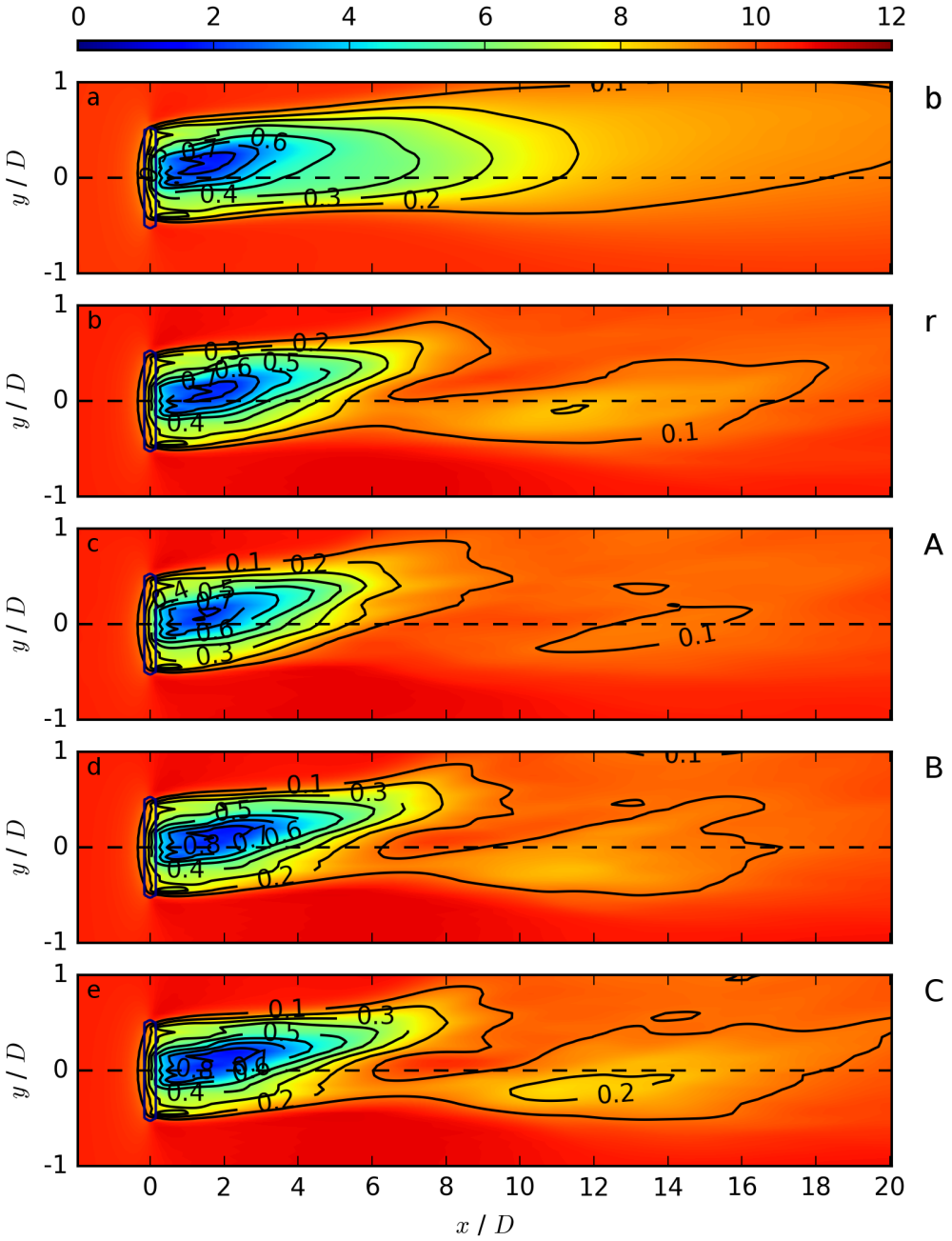

Figure 5.11: Nighttime horizontal cross sections of $\overline{u_{i,j,k_h}}$ in m s^{-1} for the benchmark wind-turbine simulation in a, the reference wind-turbine simulation in b and parameterization wind-turbine simulations of type A, B, and C in c, d, and e respectively. The black contours represent VD_{i,j,k_h}.

During day, the less rapid recovery in the reference wind-turbine simulation results from the value of α_0. The absence of the lateral wake deflection (Fig. 5.7*b*) can be attributed to the modification of using the same perturbation velocities for three time steps.

In the transitional period, the wake recovery at a certain downstream position is rather similar in the benchmark and in the reference wind-turbine simulation. The wake deflection from the benchmark wind-turbine simulation is also represented in the reference wind-turbine simulation. The smaller wake deflection angle can be attributed to the stratification dependent turbulent inflow method from Eq. 5.4, which uses the background turbulence of the EBL in combination with $\alpha_0 = 0.5$ instead of synchronized diurnal cycle data of the EBL. Further, the representation of the wake deflection in the reference wind-turbine simulation reinforces the reasoning of the different wake deflection angle during the day.

During night, the more rapid recovery in the reference wind-turbine simulation results from the value of α_0. Other differences during the night represent the upstream velocity profile, especially close to the ground, the flow pattern below the wake in between 4D and 8D, and the upward bending of the wake with larger velocity values between 6D and 8D (Fig. 5.10*b*). These differences can be related to a larger vertical gradient of the nighttime fit on u_e and v_e in Fig. 5.2 in comparison to the SBL profile, which serves as background wind profile in the benchmark wind-turbine simulation. The fitted profiles further result in a larger vertical gradient of the wind direction, which is related to a stronger wake deflection in the reference wind-turbine simulation, causing the more pronounced hub height differences between 6D and 8D.

The deviation of the reference wind-turbine simulation from the benchmark wind-turbine simulation is listed in Table 5.3 as (b - r) case for the day, the transition, and the night as vertical and lateral average. The values are calculated as the difference of the velocity deficit from Eq. 2.23 between the benchmark (b) and the reference (r) wind-turbine simulations. During day and night, the values are roughly twice as large as in the transitional state. This corresponds to the less (more) rapid wake recovery during the day (night) and is related to the value of α_0. The difference in the wake deflection angle is represented in the lateral value. The largest value during the day can be related to the much larger difference in the wake deflection angle during the day in comparison to the transitional and nighttime situation.

The presented comparison of the wake structures between the benchmark and the corresponding reference wind-turbine simulations reveal qualitatively and quantitatively consistent results for all three ABL regimes. The deviations can all be attributed to the simplifications, assumed in the reference wind-turbine simulation setup. Consequently, the reference wind-turbine simulations are adequate representations of the benchmark wind-turbine simulations at day, in the transitional period, and at night. This verifies the parameterization by using the diurnal cycle precursor simulation as stratification dependent turbulent inflow and a stratification related weighting of one in Eq. 5.4. Further, it enables in the following to compare the parameterization wind-turbine simulations directly to the reference wind-turbine simulations. This is an important step towards the verification of the proposed

Table 5.3: List of the velocity deficit deviation between two wind-turbine simulations for the day, the transition, and the night, as vertical and lateral average at a downstream position of 4D. The nomenclature b corresponds to benchmark, r to reference, A, B, and C to parameterization of type A, B, and C.

difference / %	day		transition		night	
slice	vertical	lateral	vertical	lateral	vertical	lateral
b - r	4.8	7.0	2.6	3.1	5.5	3.5
r - A	3.9	2.7	2.3	4.7	2.2	1.6
A - B	1.2	0.8	0.4	0.4	2.3	1.9
B - C	0.4	0.5	0.3	0.3	0.4	0.2

parameterization, using the precursor simulation of the NBL as input in the stratification related weighting and in the stratification dependent turbulent inflow.

Reference wind-turbine simulations and parameterization wind-turbine simulations of type A

As second step, the parameterization wind-turbine simulations of type A are compared to the reference wind-turbine simulations to investigate the impact of the NBL in combination with a stratification related weighting. The wake structures between the reference and the parameterization wind-turbine simulations of type A are rather similar, with only minor differences:

During day and in the transitional period, the wake recovery is slightly less rapid for applying function set of type A, whereas at night, the wake recovers slightly more rapidly.

The less rapid wake recovery during the day and the more rapid wake recovery during the night can be related to the NBL background turbulence in Eq. 5.4, which is larger than the SBL background turbulence in the nighttime reference wind-turbine simulation, resulting in a more rapid wake recovery, and smaller than the CBL background turbulence in the daytime reference wind-turbine simulation, resulting in a less rapid wake recovery. The contribution of the SBL and the CBL structure via the stratification related weighting account for the 3 D turbulence structure. However, it results in a less distinctive effect than using the background turbulence of the corresponding diurnal cycle regime in the reference wind-turbine simulations.

The wake recovery difference is less pronounced in the EBL in comparison to the CBL, as the fluctuations in Fig. 5.4 are rather similar for the EBL and the NBL, corresponding to a similar background turbulence of the EBL and the NBL.

Further, the wake in the transitional period in Fig. 5.8 is no longer deflected. This effect is caused by the consideration of the NBL fields as background turbulence instead of the EBL regime as it is the case in the reference wind-turbine simulation. The EBL contributes via the stratification related weighting $\boldsymbol{\alpha}_{i^*,j,k}$, however, the impact is not strong enough to represent the wake deflection. The lateral wake deflection from the reference wind-turbine simulation at night, however, is presented, as this deflection is related to the background wind profiles.

The deviation of the parameterization wind-turbine simulation of type A from the reference wind-turbine simulation is also listed in Table 5.3 as (r - A) for all regimes as vertical and lateral average. In comparison to the (b - r) differences, the (r - A) values are in most cases much smaller. This is in agreement with the rather similar wake structure in comparison to the obvious wake structure differences in (b - r). The relatively large lateral value in the transitional regime can be attributed to the wake deflection difference between the reference wind-turbine simulation and the type A parameterization wind-turbine simulation in Fig. 5.9. This effect is much less pronounced in the daytime (Fig. 5.7) and especially in the nighttime regime (Fig. 5.11), which is reflected in the corresponding lateral values. The vertical value is larger during the day in comparison to the transitional period. This can be related to the wake recovery difference between both. The vertical value at night is similar to the transitional one, even the wake recovers more rapidly at night in comparison to the less rapid recovery in the transitional period. This effect results from the use of the absolute values in the calculation of the averaged differences. However, as the tendency towards a more or less rapid recovery is persistent in the whole wake, the absolute values are verified.

The comparison of the wake structures between the reference and the corresponding parameterization wind-turbine simulations with function set of type A also reveals qualitatively and quantitatively consistent results for all three ABL regimes. The deviations can all be attributed to the use of the NBL precursor simulation in the stratification dependent turbulent inflow.

Parameterization wind-turbine simulations of type A, B, and C

As third step, the parameterization wind-turbine simulations of type B are compared to the type A parameterization wind-turbine simulations, which can be considered as the most accurate ones. Further, the parameterization wind-turbine simulations of type C are compared to the type B parameterization wind-turbine simulations, to investigate the impact of an additional simplification of the stratification related weighting $\boldsymbol{\alpha}_{i^*,j,k}$. The wake structures between the parameterization wind-turbine simulations of type A and B are rather similar, only the wake recovery at a certain position downstream of the wind turbine differs. In particular, the wake recovers more rapidly in the daytime regime and less rapidly in the nighttime regime for parameterization type B. In the transitional regime, the difference is marginal. The less rapid recovery during the night can be related to the removal of horizontal gradients in the matrices of type A in comparison to vectors of type

B. The more rapid recovery during the day is contradictory to this explanation, however, it can be related to the domination of $\mathbf{u}_{\alpha_k}$ over $\mathbf{u}_{\alpha_i}$ and $\mathbf{u}_{\alpha_j}$ (not shown here).

The deviation of the type B parameterization wind-turbine simulations from type A are listed in Table 5.3 as (A - B). The tendencies of a more or less rapid wake recovery during the day and the night result in similar sized vertical and lateral values. Both transitional values are much smaller than their daytime or nighttime equivalents, influenced by the marginal wake structure difference in Figs. 5.8 and 5.9.

The wake structure differences between the parameterization wind-turbine simulations of type B and C are only marginal in the x-y cross section at hub height, as the values α_u, α_v, and α_w correspond to hub height values of $\mathbf{u}_{\alpha_k}$. In the x-z cross sections through y_0, the wake recovers slightly more rapidly in the daytime situation and slightly less rapidly at night. In the transitional period, the difference is again marginal. Here, a similar explanation is valid, as the one explaining the difference between type A and type B simulations. The less rapid recovery during the night can be related to the removal of vertical gradients, whereas the more rapid recovery during the day is again contradictory to this explanation, however, it can be related to the relatively large values of α_u and α_v in Table 5.1 in comparison to the values of u_{α_k} and v_{α_k} at other heights in Fig. 5.4.

Further, the deviations of type C parameterization wind-turbine simulations from type B are also listed in Table 5.3 as (B-C). The lateral and vertical values are rather small for all regimes. This corresponds to the marginal difference between parameterization type B and C in Figs. 5.6 - 5.11. Small lateral values at hub height are expected, as the values α_u, α_v, and α_w from the parameterization of type C are also hub height values. The small vertical values, however, argue for a rather good parameterization of type C.

The comparison of the wake structures between the parameterization wind-turbine simulations of type A and type B and likewise of type B and type C reveal qualitatively and quantitatively consistent results for all three ABL regimes. The deviations can all be attributed to the simplifications in the stratification related weighting $\boldsymbol{\alpha}_{i^*,j,k}$.

Streamwise velocity ratio and total turbulent intensity

The parameterization effect on the streamwise velocity ratio profiles of Eq. 2.23 and the total turbulence intensity profiles of Eq. 2.25 are shown in Fig. 5.12 for the three ABL regimes. During day, the VR profiles (in a) are almost overlapping for the reference wind-turbine simulation and for the parameterization wind-turbine simulations of type A, B, and C. In the transitional state (in c), a slightly less rapid wake recovery prevails, compared to the reference wind-turbine simulation. Care must be taken when interpreting the streamwise VR through the centre of the rotor at night (in e) because of the wake deflection. Considering the profiles of I, the parameterization wind-turbine simulations of type A, B, and C are also in good agreement with the reference wind-turbine simulation for the day and the transitional state (in b and d). At night (in f), the values of I are slightly larger for the parameterization wind-turbine simulation of type A in comparison to type B and C, which correlates with the slightly more rapid wake recovery in Figs. 5.10 and 5.11.

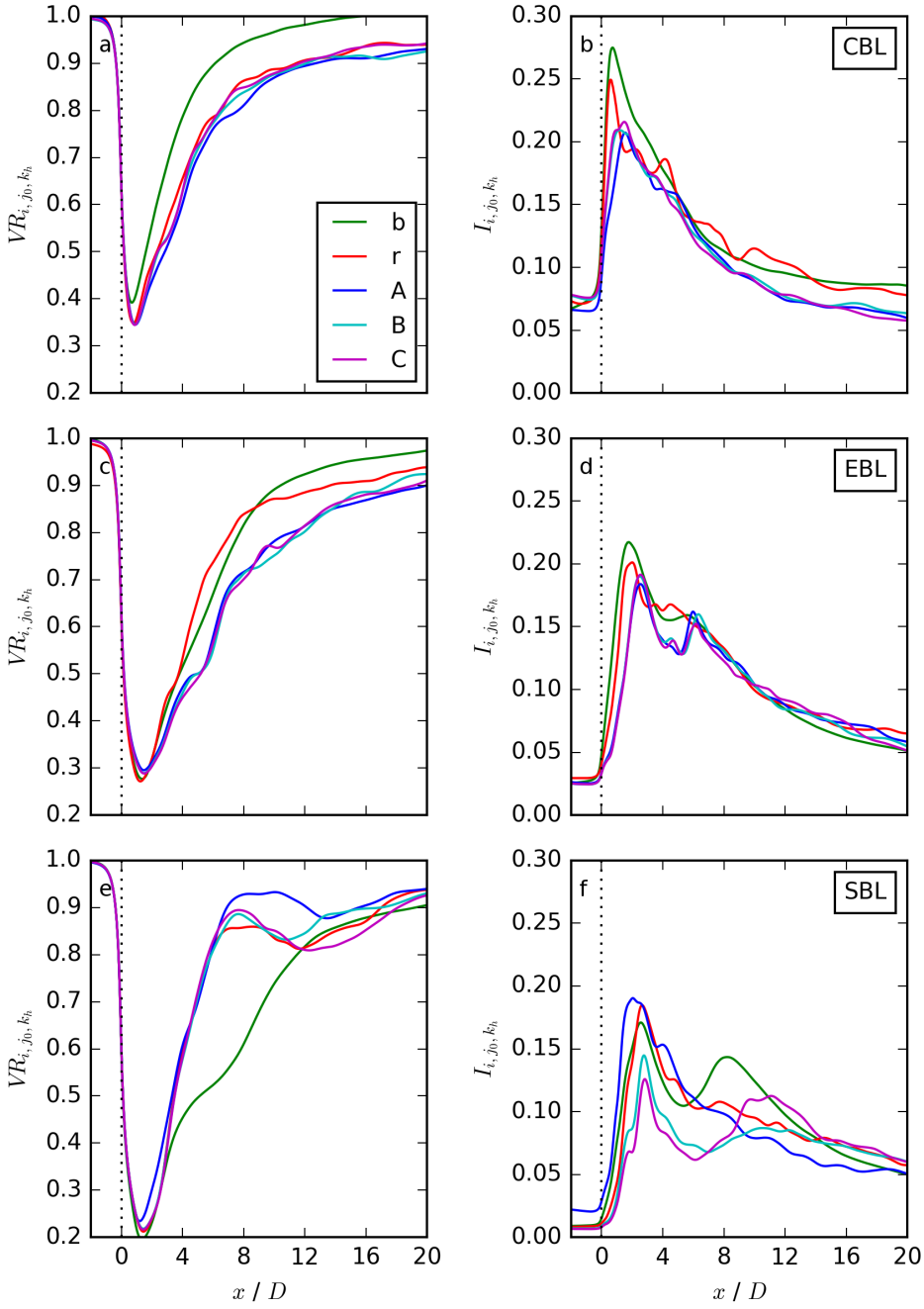

Figure 5.12: Dependence of the streamwise velocity ratio VR_{i,j_0,k_h} in a, c, and e as well as of the total turbulent intensity I_{i,j_0,k_h} in b, d and f for all wind-turbine simulations representing the daytime situation in a and b, the transition in c and d and the nighttime situation in e and f. The subscript 'b' corresponds to benchmark and 'r' to reference.

Therefore, the modified turbulence preserving method results in a great improvement of the profiles of VR and I in comparison to Fig. 5.3, especially regarding the total turbulent intensity. This is valid for the reference case as well as for all function sets applied for the stratification related weighting $\boldsymbol{\alpha}_{i^*,j,k}$.

5.5 Summary

The application of the numerically efficient parameterization of turbulent wind-turbine flows for LES of different thermal stratifications presents the following results:

The investigation of the developed parameterization reveals a rather good agreement of wind-turbine parameterizations of type A, B, and C with their corresponding reference wind-turbine simulation and also with the benchmark wind-turbine simulation. The only limitation of the parameterization is the too weak representation of the wake deflection in the parameterization wind-turbine simulations in comparison to the reference wind-turbine simulations, which is related to the use of the equilibrium state of the NBL simulations in the modified version of the turbulence preserving method.

The small vertical values in Table 5.3 for (B - C) and the fact that the stratification related weighting $\boldsymbol{\alpha}_{i^*,j,k}$ applied as function set C is the simplest one, makes function set C preferable over function set A and B. If the differences in Table 5.3 are calculated over the complete downstream region, the percentages decrease, however, the same relative difference persists as at a downstream position of 4D. Therefore, the vertical and lateral values at 4D are suitable as representations of the whole wake, reinforcing the preference of the parameterization with function set C.

The simple and computationally fast approach with function set of type C results in a numerically very efficient parameterization as it only requires an equilibrium state of an NBL precursor simulation together with stratification related values α_u, α_v, and α_w and the corresponding background wind profiles u_e, v_e, and w_e. It reduces the computational costs from 14 days, required for one diurnal cycle of the idealized ABL simulation and the corresponding four benchmark wind-turbine simulations, to less than one hour, each time performed on 256 Intel Xeon E5-2697 v3 threads at 2.6 GHz.

The development and successful validation of the numerically efficient parameterization of turbulent wind-turbine flows for LES of different thermal stratifications constitute the third step towards an increase of the wind-energy contribution to the primary energy demand. The development of the parameterization was essential to offer an alternative to the computationally extremely expensive precursor diurnal cycle simulation, which is necessary to perform wind-turbine simulations under different atmospheric conditions. Therefore, the parameterization offers a simple, numerically efficient, and computationally fast testbed for a large range of parameters to investigate how a wind turbine operates under different atmospheric conditions.

6 Conclusion

The contribution of this work towards the understanding of how a wind turbine operates under different atmospheric conditions will be evaluated in the following.

Impact of NBL turbulence on wind-turbine wakes

In a first approach, the impact of NBL turbulence on wind-turbine wakes is investigated. This allows the validation of the wind-turbine parameterizations and the development and the testing of the turbulence preserving method.

As essential very first step of a wind-turbine LES, the wake structure was investigated for different wind-turbine parameterizations and settings: The MMT and the BEM method were applied as wind-turbine parameterizations, the local blade characteristics in the BEM method were varied, and the effect of rotation of the actuator was studied. The MMT is a reasonable simplification of the BEM model for studies of the far wake, when near-wake characteristics are of secondary importance. Considering how sparse information on detailed blade geometries is available, the MMT offers an alternative, even in the near wake. As the impact of rotation of the wind turbine on the far wake is rather small, a non-rotating MMT approach can be assumed as further simplification. However, if the information on blade geometry is available, the BEM method with the corresponding blade characteristics should be applied to simulate a more realistic wake structure. This is for two reasons: Firstly, the airfoil has a crucial impact, even in the far wake. Secondly, the computational costs of the BEM method in comparison to the MMT are marginal.

The turbulence preserving method was designed and successfully validated against other simulation results and measurements as new methodology to preserve the background turbulence in an LES of a flow through a wind turbine with open horizontal boundary conditions. The method represents a simple and numerically very effective tool with a negligible memory requirement and a minimal domain size for studying the interaction of NBL flow with a wind turbine.

Further, the sensitivity of the wake to two SGS closure models (TKE and Smagorinsky-type models) and numerical simulations without an explicit SGS closure model (implicit LES) was studied as application of the turbulence preserving method. While the SGS closure models have a rather small impact on the streamwise velocity ratio, they have a remarkable impact on the streamwise turbulent intensity in the near wake. For a modification of

the amount of damping in the SGS closure model, even the implicit LES results agree surprisingly well with the base case simulation, reinforcing the suitability of the turbulence preserving method to study a wide class of ABL flows. The possibility of an implicit LES of wind-turbine flows further enables numerical simulations with stretched or adaptive meshes, where an explicit SGS parameterization might be difficult and troublesome.

This first approach illustrates the importance of the consideration of turbulence in a wind-turbine simulation. Further, it also illustrates the large effect of individual changes of the background turbulence on wind-turbine wakes. Therefore, the use of real atmospheric turbulence fields is strongly recommended for future applications.

The turbulence preserving method and the wind-turbine models, both implemented in the numerical model EULAG, allow for subsequent applications covering a wide range of scales, different thermal stratifications, as well as flow over heterogeneous or hilly terrain. The turbulence preserving method is fully adaptable by only applying three appropriate u, v, and w wind fields for the corresponding situation. This simplicity makes the turbulence preserving method most suitable as basic concept for the parameterization. However, the wind-turbine parameterizations do not consider any vertical wind. Therefore, the wind-turbine parameterizations have to be modified to make them applicable in situations with a large vertical wind component, e.g. a wind turbine sited at the edge of an escarpment.

Impact of the diurnal cycle of the ABL on wind-turbine wakes

In a second approach, the impact of the diurnal cycle of the ABL on wind-turbine wakes is investigated. This provides synchronized wind-turbine simulations of different diurnal cycle regimes. The diurnal cycle simulations were performed to deduce the parameterization ingredients and to serve as benchmark for the validation of the parameterization.

The successful validation of a full diurnal cycle of the field experiment BLLAST with the LES model EULAG gives confidence in its ability to simulate the diurnal cycle of an ABL.
An idealized diurnal cycle simulation of the ABL is performed over homogeneous surface with various atmospheric conditions occurring over the course of a day. They include differences in the low-level wind shear, the wind veer, and the total turbulent intensity. All of these characteristics are highly important for the parameterization and for studying the interaction of the ABL flow with a wind turbine, considering that a near-neutral stratification, which was used in most of previous numerical wind-turbine studies, occurs only with a frequency of roughly 10 % according to data from a representative field experiment (SWiFT Facility Representation and Preparedness; 730 days of measurement in the period from 2012 to 2014) (Kelley and Ennis, 2016).

The wind-turbine simulations represent all relevant regimes during a diurnal cycle, including stable and convective conditions as well as the morning and evening conditions. The

resulting wakes of the convective and the stable regimes are strongly influenced by the various atmospheric conditions of the precursor ABL simulation over homogeneous surface and confirm with previously published results. The wakes of the morning and the evening conditions provide the first insight in wake structures during transitional periods, which show a strong influence of the flow regime prior to the transition. Furthermore, the wind-turbine simulations allow adjustments of the domain size and the simulation time, and the rather similar wake structures throughout two full diurnal cycles, corresponding to a marginal impact of the initial conditions of the precursor simulation after 12 h, verify the investigation of the wake characteristics for the first diurnal cycle.

A detailed understanding of how a wind turbine operates under different atmospheric conditions occurring during the diurnal cycle is a crucial step to increase the wind-energy contribution to the primary energy demand. This work shows striking differences in the wake structure during the day and the night and also during both transitional states, which could eventually lead to better optimization techniques for wind farms e.g. regarding the siting or pitching of the individual wind turbines. Further, the wake differences strongly depend on the inflow conditions. Therefore, considering the upstream wind conditions, e.g. vertical wind shear and wind veer with height in the SBL and the MBL, could improve the rotor configurations and regulation systems. In addition to the CBL, the EBL, the SBL, and the MBL representatives, different other diurnal cycle states, e.g. the afternoon transition (Sandeep et al., 2015; Darbieu et al., 2015; Nilsson et al., 2016a,b), should also be considered for an increase of the wind-energy contribution to the primary energy demand in future wind-turbine simulations.

The numerical simulations investigating the impact of the diurnal cycle of the ABL on wind-turbine wakes lay the groundwork for a variety of further applications over a wide range of scales, for simulations considering moisture, and for flow over heterogeneous surfaces and hilly terrain.
The simulations in this work did not include atmospheric moisture. Low-level clouds, however, can be important for the wake response, especially if their cloud base is below the top tip height of a wind turbine. Therefore, including moisture in the EULAG simulations can be a reasonable next step.
Simulations including heterogeneous surface of hilly terrain can be conducted with only little extra effort by including the orography, because the numerical setup of the ABL simulations, the wind-turbine model, and the interface between ABL and wind-turbine simulations are all implemented in the geophysical flow solver EULAG. In EULAG, the governing equations are formulated and numerically solved in generalized curvilinear coordinates. Within the scope of this work, all implementations are also performed in generalized curvilinear coordinates. This feature in combination with the non-oscillatory foreward-in-time differencing, makes EULAG well-suited to simulate the interaction of a wind turbine with flow over hilly terrain. The additional implemented immersed boundary technique further allows numerical simulations over heterogeneous surfaces characterized by roughness elements.

As a first approach towards a more realistic representation of the surface conditions, the idealized ABL simulations were repeated for a flow over spatially distributed cubed obstacles corresponding to a surface density of 25%. This setup is a relevant scenario, as wind turbines are preferably placed in suburban areas to limit energy transfer and storage. The increase of shear in the lower levels and the resulting compensation of the formation of the night-time Ekman spiral is a key difference from the ABL simulation over homogeneous surface conditions at night and an important finding. The night-time flow field over rough surface has a crucial impact on the wake structure of a wind turbine, which differs completely from the homogeneous wake structure. In conclusion, low-level wind shear, wind veer, and the total turbulent intensity are not only the atmospheric variables with the dominant impact on the wake structure, the heterogeneous surface has an additional crucial impact on the wake structure.

For a more realistic simulation of the impact of heterogeneous surface on the wind-turbine wake, the wind turbine should be yawed with respect to the incoming wind. This was not conducted in the scope of this thesis, as the aim was to determine the pure impact of the surface configuration.

Another approach towards a more realistic flow could be the investigation of the wake response of a wind turbine affected by a hill or hilly terrain. This investigation does not necessarily require another diurnal cycle precursor simulation characterized by a 3 D hill or a 2 D ridge. Instead, the wind and the potential temperature data of the diurnal cycle simulation over homogeneous or heterogeneous terrain, conducted in this thesis, can be applied to wind-turbine simulations with open streamwise boundary conditions with the same coupling method as used in this thesis. The wind-turbine simulation setup should correspond to a hill or a ridge, affected by flow, which is influenced by homogeneous or heterogeneous terrain. The wind turbine can be placed on top of the 3 D hill or the 2 D ridge or at any other location on the luv or lee side. Only one thing has to be considered: If the hill or the ridge are simulated in a stable situation (e.g. SBL or MBL case in this work), the vertical domain size of the wind-turbine simulations has to be enlarged and a damping layer with a reciprocal damping time has to be implemented as upper boundary condition to avoid wave reflection from vertically propagating gravity waves. The effect of gravity waves on the efficiency of a wind farm has been investigated by Smith (2010). Simulations conducted with the setup of this work for an NBL (Heimann et al., 2017) show that a 3 D hill of 50 m, corresponding to roughly $^1/_{10}$ of the domain height, with a maximum slope angle ranging from 10° to 30°, does not present a numerical limitation. For other setups with a higher terrain elevation or a steeper slope angle, especially for stable conditions, precursor tests are recommendable.

The simulation of a measured atmospheric condition, e.g. an IOP (intensive observation period) of a field campaign, however, could require a diurnal cycle precursor simulation. Similar to the hindcast of an IOP of the BLLAST field campaign, this hindcast would require the wind and the temperature data and, depending on the atmospheric situation, even the moisture data for initialization. Further, additionally to the sensible heat flux

forcing, information of measured profiles of the wind, the potential temperature, and, if required, the moisture during the diurnal cycle are useful for the respective initial and boundary conditions and likewise for nudging of the simulation towards the measurements. In addition, external forcings like the subsidence velocity and the radiative cooling could be important to include mesoscale processes. The required interface between the wind-turbine simulation and the ABL simulation can be adapted from this work. Based on the knowledge of this work, this procedure is planned as next stage to simulate selected IOPs of the Perdigão field campaign (Mann et al., 2017), characterized by a terrain affected by a steep double ridge. This is a crucial next step, as it offers the possibility to expand the knowledge of how the atmosphere influences the wind-turbine wake characteristics in complex terrain.

A numerically efficient parameterization of turbulent wind-turbine flows for LES of different thermal stratifications

In a third approach, a numerically efficient parameterization of turbulent wind-turbine flows for LES of different thermal stratifications is introduced, implemented, and applied. The parameterization is based on the turbulence preserving method and utilizes a stratification related weighting and suitable background wind profiles from the idealized diurnal cycle simulation over homogeneous surface. The combination of the first and the second part of this work makes the developed parameterization appropriate for different thermal stratifications, despite the limitations of the idealized ABL simulation over homogeneous surface, which does not consider other external forcings than the sensible heat flux, large- or mesoscale flow systems, local wind systems, or moisture. Further, the upstream profiles are only characterized by statistical homogeneous turbulence fields without considering surface heterogeneities of any kind.

The simplest function set of the stratification related parameters consists of only three values α_u, α_v, and α_w. Surprisingly, these three scalars are sufficient to reproduce the atmospheric daytime, transition, and nighttime situation in the wind-turbine simulations, which are quantitatively comparable to the synchronized diurnal cycle benchmark wind-turbine simulations over homogeneous surface. With the simplest approach, no diurnal cycle precursor simulation is needed, the values α_u, α_v, and α_w can be approximated for different atmospheric situations by taking the values determined in this study. This reduces the computational costs in comparison to the diurnal cycle and the benchmark wind-turbine simulations by a factor of $\mathcal{O}(10^2)$, resulting in a numerically very efficient tool.

The parameterization, developed and tested in this thesis, offers a simple, efficient, and computationally very fast approach providing a first impression of the expected wake structure. It further offers a testbed for a large range of parameters, like different rotor configurations, different subgrid-scale models, different atmospheric conditions, ranging from very stable to stable, to near-neutral, to convective, to very convective (by varying α_u, α_v, and α_w), or different background wind profiles (by varying the fit used for u_e, v_e, and

w_e). Another important advantage of the parameterization is the possibility of extracting turbulence fields at every time step of interest in comparison to a RANS approach.

Despite the promising results of the developed parameterization, there is improving potential:
The application of a repeating turbulence structure (no temporal evolution) in the parameterization is not a perfect method. However, taking into account that in many other cases like in artificial neural networks, which are used for wind power forecasting to learn the relation between numerical weather prediction and actual production (Bessa et al., 2012), even 1-h averages of the wind are used, a repeating turbulent structure is a good and sufficient first assumption for the parameterization.
Therefore, as alternative, the benchmark wind-turbine simulation in the convective case could be reproduced with only the three 3 D wind fields at 12 h, instead of the synchronized simulations ranging from 12 h to 13 h, which are corresponding to different phases of the diurnal cycle behaviour. This makes it more comparable to the reference wind-turbine simulation, which only uses the three 3 D wind fields at 12 h as input into the stratification dependent turbulent inflow of the parameterization. The same is valid for the EBL and the SBL representatives.
Another limitation of the parameterization is the too weak representation of the wake deflection in the parameterization wind-turbine simulations in comparison to the benchmark wind-turbine simulations. This behaviour could also be improved e.g. by including additional terms which represent the upstream wind direction in more detail than it is the case in $\boldsymbol{\alpha}_{i^*,j,k}$. This step, however, would make the parameterization very complex by requiring detailed information of the upstream wind. As the aim of this work was to develop a simple parameterization, this was not taken into account.

An important subsequent step for the advancement of this parameterization will be to conduct an ensemble of stratification related weighting values and background wind profiles for different setups of the idealized diurnal cycle simulation over homogeneous surface, e.g. different surface flux profiles. Further, the parameterization ingredients could also be determined for heterogeneous and hilly terrain, in a rather similar way as done for the homogeneous idealized diurnal cycle simulation, resulting in a pool of parameters, applicable for different general specifications. To meet the requirements of a specific locality and/or atmospheric conditions, the effort of determining the stratification related weighting and suitable background wind profiles for the parameterization has to be repeated. This includes the reproduction of the diurnal cycle simulation. However, all relevant steps in the parameterization as well as the NBL equilibrium state can be adapted from this work.

These applications make the parameterization developed in this thesis a viable tool to investigate the response of the wind-turbine wake to a turbulent atmospheric boundary-layer flow. An important remaining issue is the application of the interface method between wind-turbine and ABL simulations and the parameterization in other numerical models:
One difference between the numerical model EULAG and other models like WRF or PALM (PArallelized Large-eddy simulation Model) is the use of Θ' in the EULAG setup of this

work, contrasting the use of Θ in the other numerical models. However, this can easily be adapted as $\Theta_e(z)$ is horizontally homogeneous in the problems considered in this work. The parameterization can even be used without difficulty and without further adaptions in other numerical models, because the parameterization only uses $\tilde{\psi} = (u, v, w)$ and $\tilde{\psi}_e = (u_e, v_e, w_e)$ instead of $\psi = (u, v, w, \Theta')$ and $\psi_e = (u_e, v_e, w_e, \Theta_e)$.

The wind-turbine simulations representing different atmospheric states of the diurnal cycle, as well as the parameterization and all further discussed adaptions, make an important progress of accessing the way how the atmospheric conditions influence the wind-turbine wake characteristics. The results of this work recommend for future work to place special emphasis on the application of the corresponding blade data, the atmospheric situation, the surface conditions, and the appropriate background turbulence field, as all four ingredients are essential to achieve more realistic simulation results. The turbulence preserving method as well as the parameterization, both developed and validated in this thesis, can serve as useful tools for future investigations. Being aware of the discussed limitations, this work has greatly improved the knowledge of the response of the wind-turbine wake to a turbulent ABL flow. For this reason, it constitutes an important contribution to increase the utilization of wind energy and therefore the wind-energy contribution to the primary energy demand in the future.

Acronyms

ABL	atmospheric boundary layer
ADM	actuator disc model
ALM	actuator line model
BEM	blade-element momentum
BLLAST	Boundary Layer Late Afternoon and Sunset Turbulence
CBL	convective boundary layer
EBL	evening boundary layer
EULAG	EUlarian / semi-LAGrangian
IOP	intensive observation period
LES	large-eddy simulation
LLJ	low-level jet
MBL	morning boundary layer
MMT	modified momentum theory
MPDATA	Multi-dimensional Positive Definite Advection Transport Algorithm
NBL	neutral boundary layer
PALM	PArallelized Large-eddy simulation Model
RANS	Reynolds-averaged Navier-Stokes
SBL	stable boundary layer
SGS	subgrid-scale
TKE	turbulent kinetic energy
WRF	Weather Research and Forecasting

Bibliography

Abkar M, Porté-Agel F (2014) The effect of atmospheric stability on wind-turbine wakes: A large-eddy simulation study. In: Journal of Physics: Conference Series, IOP Publishing, vol 524, p 012138, DOI 10.1088/1742-6596/524/1/012138

Abkar M, Sharifi A, Porté-Agel F (2016) Wake flow in a wind farm during a diurnal cycle. Journal of Turbulence 17(4):420–441, DOI 10.1080/14685248.2015.1127379

Aitken ML, Kosović B, Mirocha JD, Lundquist JK (2014) Large eddy simulation of wind turbine wake dynamics in the stable boundary layer using the Weather Research and Forecasting Model. J Renew Sust Energy 6:1529–1539

Baker RW, Walker SN (1984) Wake measurements behind a large horizontal axis wind turbine generator. Solar Energy 33(1):5–12, DOI 10.1016/0038-092X(84)90110-5

Balsley BB, Svensson G, Tjernström M (2008) On the scale-dependence of the gradient richardson number in the residual layer. Bound-Lay Meteorol 127(1):57–72, DOI 10.1007/s10546-007-9251-0

Basu S, Vinuesa JF, Swift A (2008) Dynamic les modeling of a diurnal cycle. J Appl Meteorol Clim 47(4):1156–1174, DOI 10.1175/2007JAMC1677.1

Beare RJ (2008) The Role of Shear in the Morning Transition Boundary Layer. Bound-Lay Meteorol 129(3):395–410, DOI 10.1007/s10546-008-9324-8

Beare RJ, Macvean MK, Holtslag AAM, Cuxart J, Esau I, Golaz JC, Jimenez MA, Khairoutdinov M, Kosović B, Lewellen D, Lund TS, Lundquist JK, Mccabe A, Moene AF, Noh Y, Raasch S, Sullivan P (2006) An Intercomparison of Large-Eddy Simulations of the Stable Boundary Layer. Bound-Lay Meteorol 118(2):247–272, DOI 10.1007/s10546-004-2820-6

Belcher S, Jerram N, Hunt J (2003) Adjustment of a turbulent boundary layer to a canopy of roughness elements. J Fluid Mech 488:369–398

Bellon G, Stevens B (2012a) Using the sensitivity of large-eddy simulations to evaluate atmospheric boundary layer models. J Atmos Sci 69:1582–1601

Bellon G, Stevens B (2012b) Using the sensitivity of large-eddy simulations to evaluate atmospheric boundary layer models. J Atmos Sci 69(5):1582–1601, DOI 10.1175/JAS-D-11-0160.1

Bessa RJ, Miranda V, Botterud A, Zhou Z, Wang J (2012) Time-adaptive quantile-copula for wind power probabilistic forecasting. Renewable Energy 40(1):29–39

Bhaganagar K, Debnath M (2014) Implications of Stably Stratified Atmospheric Boundary Layer Turbulence on the Near-Wake Structure of Wind Turbines. Energies 7(9):5740–5763, DOI 10.3390/en7095740

Bhaganagar K, Debnath M (2015) The effects of mean atmospheric forcings of the stable atmospheric boundary layer on wind turbine wake. Journal of Renewable and Sustainable Energy 7(1):013,124, DOI 10.1063/1.4907687

Blay-Carreras E, Pino D, Vilà-Guerau de Arellano J, van de Boer A, De Coster O, Darbieu C, Hartogensis O, Lohou F, Lothon M, Pietersen H (2014) Role of the residual layer and large-scale subsidence on the development and evolution of the convective boundary layer. Atmos Chem Phys 14(9):4515–4530, DOI 10.5194/acp-14-4515-2014

Bou-Zeid E, Meneveau C, Parlange MB (2004) Large-eddy simulation of neutral atmospheric boundary layer flow over heterogeneous surfaces: Blending height and effective surface roughness. Water Resources Research 40(2)

BP (2016) Statistical Review of World Energy. `bp.com/statisticalreview`, [Online; accessed 20-February-2017]

Calaf M, Meneveau C, Meyers J (2010a) Large eddy simulation study of fully developed wind-turbine array boundary layers. Physics of fluids 22(1):015,110

Calaf M, Meneveau C, Meyers J (2010b) Large eddy simulation study of fully developed wind-turbine array boundary layers. Phys Fluids 22:015110

Calaf M, Higgins C, Parlange MB (2014) Large wind farms and the scalar flux over an heterogeneously rough land surface. Boundary-layer meteorology 153(3):471–495

Carlson MA, Stull RB (1986) Subsidence in the nocturnal boundary layer. J Clim Appl Meteorol 25(8):1088–1099, DOI 10.1175/1520-0450(1986)025⟨1088:SITNBL⟩2.0.CO;2

Chamorro LP, Porté-Agel F (2009) A wind-tunnel investigation of wind-turbine wakes: Boundary-layer turbulence effects. Boundary-Layer Meteorol 132:129–149

Chamorro LP, Porté-Agel F (2010) Effects of thermal stability and incoming boundary-layer flow characteristics on wind-turbine wakes: A wind-tunnel study. Boundary-Layer Meteorol 136:515–533

Conzemius R, Fedorovich E (2007) Bulk models of the sheared convective boundary layer: Evaluation through large eddy simulations. J Atmos Sci 64(3):786–807, DOI 10.1175/JAS3870.1

Darbieu C, Lohou F, Lothon M, Vilà-Guerau de Arellano J, Couvreux F, Durand P, Pino D, Patton EG, Nilsson E, Blay-Carreras E, et al. (2015) Turbulence vertical structure of the boundary layer during the afternoon transition. Atmospheric Chemistry and Physics 15(17):10,071–10,086

Deardorff JW (1974a) Three-dimensional numerical study of the height and mean structure of a heated planetary boundary layer. Bound-Lay Meteorol 7(1):81–106, DOI 10.1007/BF00224974

Deardorff JW (1974b) Three-dimensional numerical study of turbulence in an entraining mixed layer. Bound-Lay Meteorol 7(2):199–226, DOI 10.1007/BF00227913

Dörenkämper M, Witha B, Steinfeld G, Heinemann D, Kühn M (2015) The impact of stable atmospheric boundary layers on wind-turbine wakes within offshore wind farms. Journal of Wind Engineering and Industrial Aerodynamics 144:146–153

Dörnbrack A, Schumann U (1993) Numerical simulation of turbulent convective flow over wavy terrain. Bound-Lay Meteorol 65(4):323–355, DOI 10.1007/BF00707032

Doyle JD, Gaberšek S, Jiang Q, Bernardet L, Brown JM, Dörnbrack A, Filaus E, Grubišic V, Kirshbaum DJ, Knoth O, et al. (2011) An intercomparison of t-rex mountain-wave simulations and implications for mesoscale predictability. Mon Weather Rev 139:2811–2831

El Kasmi A, Masson C (2008) An extended model for turbulent flow through horizontal-axis wind turbines. J Wind Eng Ind Aerodyn 96:103–122

Emeis S (2013) Wind energy meteorology: Atmospheric physics for wind power generation. Springer Science & Business Media, 196 pp

Emeis S (2014) Current issues in wind energy meteorology. Meteorol Appl 21:803–819

Englberger A, Dörnbrack A (2017a) Impact of neutral boundary-layer turbulence on wind-turbine wakes: A numerical modelling study. Boundary-Layer Meteorology 162(3):427–449

Englberger A, Dörnbrack A (2017b) Impact of the diurnal cycle of the atmospheric boundary layer on wind-turbine wakes: A numerical modelling study. Boundary-Layer Meteorology pp 1–26

Englberger A, Dörnbrack A (2017c) A numerically efficient parametrization of turbulent wind-turbine flows for LES of different thermal stratifications. Boundary-Layer Meteorology, under review

Fedorovich E, Nieuwstadt F, Kaiser R (2001) Numerical and laboratory study of a horizontally evolving convective boundary layer. part i: Transition regimes and development of the mixed layer. J Atmos Sci 58(1):70–86, DOI 10.1175/1520-0469(2001)058⟨0070:NALSOA⟩2.0.CO;2

Fröhlich J (2006) Large Eddy Simulation turbulenter Strömungen. Teubner Verlag / GWV Fachverlage GmbH, Wiesbaden, 414 pp

Froude RE (1889) On the part played in propulsion by difference of fluid pressure. Trans RINA 30:390

Gisinger S, Dörnbrack A, Schröttle J (2015) A modified darcy's law. Theoretical and Computational Fluid Dynamics 29(4):343

Glauert H (1963) Airplane propellers. In: Aerodynamic theory, W. F. Durand, Dover, New York, pp 169–360.

Gomes VMMGC, Palma JMLM, Lopes AS (2014) Improving actuator disk wake model. In: The science of making torque from wind. Conference series, vol 524, p 012170.

Grimsdell AW, Angevine WM (2002) Observations of the afternoon transition of the convective boundary layer. J Appl Meteorol 41(1):3–11, DOI 10.1175/1520-0450(2002)041⟨3C0003:OOTATO⟩3E2.0.CO;2

Grinstein FF, Margolin LG, Rider WJ (2007) Implicit Large Eddy Simulation. Cambridge university press, 546 pp

Hancock P, Zhang S (2015) A wind-tunnel simulation of the wake of a large wind turbine in a weakly unstable boundary layer. Boundary-Layer Meteorol 156(3):395–413, DOI 10.1007/s10546-015-0037-5

Hancock PE, Pascheke F (2014) Wind-tunnel simulation of the wake of a large wind turbine in a stable boundary layer: Part 2, the wake flow. Boundary-Layer Meteorol 151(1):23–37, DOI 10.1007/s10546-013-9887-x

Hansen MO (2008) Aerodynamics of wind turbines, vol 2. Earthscan, London and Sterling, UK and USA, 181 pp

Heimann D, Käsler Y, Gross G (2011) The wake of a wind turbine and its influence on sound propagation. Meteorol Z 20:449–460

Heimann D, Englberger A, Schady A (2017) Sound propagation through the wake flow of a hill-top wind tubine - a numerical study. Wind Energy, under review

Iungo GV, Porté-Agel F (2014) Volumetric lidar scanning of wind turbine wakes under convective and neutral atmospheric stability regimes. J Atmos Ocean Technol 31(10):2035–2048, DOI 10.1175/JTECH-D-13-00252.1

Iungo GV, Wu YT, Porté-Agel F (2013) Field measurements of wind turbine wakes with lidars. J Atmos Ocean Technol 30:274–287

Ivanell BS, Mikkelsen R, Henningson D (2008) Validation of methods using EllipSys3D. Technical report, KTH, TRITA-MEK 2008:12, pp 183–221.

Kang SL, Lenschow DH (2014) Temporal evolution of low-level winds induced by two-dimensional mesoscale surface heat-flux heterogeneity. Boundary-layer meteorology 151(3):501–529

Kang SL, Lenschow D, Sullivan P (2012) Effects of mesoscale surface thermal heterogeneity on low-level horizontal wind speeds. Boundary-layer meteorology 143(3):409–432

Käsler Y, Rahm S, Simmet R, Kühn M (2010) Wake measurements of a multi-MW wind turbine with coherent long-range pulsed doppler wind lidar. J Atmos Ocean Technol 27:1529–1532

Kataoka H, Mizuno M (2002) Numerical flow computation around aeroelastic 3D square cylinder using inflow turbulence. Wind and Structures 5:379–392

Kelley CL, Ennis BL (2016) Swift site atmospheric characterization. Tech. rep., Sandia National Laboratories (SNL-NM), Albuquerque, NM (United States)

Kühnlein C, Smolarkiewicz PK, Dörnbrack A (2012) Modelling atmospheric flows with adaptive moving meshes. J Comput Phys 231:2741–2763

Kumar V, Kleissl J, Meneveau C, Parlange MB (2006) Large-eddy simulation of a diurnal cycle of the atmospheric boundary layer: Atmospheric stability and scaling issues. water resour res 42(6), DOI 10.1029/2005WR004651

von Larcher T, Dörnbrack A (2014) Numerical simulations of baroclinic driven flows in a thermally driven rotating annulus using the immersed boundary method. Meteorologische Zeitschrift pp 1–12

Lothon M, Lohou F, Pino D, Couvreux F, Pardyjak ER, Reuder J, Vilà-Guerau de Arellano J, Durand P, Hartogensis O, Legain D, Augustin P, Gioli B, Lenschow DH, Faloona I, Yagüe C, Alexander DC, Angevine WM, Bargain E, Barrié J, Bazile E, Bezombes Y, Blay-Carreras E, van de Boer a, Boichard JL, Bourdon a, Butet a, Campistron B, de Coster O, Cuxart J, Dabas a, Darbieu C, Deboudt K, Delbarre H, Derrien S, Flament P, Fourmentin M, Garai a, Gibert F, Graf a, Groebner J, Guichard F, Jiménez Ma, Jonassen M, van den Kroonenberg a, Magliulo V, Martin S, Martinez D, Mastrorillo L, Moene aF, Molinos F, Moulin E, Pietersen HP, Piguet B, Pique E, Román-Cascón C, Rufin-Soler C, Saïd F, Sastre-Marugán M, Seity Y, Steeneveld GJ, Toscano P, Traullé O, Tzanos D, Wacker S, Wildmann N, Zaldei a (2014) The BLLAST field experiment: Boundary-Layer Late Afternoon and Sunset Turbulence. Atmos Chem Phys 14(20):10,931–10,960, DOI 10.5194/acp-14-10931-2014

Lu H, Porté-Agel F (2011) Large-eddy simulation of a very large wind farm in a stable atmospheric boundary layer. Physics of Fluids 23(6):065,101

Magnusson M, Smedman A (1994) Influence of atmospheric stability on wind turbine wakes. Wind Engineering 18(3):139–152, DOI 10.1063/1.4913695

Mahrt L (1998) Nocturnal boundary-layer regimes. Bound-Lay Meteorol 88(2):255–278, DOI 10.1023/A:1001171313493

Mann J (1994) The spatial structure of neutral atmospheric surface-layer turbulence. J Fluid Mech 273:141–168

Mann J, Angelou N, Arnqvist J, Callies D, Cantero E, Arroyo RC, Courtney M, Cuxart J, Dellwik E, Gottschall J, et al. (2017) Complex terrain experiments in the new european wind atlas. Phil Trans R Soc A 375(2091):20160,101

Manwell J, McGowan J, Roger A (2002) Wind Energy Explained: Theory, Design and Application. Wiley: New York, NY, USA, 134 pp

Margolin L, Rider W (2002) A rationale for implicit turbulence modelling. International Journal for Numerical Methods in Fluids 39:821–841

Margolin L, Smolarkiewicz PK, Wyszogrodzki A (2002) Implicit turbulence modeling for high reynolds number flows. Journal of Fluids Engineering 124:862–867

Margolin L, Rider W, Grinstein F (2006) Modeling turbulent flow with implicit les. Journal of Turbulence 7:1–27

Mazzitelli IM, Cassol M, Miglietta MM, Rizza U, Sempreviva aM, Lanotte aS (2014) The role of subsidence in a weakly unstable marine boundary layer: a case study. Nonlinear Proc Geoph 21(2):489–501, DOI 10.5194/npg-21-489-2014

Medici D, Alfredsson PH (2006) Measurements on a wind turbine wake: 3D effects and bluff body vortex shedding. Wind Energy 9:219–236

Meyers J, Meneveau C (2013) Flow visualization using momentum and energy transport tubes and applications to turbulent flow in wind farms. J Fluid Mech 715:335–358

Micallef D, Bussel GV, Sant T (2013) An investigation of radial velocities for a horizontal axis wind turbine in axial and yawed flows. Wind Energy 16:529–544

Mikkelsen R (2003) Actuator disc methods applied to wind turbines. PhD thesis, Technical University of Denmark

Millward-Hopkins J, Tomlin A, Ma L, Ingham D, Pourkashanian M (2012) The predictability of above roof wind resource in the urban roughness sublayer. Wind Energy 15(2):225–243

Mirocha J, Kirkil G, Bou-Zeid E, Chow FK, Kosović B (2013) Transition and equilibration of neutral atmospheric boundary layer flow in one-way nested large-eddy simulations using the weather research and forecasting model. Mon Weather Rev 141:918–940

Mirocha J, Kosovic B, Aitken M, Lundquist J (2014) Implementation of a generalized actuator disk wind turbine model into the weather research and forecasting model for large-eddy simulation applications. J Renew Sust Energy 6:013104

Mirocha JD, Kosović B (2010) A large-eddy simulation study of the influence of subsidence on the stably stratified atmospheric boundary layer. Boundary-Layer Meteorol 134(1):1–21, DOI 10.1007/s10546-009-9449-4

Mirocha JD, Rajewski DA, Marjanovic N, Lundquist JK, Kosović B, Draxl C, Churchfield MJ (2015) Investigating wind turbine impacts on near-wake flow using profiling lidar data and large-eddy simulations with an actuator disk model. Journal of Renewable and Sustainable Energy 7(4):043,143

wind-turbine models (2016) wind-turbine models. `https://www.wind-turbine-models.com/`, [Online; accessed 20-February-2017]

Moeng CH, Sullivan PP (1994) A comparison of shear-and buoyancy-driven planetary boundary layer flows. J Atmos Sci 51(7):999–1022, DOI 10.1175/1520-0469(1994)051⟨0999:ACOSAB⟩2.0.CO;2

Muñoz-Esparza D, Kosović B, Mirocha J, van Beeck J (2014) Bridging the transition from mesoscale to microscale turbulence in numerical weather prediction models. Boundary-Layer Meteorol 153:409–440

Naughton JW, Heinz S, Balas M, Kelly R, Gopalan H, Lindberg W, Gundling C, Rai R, Sitaraman J, Singh M (2011) Turbulence and the isolated wind turbine. In: 6th AIAA Theoretical Fluid Mechanics Conference, Honolulu, Hawaii, pp 1–19.

Nieuwstadt FT (1984) The turbulent structure of the stable, nocturnal boundary layer. J Atmos Sci 41(14):2202–2216, DOI 10.1175/1520-0469(1984)041⟨2202:TTSOTS⟩2.0.CO;2

Nilsson E, Lohou F, Lothon M, Pardyjak E, Mahrt L, Darbieu C (2016a) Turbulence kinetic energy budget during the afternoon transition–part 1: Observed surface tke budget and boundary layer description for 10 intensive observation period days. Atmospheric Chemistry and Physics 16(14):8849–8872

Nilsson E, Lothon M, Lohou F, Pardyjak E, Hartogensis O, Darbieu C (2016b) Turbulence kinetic energy budget during the afternoon transition–part 2: A simple tke model. Atmospheric Chemistry and Physics 16(14):8873–8898

Pelte D (2014) Die Zukunft unserer Energieversorgung: eine Analyse aus mathematisch-naturwissenschaftlicher Sicht. Springer-Verlag

Pino D, Vilà-Guerau de Arellano J, Duynkerke PG (2003) The contribution of shear to the evolution of a convective boundary layer. J Atmos Sci 60(16):1913–1926, DOI 10.1175/1520-0469(2003)060⟨1913:TCOSTT⟩2.0.CO;2

Pino D, Jonker HJ, De Arellano JVG, Dosio A (2006) Role of shear and the inversion strength during sunset turbulence over land: characteristic length scales. Bound-Lay Meteorol 121(3):537–556, DOI 10.1007/s10546-006-9080-6

Porté-Agel F, Lu H, Wu YT (2010) A large-eddy simulation framework for wind energy applications. In: The Fifth International Symposium on Computational Wind Engineering, vol 23-27 May 2010, Chapel Hill, North Carolina, USA

Prusa JM, Smolarkiewicz PK, Wyszogrodzki AA (2008) EULAG, a computational model for multiscale flows. Computers & Fluids 37:1193–1207

Rankine WJM (1865) On the mechanical principles of the action of propellers. Trans RINA 6:13

Rhodes ME, Lundquist JK (2013) The effect of wind-turbine wakes on summertime us midwest atmospheric wind profiles as observed with ground-based doppler lidar. Boundary-Layer Meteorol 149(1):85–103, DOI 10.1007/s10546-013-9834-x

Sandeep A, Rao TN, Rao S (2015) A comprehensive investigation on afternoon transition of the atmospheric boundary layer over a tropical rural site. Atmospheric Chemistry and Physics 15(13):7605–7617

Sathe A, Mann J, Barlas T, Bierbooms W, Bussel G (2013) Influence of atmospheric stability on wind turbine loads. Wind Energy 16(7):1013–1032, DOI 10.1002/we.1528

Schetz JA, Fuhs AE (1996) Handbook of fluid dynamics and fluid machinery. Wiley, New York, 2776 pp

Schmidt H, Schumann U (1989) Coherent structure of the convective boundary layer derived from large-eddy simulations. J Fluid Mech 200:511–562, DOI 10.1017/S0022112089000753

Schröttle J, Dörnbrack A (2013) Turbulence structure in a diabatically heated forest canopy composed of fractal pythagoras trees. Theoretical and Computational Fluid Dynamics pp 1–23

Shapiro A, Fedorovich E (2010) Analytical description of a nocturnal low-level jet. Quarterly Journal of the Royal Meteorological Society 136(650):1255–1262

Smith RB (2010) Gravity wave effects on wind farm efficiency. Wind Energy 13(5):449–458

Smolarkiewicz PK, Charbonneau P (2013) EULAG, a computational model for multiscale flows: An MHD extension. J Comput Phys 236:608–623

Smolarkiewicz PK, Dörnbrack A (2008) Conservative integrals of adiabatic durran's equations. Int J Numer Methods Fluids 56:1513–1519

Smolarkiewicz PK, Margolin LG (1993) On forward-in-time differencing for fluids: extension to a curviliniear framework. Mon Weather Rev 121:1847–1859

Smolarkiewicz PK, Margolin LG (1998) MPDATA: A Finite-Difference Solver for Geophysical Flows. J Comput Phys 140:459–480

Smolarkiewicz PK, Prusa JM (2002) Forward-in-time differencing for fluids: simulation of geophysical turbulence. In: Turbulent Flow Computation, Kluwer Academic Publishers, Boston, USA, pp 279-312

Smolarkiewicz PK, Prusa JM (2005) Towards mesh adaptivity for geophysical turbulence: continuous mapping approach. Int J Numer Methods Fluids 47:789–801

Smolarkiewicz PK, Pudykiewicz JA (1992) A class of semi-Lagrangian approximations for fluids. J Atmos Sci 49:2082–2096

Smolarkiewicz PK, Winter CL (2010) Pores resolving simulation of darcy flows. J Comput Phys 229:3121–3133

Smolarkiewicz PK, Sharman R, Weil J, Perry SG, Heist D, Bowker G (2007) Building resolving large-eddy simulations and comparison with wind tunnel experiments. J Comput Phys 227:633–653, DOI 10.1016/j.jcp.2007.08.005

Sorbjan Z (1996) Effects caused by varying the strength of the capping inversion based on a large eddy simulation model of the shear-free convective boundary layer. J Atmos Sci 53(14):2015–2024, DOI 10.1175/1520-0469(1996)053⟨2015:ECBVTS⟩2.0.CO;2

Sorbjan Z (1997) Decay of convective turbulence revisited. Bound-Lay Meteorol 82(3):503–517, DOI 10.1023/A:1000231524314

Sorbjan Z (2004) Large-eddy simulations of the baroclinic mixed layer. Bound-Lay Meteorol 112:57–80, DOI 10.1023/B:BOUN.0000020161.99887.b3

Sorbjan Z (2007) A numerical study of daily transitions in the convective boundary layer. Bound-Lay Meteorol 123(3):365–383, DOI 10.1007/s10546-006-9147-4

Stull RB (1988) An Introduction of Boundary Layer Meteorology. Dordrecht, Kluwer Academic

Sullivan PP, Moeng CH, Stevens B, Lenschow DH, Mayor SD (1998) Structure of the Entrainment Zone Capping the Convective Atmospheric Boundary Layer. J Atmos Sci 55(19):3042–3064, DOI 10.1175/1520-0469(1998)055⟨3042:SOTEZC⟩2.0.CO;2

Tian W, Ozbay A, Yuan W, Sarakar P, Hu H (2013) An experimental study on the performances of wind turbines over complex terrain. In: 51st AIAA Aerospace Sciences Meeting including the New Horizons Forum and Aerospace Exposition, vol 07-10 January 2013, Grapevine, Texas, USA, pp 1–14.

Tossas LAM, Leonardi S (2013) Wind turbine modeling for computational fluid dynamics: December 2010-December 2012. NREL Technical Monitor: Pat Moriarty, pp 1–48.

Troldborg N, Sørensen JN, Mikkelsen R (2007) Actuator line simulation of wake of wind turbine operating in turbulent inflow. In: The science of making torque from wind. Conference series, vol 75, p 012063.

Vanderwende B, Lundquist JK (2012) The modification of wind turbine performance by statistically distinct atmospheric regimes. Environmental Research Letters 7(3):034,035

Vollmer L, Steinfeld G, Heinemann D, Kühn M (2016) Estimating the wake deflection downstream of a wind turbine in different atmospheric stabilities: An les study. Wind Energy Science 1(2):129–141

Walter K, Weiss CC, Swift AH, Chapman J, Kelley ND (2009) Speed and direction shear in the stable nocturnal boundary layer. Journal of Solar Energy Engineering 131(1):011,013, DOI 10.1115/1.3035818

Wedi NP, Smolarkiewicz PK (2006) Direct numerical simulation of the plumb-McEwan laboratory analog of the QBO. J Atmos Sci 63:3226–3252

Wehner B, Siebert H, Ansmann A, Ditas F, Seifert P, Stratmann F, Wiedensohler A, Apituley A, Shaw R, Manninen H, et al. (2010) Observations of turbulence-induced new particle formation in the residual layer. Atmos Chem Phys 10(9):4319–4330, DOI 10.5194/acp-10-4319-2010

Wharton S, Lundquist JK (2012) Atmospheric stability affects wind turbine power collection. Environmental Research Letters 7(1):014,005

Wieringa J (1976) An objective exposure correction method for average wind speeds measured at a sheltered location. Quarterly Journal of the Royal Meteorological Society 102(431):241–253

Wildmann N, Hofsäß M, Weimer F, Joos A, Bange J (2014) MASC–a small remotely piloted aircraft (RPA) for wind energy research. Advances in Science and Research 11:55–61

Witha B, Steinfeld G, Heinemann D (2014) High-resolution offshore wake simulations with the LES model PALM. In: Wind energy - Impact of turbulence, Spring 2012, Oldenburg, Germany, pp 175–181.

Wu YT, Porté-Agel F (2011) Large-Eddy Simulation of Wind-Turbine Wakes: Evaluation of Turbine Parametrisations. Boundary-Layer Meteorol 138:345–366

Wu YT, Porté-Agel F (2012) Atmospheric turbulence effects on wind-turbine wakes: An LES study. Energies 5:5340–5362

Zhang W, Markfort CD, Porté-Agel F (2012) Near-wake flow structure downwind of a wind turbine in a turbulent boundary layer. Exp Fluids 52:1219–1235

Zhang W, Markfort CD, Porté-Agel F (2013) Wind-turbine wakes in a convective boundary layer: A wind-tunnel study. Boundary-Layer Meteorol 146:161–179

Acknowledgement

First and foremost, I would like to thank Dr. Andreas Dörnbrack for his encouraging support. I am very grateful for all helpful discussions and ideas and his invaluable guidance during the three years.

Many thanks to Dr. Thomas Gerz for making this work possible and also for his ideas and comments on my topic.

I would like to thank Prof. Dr. George Craig for supervising the thesis and for his valuable suggestions during the thesis and also on the manuscript.

I would also like to thank Prof. Dr. Markus Rapp for supervising the thesis as a coexaminar and his helpful suggestions during the thesis.

I would like to thank Dr. Piotr Smolarkiewicz for discussions about the subsidence process in EULAG, Dr. Christian Kühnlein for discussions about the adaptive time step in EULAG, Dr. Zbigniew Piotrowski and Dr. Andrezej Wyszogrodski for their help with debugging the 3 D parallelized version of EULAG, and Dr. Wojciech Grabowski for the Baby-EULAG code.

I would like to thank Dr. Fernando Porté-Agel for two very interesting and helpful discussions during the EGU conference in 2015 and the TORQUE conference in 2016. Further, I would also like to thank Dr. Marie Lothon, Dr. David Pino, and Dr. Christopher Moseley for interesting discussions about atmospheric boundary-layer simulations and especially the BLLAST team for sharing the data of the BLLAST field campaign.

Last but not least, I would like to thank the LIPS project working group, Dr. Thomas Gerz, Dr. Andreas Dörnbrack, Dr. Dietrich Heimann, Dr. Arthur Schady, Dr. Josef Schröttle, Dr. Johannes Wagner, Dr. Norman Wildmann, and Bettina Richter for a pleasant and fruitful collaboration.